NASA CR - 180862

NASA

ADVANCED ELECTRIC PROPULSION

AND

SPACE PLASMA CONTACTOR RESEARCH

(NASA-CR-180862) ADVANCED ELECTRIC PROPULSION AND SPACE PLASMA CONTACTOR RESEARCH Annual Report (Colorado State Univ.) 163 p CSCL 21C G3/20

N88-14126

Unclas 0116605

Prepared For

LEWIS RESEARCH CENTER

NATIONAL AERONAUTICS AND SPACE ADMINISTRATION

Grant NGR-06-002-112

Annual Report

January 1987

Paul J. Wilbur
Department of Mechanical Engineering
Colorado State University
Fort Collins, CO 80523

1. Report No. NASA CR-180862	2. Government Accession No.	3. Recipient's Catalog No.

4. Title and Subtitle

ADVANCED ELECTRIC PROPULSION AND SPACE CONTACTOR RESEARCH

5. Report Date: Jan. 1987

6. Performing Organization Code

7. Author(s)

Paul J. Wilbur

8. Performing Organization Report No.

10. Work Unit No.

9. Performing Organization Name and Address

Department of Mechanical Engineering
Colorado State University
Fort Collins, CO 80523

11. Contract or Grant No. NGR-06-002-112

13. Type of Report and Period Covered: Annual, Jan. 1, 1986-Jan. 1, 1987

12. Sponsoring Agency Name and Address

National Aeronautics and Space Administration
Washington, D.C. 20546

14. Sponsoring Agency Code

15. Supplementary Notes

Grant Monitor - Vincent K. Rawlin, NASA Lewis Research Center
Cleveland, Ohio 44135

16. Abstract

A theory of the plasma contacting process is described and experimental results obtained using three different hollow cathode-based plasma contactors are presented. The existence of a sheath across which the bulk of the voltage drop associated with the contacting process occurs is demonstrated. Test results are shown to agree with a model of a spherical, space-charge-limited double-sheath. The concept of ignited mode contactor operation is discussed and this mode of operation is shown to enhance contactor efficiency when it is collecting electrons. A detailed investigation of the potentials in the plasma plumes downstream of contactors operating at typical conditions is presented. Results of tests performed on hollow cathodes operating at high interelectrode pressures (up to about 1000 Torr) on ammonia are presented and criteria that are necessary to ensure that the cathode will operate properly in this regime are presented. These results suggest that high pressure hollow cathode operation is difficult to achieve and that special care must be taken to assure that the electron emission region remains diffuse and attached to the low work function insert. Experiments conducted to verify results obtained previously using a ring cusp ion source equipped with a movable anode are described and test results are reported. A theoretical study of hollow cathode operation at high electron emission currents is presented. This study suggests that it is desirable to increase the hollow cathode body diameter as emission capability is increased and the reasons why this is desirable are discussed. Preliminary experiments conducted using the constrained sheath optics concept to achieve ion extraction under conditions of high beam current density, low net accelerating voltage and well columniated beamlet formation are discussed.

17. Key Words (Suggested by Author(s))	18. Distribution Statement
Electrostatic Thruster Arcjet Thruster Hollow Cathode Electrodynamic Tether Plasma Contactor	Unclassified-Unlimited

19. Security Classif. (of this report)	20. Security Classif. (of this page)	21. No. of Pages	22. Price*
Unclassified	Unclassified	173	

* For sale by the National Technical Information Service, Springfield, Virginia 22161

TABLE OF CONTENTS

LIST OF TABLES

LIST OF FIGURES

ELECTRODYNAMIC TETHER PLASMA CONTACTOR RESEARCH

John D. Williams

Introduction

It is important in some space applications to be able to establish an electrical connection to the local space plasma. A device designed to perform this function is known as a space plasma contactor and ideally it would clamp a point on a spacecraft to a potential near space plasma potential regardless of the current passing between this point and the ambient space plasma. Functioning like a grounding wire on earth, a plasma contactor would provide a reference potential for instruments on board a spacecraft and prevent the spacecraft from charging relative to the potential of the local plasma. The performance of a plasma contactor would become more critical as the current it could be called upon to handle increased to values in the decampere range that are expected in future electrodynamic tether applications.[1] The objective of the work described here is to develop an understanding of the plasma contacting process which can eventually lead to the design of a device suitable for such electrodynamic tether systems.

Theory

Plasma contactor performance can be characterized by plotting the contactor electron emission current vs. the contactor potential measured relative to the local space plasma potential. The ideal plasma contactor would exhibit a current/voltage characteristic curve appearing as a vertical line at zero potential if it could make ions and/or electrons available at a sufficiently high rate so negligible voltage drops would develop over the full range of

current demanded. Such performance might be approached if contactor ion/electron production rates were sufficiently high so that each contactor produced a high density, high conductivity plasma plume with a surface area equal to or greater than the associated tether current divided by the ambient space current density. Although it might be desirable to achieve this level of performance, the large contactor operating powers that could be required to produce the ion and electron current densities needed at high tether current levels could depress overall system efficiencies to the point where this performance level would be unattractive. Consequently, operation of the contactors at conditions where the performance curve would depart from the vertical might be preferred. As Parks, et al.,[2] have pointed out, reduction of the contactor plasma plume size below that which would produce the near vertical (approximately zero impedance) current/voltage characteristic results in the development of a double sheath between the region of the contacting plasma and unperturbed space plasma in the manner suggested by the conceptual sketch in Fig. 1. In this intermediate region two currents, one due to particles from the contacting plasma and the other due to oppositely charged particles from the space plasma, are counterflowing and it is because of this that the term double sheath is used. The total current produced by these counterflowing charged particles under a prescribed potential difference will be limited by space-charge effects and it is suggested that a plasma contactor may always operate at a space-charge-limited condition determined by the sizes of the boundaries between 1) the high density plume and the sheath and 2) the undisturbed space plasma and the sheath. The space-charge-limited current that would flow under ideal conditions can be found by applying a theoretical model developed during this grant period[3] and included as Appendix A to this report. In this model it is assumed that spherical symmetry exists and that the high density plume can be

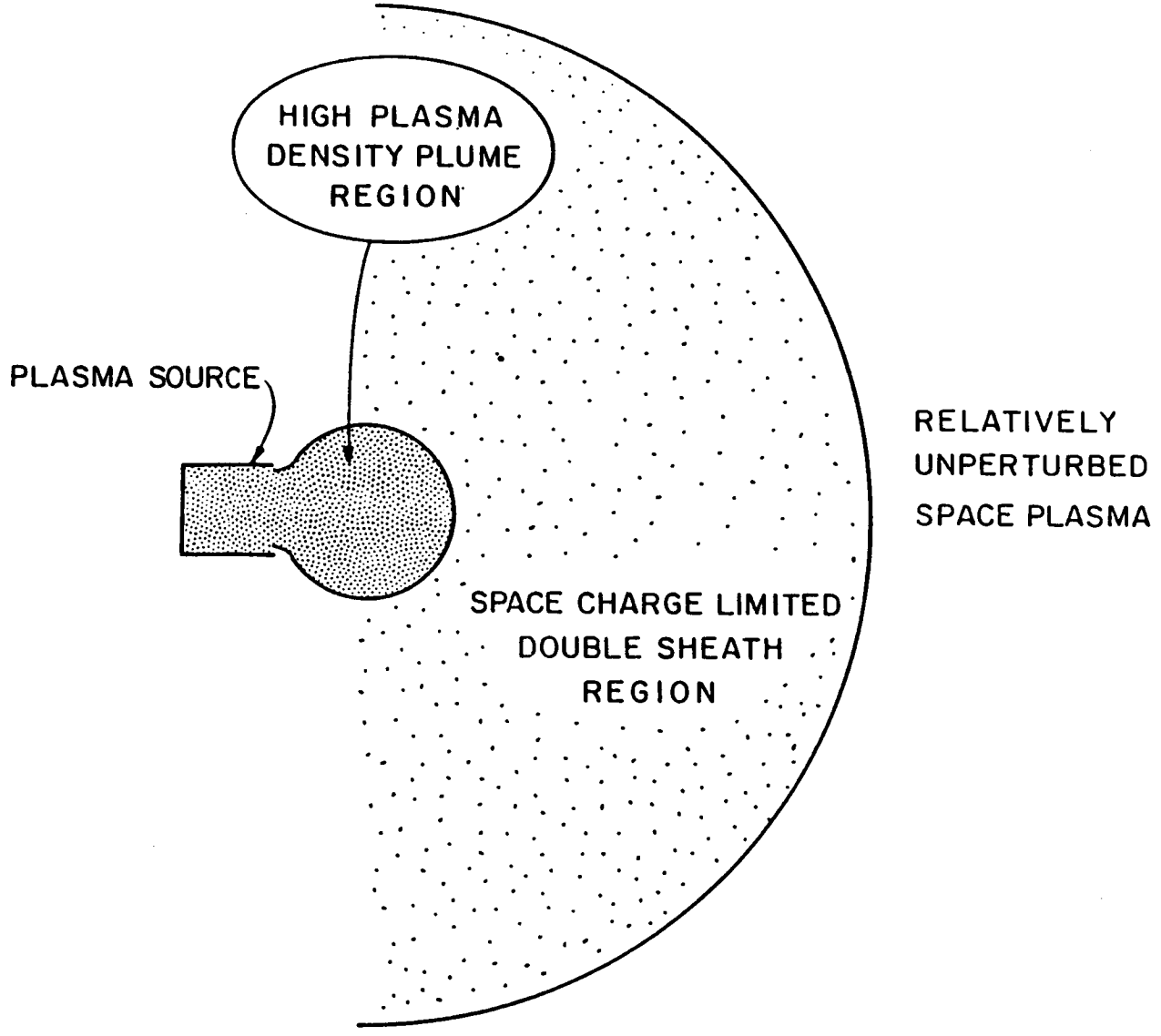

Fig. 1 Plasma Contacting Model

represented by a surface of radius r_i which is an infinite source of zero velocity, charged particles of mass m_i as shown in Fig. 2. Under the influence of a potential V_i a particle current J_i is drawn radially outward toward a second surface representing the low density, ambient space plasma. This outer surface; which serves as an infinite source of zero velocity, oppositely charged particles of mass m_o at zero potential; has a radius r_o and contributes a particle current J_o flowing inward. The model assumes that the effects of ion and electron collisions with either neutral atoms or other ions and electrons can be neglected in the vacuous region between the two surfaces both in terms of the impedance they induce and the production of additional ion-electron pairs. The solution sought to this physical problem is the one corresponding to maximum current flow for both species. This occurs when the electric fields at both r_o and r_i are zero i.e. the doubly space-charge-limited condition. The main result of the paper can be given in the form of equations describing the currents J_o and J_i which are reproduced here as Eqs. 1 and 2.

$$J_o = 4\pi\varepsilon_o V_i^{3/2} (2e/m_o)^{1/2} j_o \tag{1}$$

$$J_i = J_o (\alpha)^{-1} (m_o/m_i)^{1/2} \tag{2}$$

These equations describe the counterflowing currents in terms of the mass m_o of the particles flowing from the outer surface and the mass m_i of the particles flowing from the inner surface, the potential difference V_i between the two surfaces, the constants e and ε_o and the parameters $j_o(r_i/r_o)$ and $\alpha(r_i/r_o)$. These parameters, which have been determined numerically, are plotted as a function of radius ratio in Appendix A. Note that the equations show the currents J_o and J_i are implicit functions of the radius ratio (through j_o and α) and the imposed potential difference but are independent of the actual magnitudes

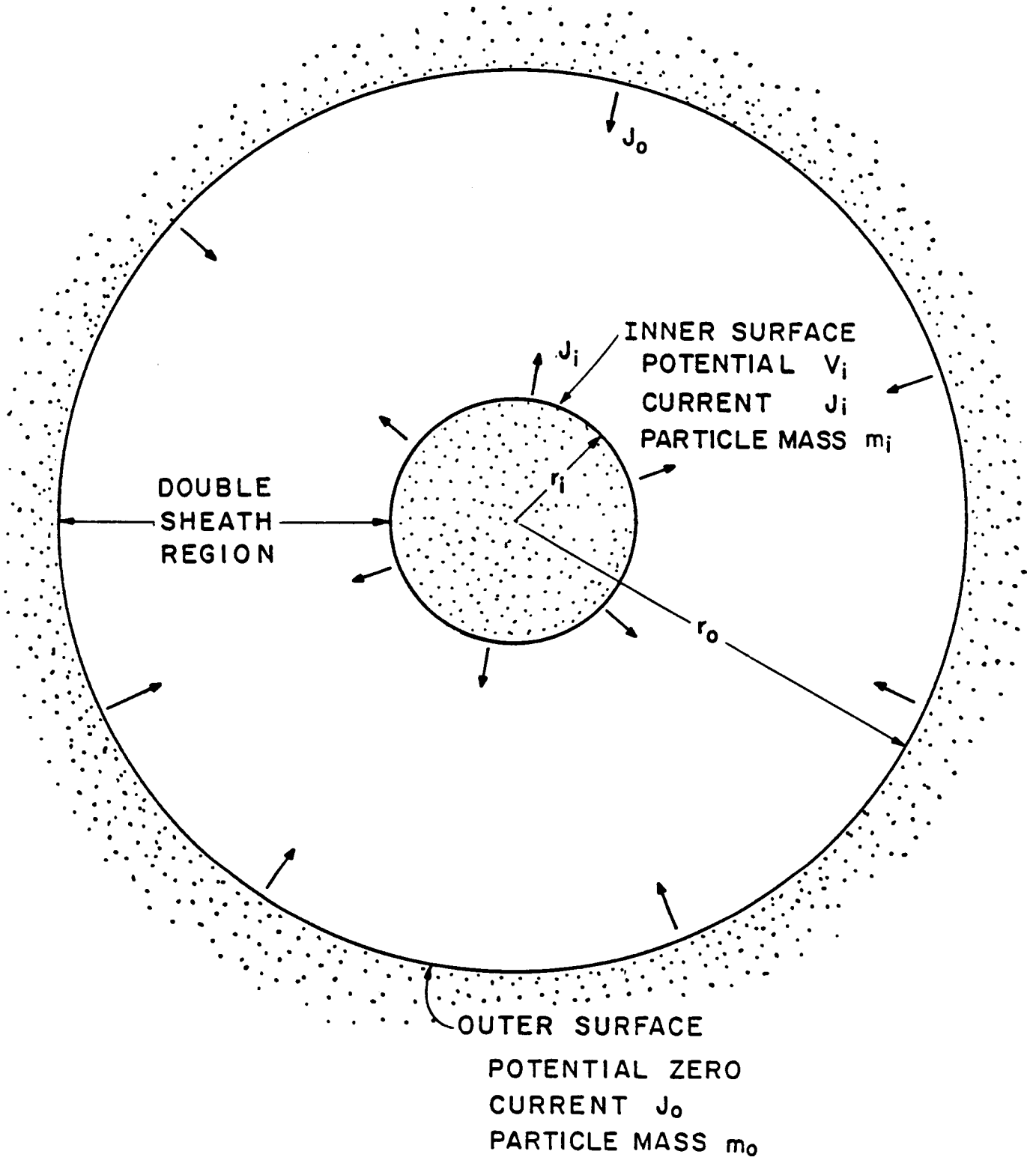

Fig. 2 Theoretical Model Concept

of the radii. In this report potential profiles for theoretical solutions to the space-charge-limited problem will be compared to experimental results in order to determine the conditions under which the model is valid. It is believed that the model will provide a basic picture of the plasma contacting process and be useful in computing currents at prescribed potential differences, when low collision frequency conditions prevail in the double sheath region.

In order to differentiate between the two modes of operation of the plasma contactors (i.e. whether V_i is positive or negative), the term electron collection mode will be used when the contactor is collecting electrons and emitting ions (V_i positive) and the term electron emission mode will be used when the contactor is emitting electrons and collecting ions (V_i negative). Hence for a system operating in the electron collection mode J_o would represent an electron current, J_i an ion current and the two currents would add to give the total conventional current flowing between the two surfaces. Note from Eq. 2 that J_i is considerably less than J_o in the electron collection case because the ion mass is considerably greater than the electron mass. Although this may suggest the ion current can be neglected, the analysis of Appendix A shows that the real importance of the ions is reflected in their ability to neutralize the electron space charge and, hence, increase the electron current over what would flow with no ions present. Since the model predicts improved performance as the radius of the plasma plume approaches the radius of the unperturbed space plasma boundary (i.e. $r_i/r_o \rightarrow 1$) and since the location of the outer boundary is probably fixed for a prescribed total current and ambient plasma condition, the ultimate low impedance plasma contactor should be realized when the high density plume (Fig. 1) is expanded to meet the outer boundary. It appears that this could be accomplished by increasing the ion production rate of the plasma contactor.

Experimental Apparatus and Procedure

In order to measure the performance of a typical plasma contactor as a function of its controllable operating parameters the apparatus suggested by the electrical schematic diagrams of Fig. 3 was set up. As the figure suggests the two major elements of the system are the contactor under test and the simulator used to generate a diffuse, simulated space plasma that can couple to the contactor. Both the contactor and simulator utilize heater power supplies to facilitate cathode startup and maintenance of cathode temperatures and anode power supplies that maintain electrical discharges between their anodes and cathodes. The coupling power supply is used to bias the contactor relative to the simulator so a current can be forced through the plasma between these two devices.

The contactor and simulator are located within a 1.2 m dia by 5.3 m long vacuum tank and are separated by 2.7 m as Fig. 3a shows. The simulator axis is oriented perpendicular to the common axis of the tank and the contactor. The simulator is a 0.64 cm dia hollow cathode plasma source that has a 0.76 mm dia cathode orifice and utilizes an R-500* treated, rolled tantalum foil insert. It is equipped with a 2 cm dia flat plate anode 1 mm from the cathode with no orifice in it. This anode design was used because it was believed that it would provide a diffuse, non-focused plasma which would approach a realistic simulation of the ionospheric plasma. Although the same hollow cathode device was used to produce the simulated space plasma throughout all experiments, the conventional hollow cathode plasma contactor (distinguishd by the dotted boundary in Fig. 3b) was replaced with two other contactor configurations. These contactors, the ring cusp contactor and the variable area anode contactor, are shown schematically in Fig. 4 and are also enclosed by dotted boundaries to indicate visually that they can be interchanged with the

*Chemical R-500 is a double carbonate ($BaCO_3$, $SrCO_3$) mixture that has been manufactured by the J.R. Baker Chemical Co., Phillipsburg, N.J. but is no longer made.

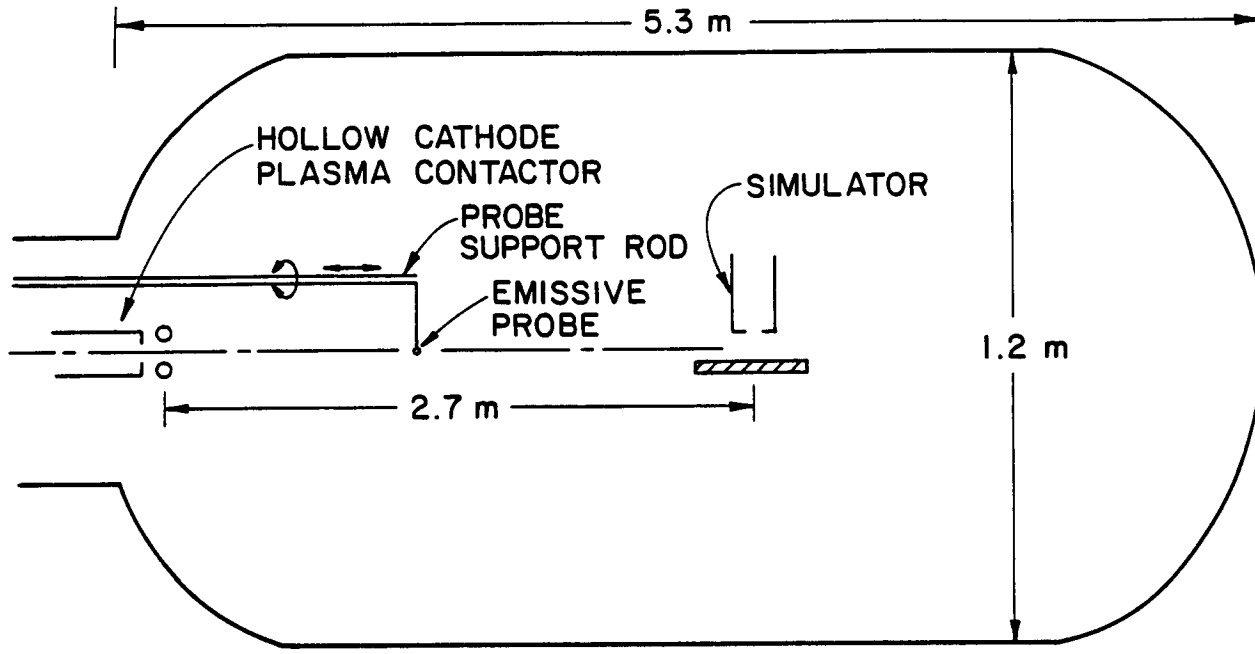

a. MECHANICAL

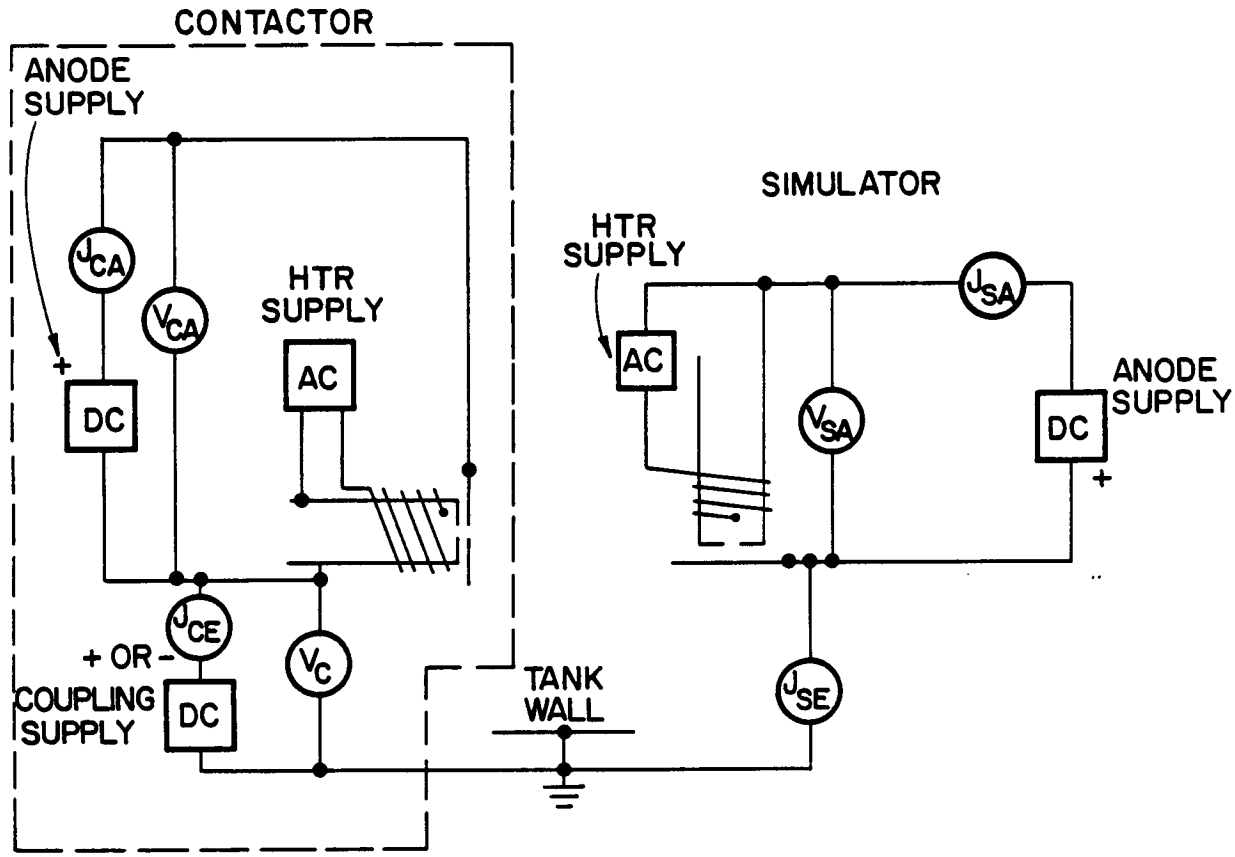

b. ELECTRICAL

Fig. 3 Schematic Diagrams

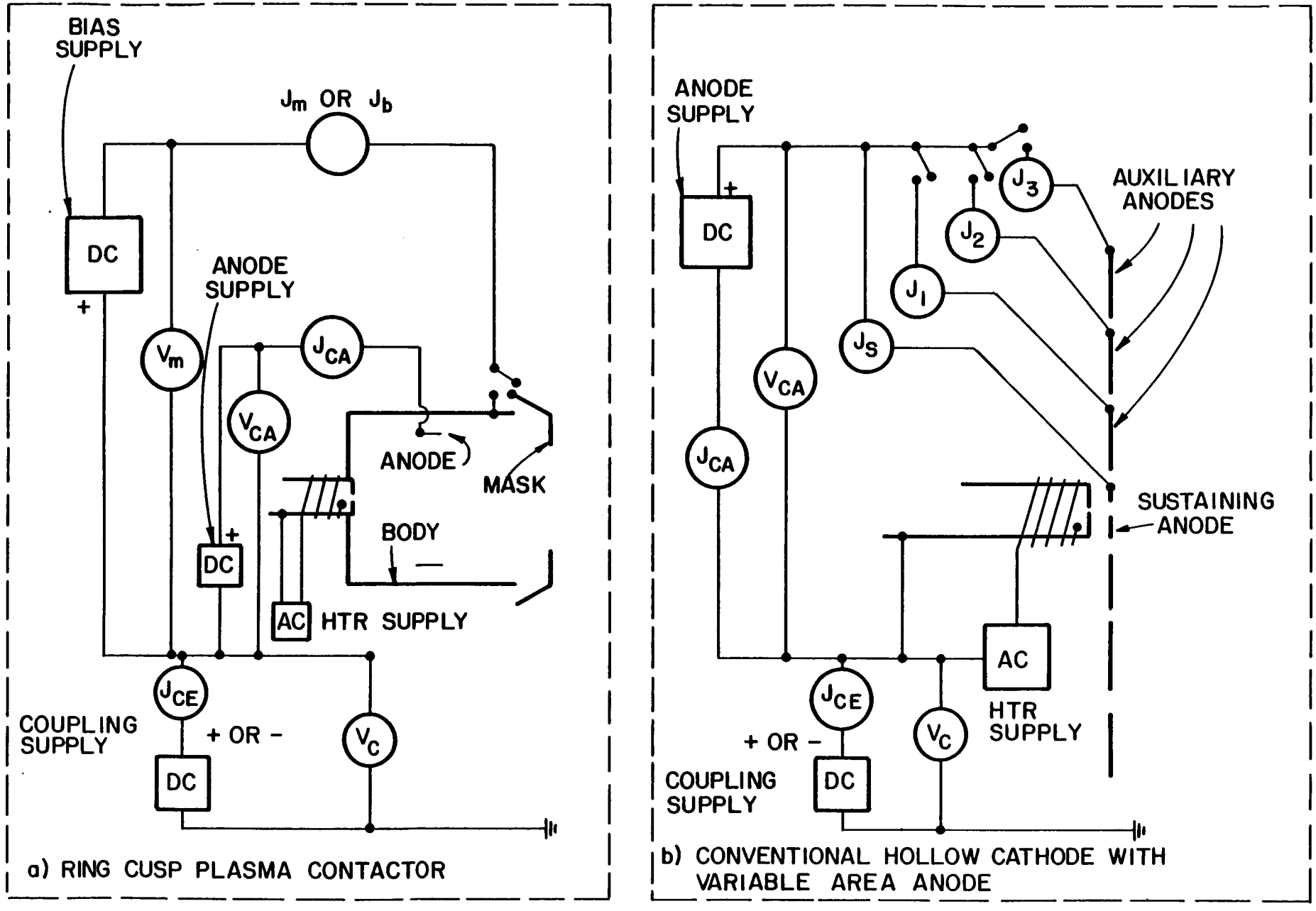

Fig. 4 Alternative Plasma Contactor Schematics

one shown in Fig. 3b. Also shown in Figs. 3b and 4 are the locations of the meters used to measure the currents and potentials considered important to the tests. The symbols used to designate the measured currents or potentials are indicated within the circles representing the meters. The power supplies needed to sustain operation of the contactors and the coupling and bias supplies are labeled and shown as squares on the figures.

Also shown in Fig. 3a is the rod used to support and position the emissive and Langmuir probes which were used to measure plasma properties in the region extending to the plane 1 m downstream of the contactor. The measuring circuits and mechanical designs for these probes are similar to those which have been used previously and they are described by Aston[4] and Laupa,[5] respectively. In the present research the emissive probe system differs from the previous design in that the probe output is transmitted to an X-Y plotter along with the output of a probe position indicating potentiometer so continuous traces of the plasma potential vs. axial position between the contactor and simulator are recorded. The emissive probe can be swept along the tank centerline or rotated so plasma potential profiles along paths parallel to the centerline are obtained. By using the data from such traces recorded at various radii, sufficient data can be collected so equipotential contours can be generated to describe the complete potential picture in the region downstream of the contactor.

Three different configurations of contactors were investigated during the grant period. They included the conventional hollow cathode (Fig. 5) the ring cusp magnetic field (Fig. 6) and the variable anode area (Fig. 7) plasma contactors. The conventional hollow cathode contactor consists of a 7 mm dia tantalum tube with a 0.7 mm orifice in an orifice plate welded to one end of

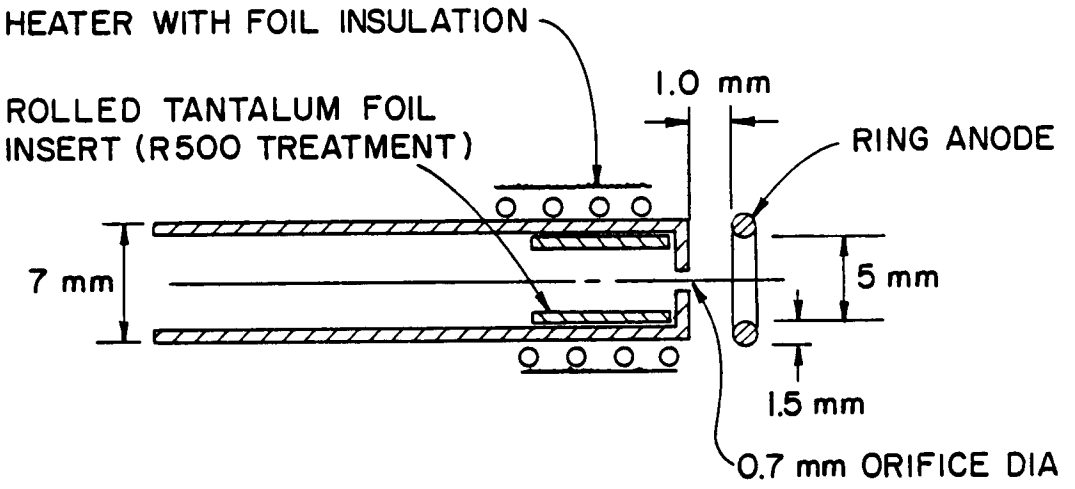

Fig. 5 Conventional Hollow Cathode Contactor

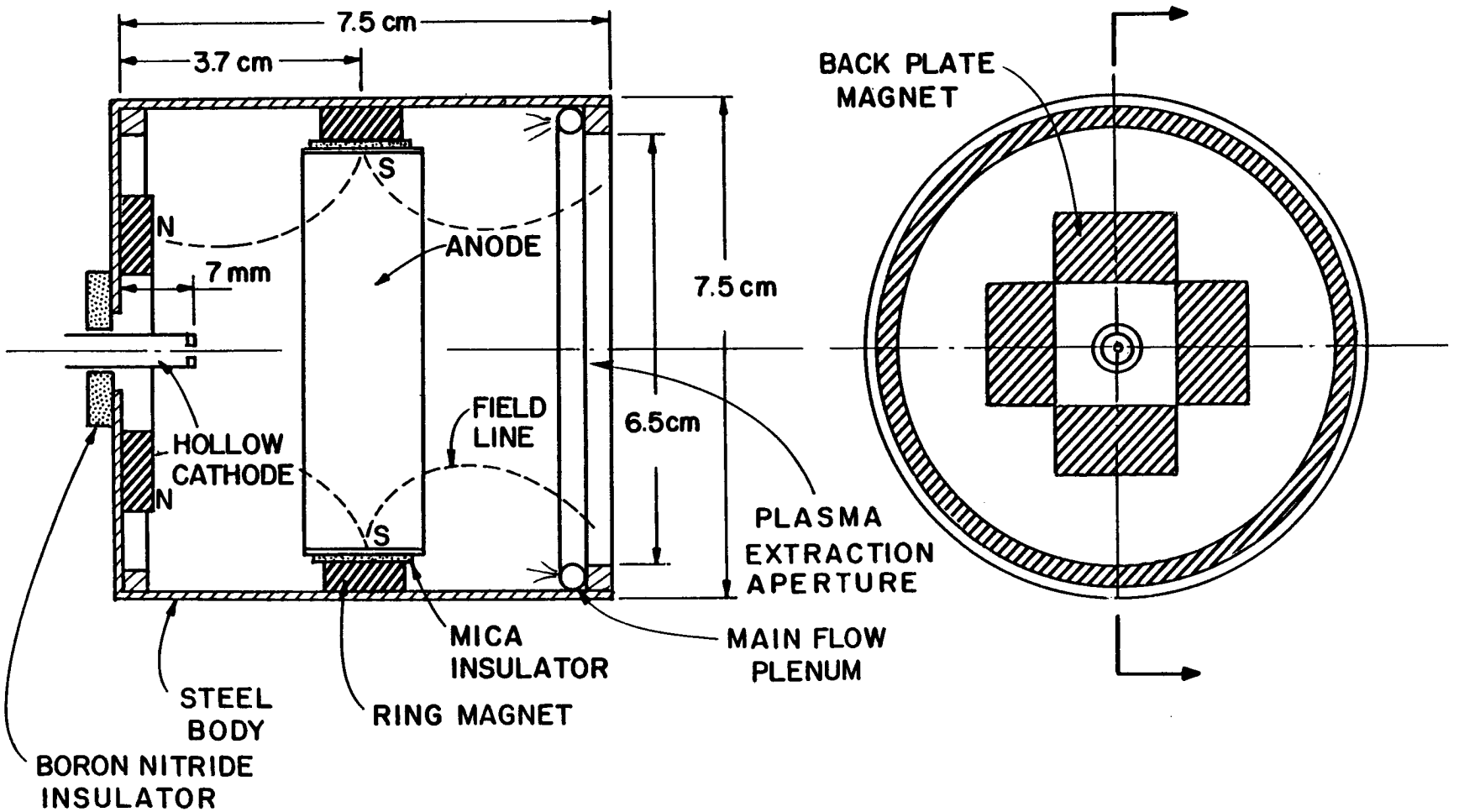

Fig. 6 Ring Cusp Magnetic Field Contactor

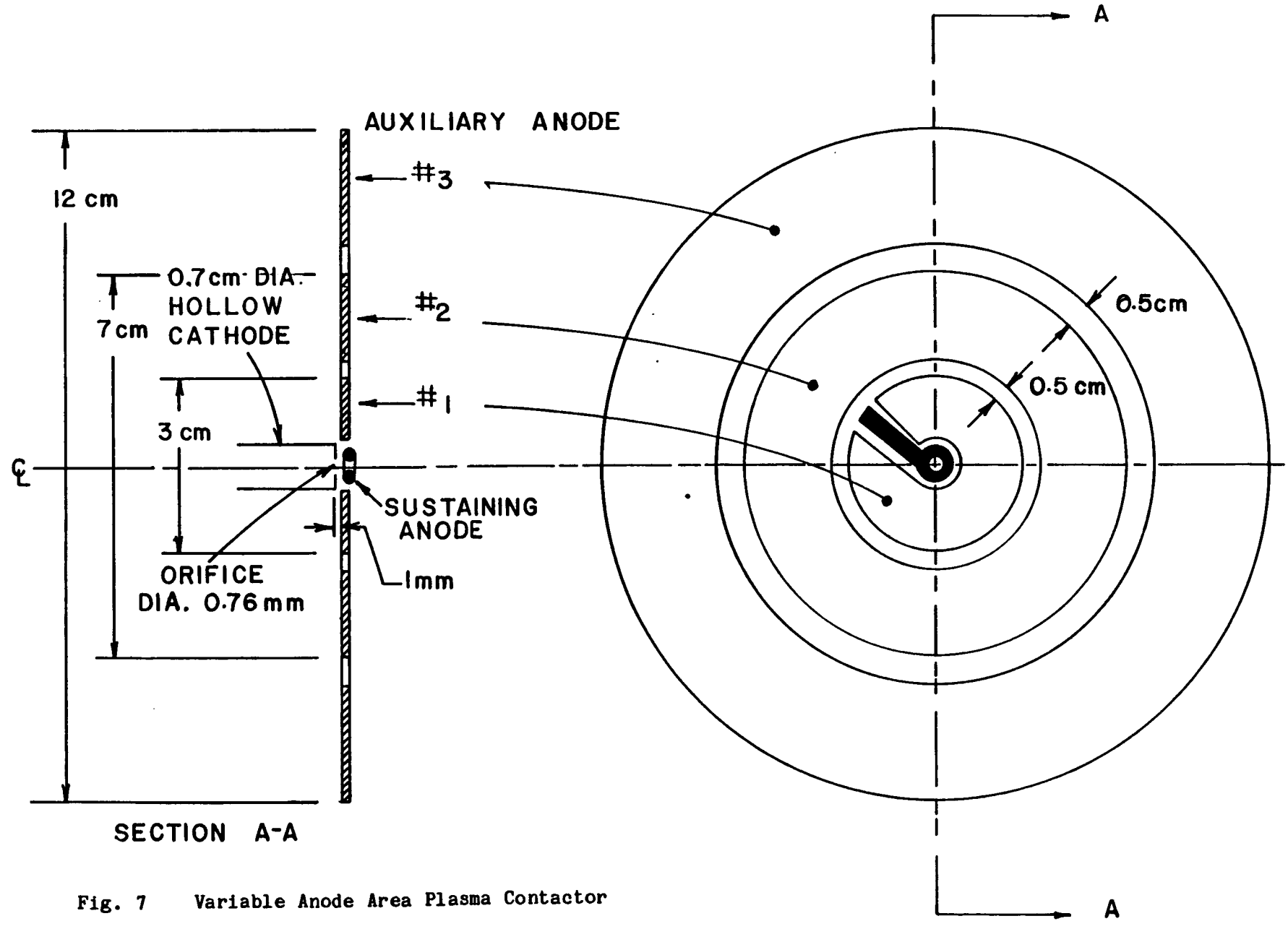

Fig. 7 Variable Anode Area Plasma Contactor

the tube. The insert in the cathode is made of 0.013 mm thick rolled tantalum foil covered with the low work function material Chemical R-500. The insert region of the tantalum tube is heated by a swaged heater wrapped with a tantalum foil radiation shield. The anode is 1 mm downstream of the orifice and is a loop of 1.5 mm dia tantalum wire with an outside dia of 8 mm. Because this device was not designed to produce ions efficiently or to provide a large anode plume boundary, it was not expected to be a superior plasma contactor, but rather a device that could be used to study the plasma contacting process.

A contactor which should be capable of better performance than the conventional contactor because it is designed to produce ions efficiently is the ring cusp magnetic field contactor[6] shown in Fig. 6. The ring cusp contactor utilizes the same hollow cathode electron source as the conventional hollow cathode contactor, and enhanced ion production is facilitated in it because of the cusped magnetic field indicated by the dotted lines in Fig. 6. This field, which is produced by a ring of samarium cobalt magnets near the chamber midsection and the magnet at the upstream face of the chamber, enhances performance by confining most primary electrons (i.e. those supplied by the catnode) from being lost directly to the anode until after they have had ionizing collisions. As a consequence of the electron confinement it is believed that the ions are also confined so they can be extracted preferentially through the open end of the chamber rather than being lost through recombination on the chamber walls. The samarium cobalt magnets have a flux density at their surfaces of 0.27 Tesla and the discharge chamber steel construction provides a low reluctance return path for the magnetic field lines they induce through the chamber. The plasma source is also designed so expellant can be supplied through both the hollow cathode at a flowrate $\dot{m}_c$ and a main flow ple-

num located at the downstream end of the discharge chamber at a rate $\dot{m}_b$.

The variable area anode plasma contactor (Fig. 7) also utilizes the conventional hollow cathode as its electron source but it has a large diameter segmented anode. The sustaining anode shown in Fig. 7 is always held at anode potential, but each of the progressively larger segments shown may either float or be held at anode potential. This design makes it possible to vary the effective anode diameter from ~1 to 12 cm by simply changing switch positions.

Normally the contactors were first tested with the simulator off by varying the coupling supply output voltage (V_c) from ~-70 to 130 V. As the contactor is biased negative relative to the tank, it will emit electrons and when the contactor is biased sufficiently positive the electrons produced in the discharge will be reflected from the tank walls and simulator anode thereby allowing measurement of the small ion current (ion production current) being drawn to these surfaces. Typically this ion production rate associated with a particular contactor operating condition can be measured when the coupling voltage V_c is above ~30 V. Further moderate increases in V_c will not cause this current, measured on the contactor emission current meter J_{CE} shown in Figs 3b and 4, to increase. This occurs because the sheath that develops at the tank wall is able to reflect all electrons including those from the Maxwellian tail so only the ions produced are collected. Hence the ion current collected at the tank wall is limited to the rate at which ions are produced by the contactor at its prevailing flowrate and discharge current operating condition. It has also been observed that increasing the coupling voltage V_C above ~100 V causes the ion current measured to increase above the stable value observed at a coupling voltage near 30 V. It is assumed that

this occurs because high potential differences cause excessive acceleration of the ions through the sheath at the tank wall thereby causing secondary electrons to be ejected from the tank surface. These electrons are then collected at the contactor anode thereby causing the contactor emission current J_{CE} to increase. Arcing from the tank walls to the contactor was also observed at these high potentials and this supports the suggestion that the metallic tank may have been participating in this way. To prevent these effects a coupling voltage near 30 V was used when ion production rates were being measured. After the ion production capability of each contactor had beem measured at a specified operating condition, plasma potential profiles associated with particular contactor operating conditions were recorded using the emissive probe.

The simulator was started next and allowed to stabilize at a flowrate ($\dot{m}_s$) of 1.9 sccm (Xe) and a discharge current J_{SA} of 0.3 A; this normally resulted in an anode voltage V_{SA} of ~14 V. Once the simulator was operating stably the coupling voltage V_C was varied through the range ~-70 to 130 V. At each operating point all of the currents and voltages indicated in Fig. 3b were measured and plasma potential profiles could be recorded using the emissive probe. Typically these data were used to generate a curve of contactor electron emission and collection current (J_{CE}) as a function of a potential difference considered representative of the potential difference between the contactor and simulator plasmas. Such a curve is referred to here as the characteristic curve of the contactor. The potential difference used to generate the curve was initially the one between the contactor anode and the simulator anode ($V_C + V_{CA}$). This potential difference was chosen because the potentials of the plasmas at the simulator and contactor were expected to close to their respective anode potentials so it was believed this potential difference would be representative of the potential drop through the

intervening plasma. It should be noted, however, that the contactor potential ($V_C + V_{CA}$) defined in this way is actually the potential drop across both the contactor and simulator and it was therefore not the preferred measure of contactor performance as tests conducted near the end of the grant period eventually demonstrated. All tests were performed using xenon as the expellant over a wide range of contactor anode currents and voltages. The tank pressures (P_t) measured during tests ranged from $1x10^{-6}$ Torr at low contactor flowrates to $1.2x10^{-5}$ Torr at high ones.

Results

Generic characteristic curves obtained showing the operating features observed in essentially all hollow cathode-based plasma contactors with the simulator on and off are shown in Fig. 8. It shows that a contactor operating in the electron emission mode (2nd quadrant) exhibits a curve that is close to the ideal (vertical) one. In this region essentially all hollow cathode contactors are observed to emit up to several amperes of current at contactor potentials of ~ -50 V independent of whether the simulator is on or off. This independence of the electron emission portion of the characteristic curve from the simulator operating condition is a consequence of the fact that electrons emitted by a contactor are generally collected on the vacuum tank wall whether the simulator is operating or not. The tests described herein were conducted under conditions where the simulator was operating at a low power level to produce plasma densities of the order of $10^6/cm^{-3}$ near the midpoint of the region between the contactor and simulator. Operation of the simulator to produce a higher plasma density might be expected to induce a still steeper curve but it would be less representative of the performance expected in space.

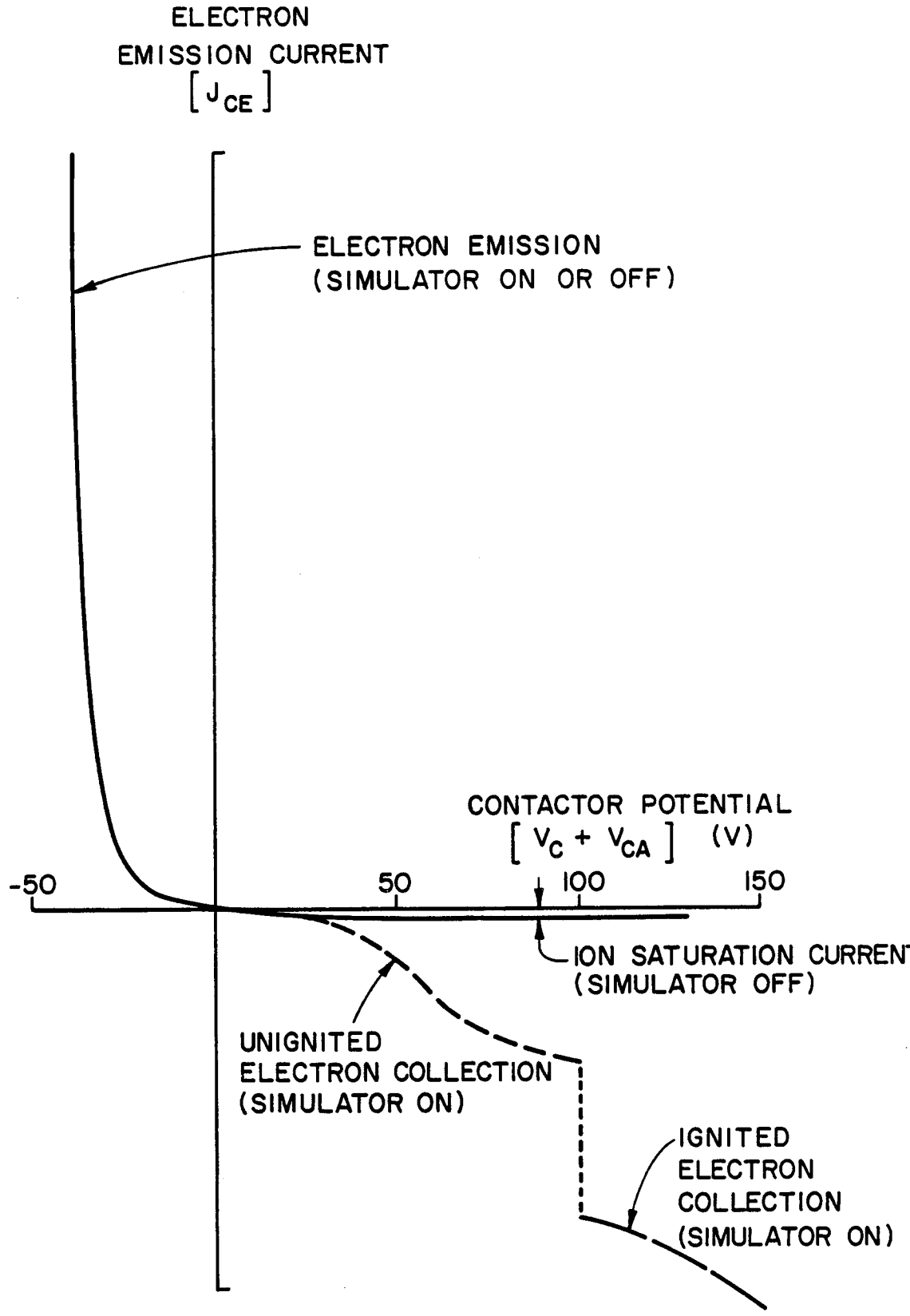

Fig. 8 Generic Contactor Characteristics

In general, the contactor performance curve in the electron collection/ion emission mode (4th quadrant of Fig. 8) when the simulator is on shows much more structure than the electron emission curves or the ion emission only curve (4th quadrant, simulator off). In this mode the electron collection current increases in both magnitude and absolute gradient as the contactor potential is increased from low positive values. Near 60 V Fig. 8 shows an inflection point in the electron collection curve beyond which the gradient of electron collection current with contactor potential decreases and the curve levels out due to a limiting phenomenon which has not been identified. At contactor potentials ($V_C + V_{CA}$) of the order of 100 V the contactor has been observed to undergo a transition from what might be termed the unignited mode to the ignited mode of electron collection. This transition, which is accompanied by the appearance of a visible plume within which expellant excitation and presumably ionization are occurring, is most likely to occur in contactors utilizing large diameter anodes. The visible plasma plume associated with ignited mode operation usually extends downstream of the anode ~5 to 20 cm. Again the point at which transition to ignited electron collection occurs depends on hollow cathode operating conditions and ambient pressure. For example this transition may occur before or after the unignited electron collection curve begins to level out depending on these conditions.

The ion saturation current, measured with the simulator off, is represented as the vertical separation between the solid curve and the horizonal axis in the 4th quadrant of Fig. 8. This curve remains relatively flat for contactor potentials greater than ~30 V at an ion production current which depends upon the particular contactor being tested, the expellant flowrate, and discharge power.

When a contactor is operated in the electron collection mode with the simulator on, the plasma potential profile along the centerline joining the contactor and simulator has the general shape shown by the solid line in Fig. 9a. This figure shows that the plasma potential at the contactor, measured relative to tank/simulator anode potential, is near contactor anode potential and that it remains at this potential as one moves downstream to the point r_u. Between the points r_u and r_d the potential drops by V_S because of a double sheath that develops at the prevailing current condition. Beyond the location r_d the potential changes very slowly until it drops rapidly to simulator anode potential through an electron extraction/ion collection sheath that develops adjacent to the simulator. The region between the double sheath and the simulator in Fig. 9a might show a small gradual potential drop that could develop because of collisional effects or magnetially induced impedance, but slight potential increases and negligible potential gradients have also been observed in this region.

For the case of ion emission only (simulator off) the dotted plasma potential profile in Fig. 9a indicates that a small potential sheath develops between the contactor anode and the plasma near the contactor. The potential directly downstream of the contactor remains constant near anode potential until a sheath, which was not measured directly but which probably develops near the tank wall and cold anode of the simulator collects the ions and completes the circuit. It is noted that the potential profiles shown in Fig. 9 cannot be measured continuously using the emissive probe because it can only be swept 1 m downstream of the contactor. The solid line (simulator on) profile shown in Fig. 9a was actually constructed by measuring profiles while operating the contactor in the electron collection mode and then in the electron emission mode and combining the results to show the expected potential

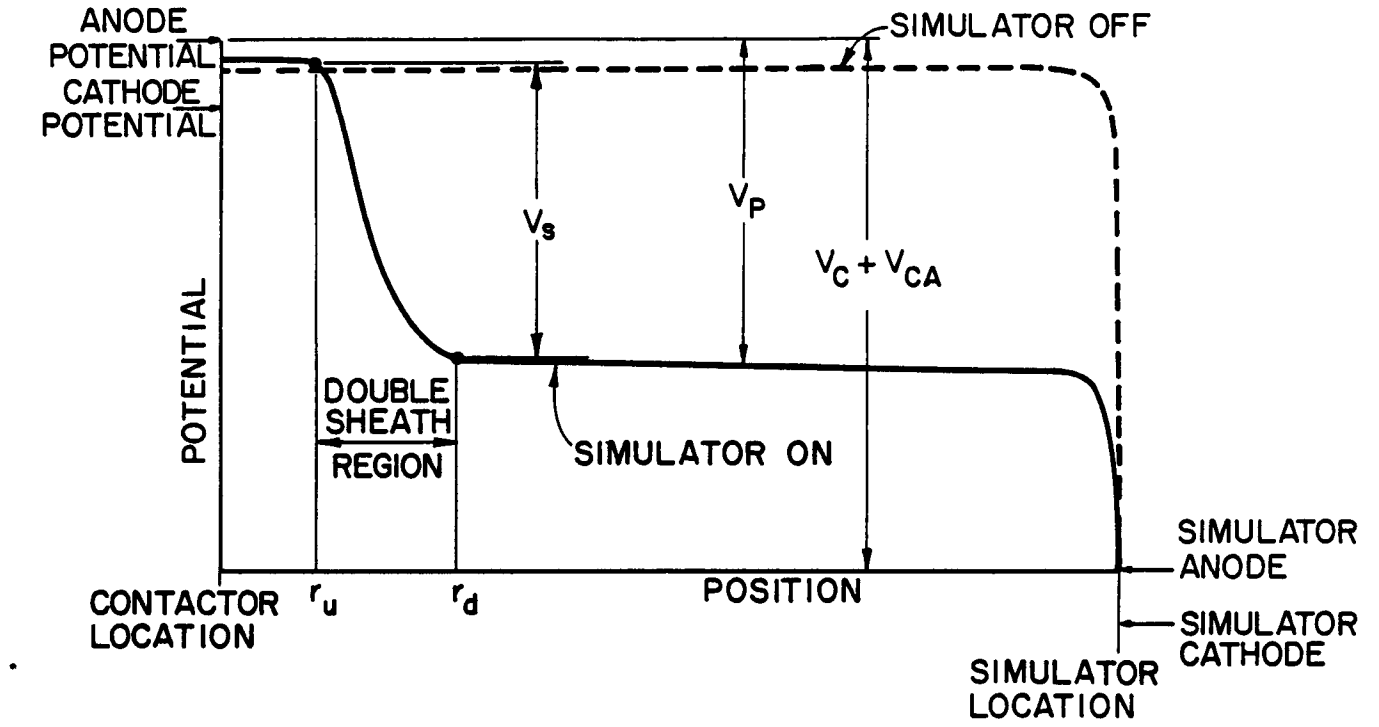

a) ELECTRON COLLECTION / ION EMISSION

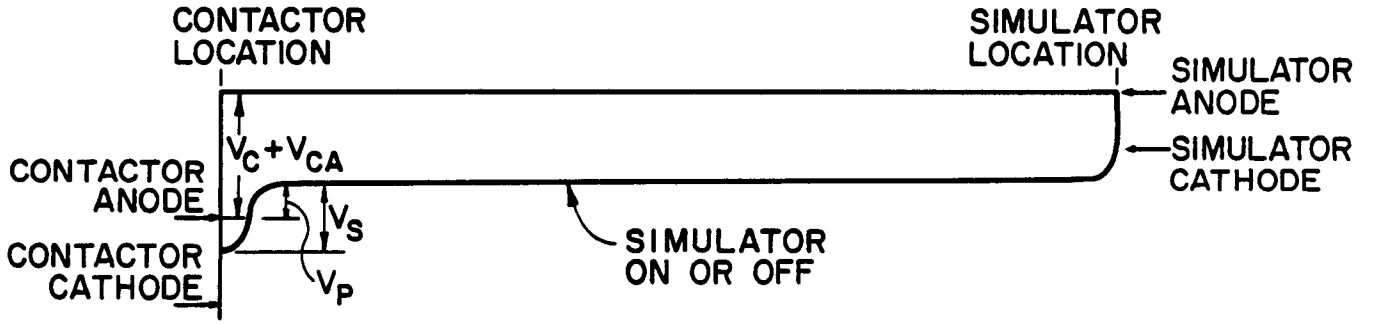

b) ION COLLECTION / ELECTRON EMISSION

Fig. 9 Generic Potential Profiles

variation along the centerline between the contactor and simulator. Figure 9b shows the generalized potential profile for a contactor operating in the electron emission mode when the simulator is either on or off. In these cases the plasma adjacent to the contactor is near anode potential and the potential changes only slightly with position until the bulk of the potential rise occurs near the simulator anode surface.

In order to achieve a good simulation of the plasma contacting phenomena expected in space it is necessary that the simulation environment reproduce the environment expected in space. This condition would be satisfied if the following variables could be controlled at values similar to those expected in space:

- ambient ionic and neutral gas species and their densities,
- ambient electron density and temperature,
- ambient magnetic field strength.

No attempt has been made in these tests to keep the ionic and neutral gas species at the concentrations expected in space. In fact, xenon levels in the tank required for proper contactor operation induce vacuum tank pressures that exceed those expected in the space environment. Also the plasma densities in the dilute, simulated space plasma have not been measured during all of the tests. Actually, with the present experimental set up the Langmuir probe can only be swept through the region extending to 1 m downstream of the contactor so it cannot probe the plasma adjacent to the simulator. The plasma in the region immediately downstream of the conventional contactor has been probed over the range of conditions investigated in this report however, and typical

plasma density profiles measured in these tests are shown in Fig. 10. They suggest electron densities in range near 10^5 - 10^6 cm^{-3} exist in the region intermediate between the contactor and simulator. This range of densities is considered to be reasonably close to the values expected in the space environment where tether tests are planned. Electron temperatures measured in the tests were about 1 eV which is higher than the 0.2 eV temperature associated with space plasma.

The symbols used in Fig. 10 to represent voltages (V) and currents (J) have been defined in Figs. 3 and 4. The other symbols ($\dot{m}$) and (P_t) represent flowrate in standard cubic centimeters per minute (sccm) of xenon (Xe) and vacuum tank background pressure in Torr respectively. The background pressures have been corrected to account for the fact that the cold cathode gauge used to measure them has a different sensitivity for xenon than it does for the nitrogen on which its calibration is based.

In order to investigate the importance of the ambient magnetic field, tests were conducted in which the ambient field was changed to determine its effect on the contactor performance. The test facility in which the tests were conducted is stainless steel so the 0.5 gauss geomagnetic field penetrates the tank. This field is inclined at ~70^o to the axis joining the contactor and simulator throughout the region of plasma interaction . In order to investigate the effect of magnetic field on the test results, a Helmholtz coil was installed so that it could be energized to null the geomagnetic field. With the currents through the Helmholtz coil adjusted to their optimum values the magnetic field was measured along the axis of the tank and determined to be within 0.1 gauss of zero over the plasma interaction region.

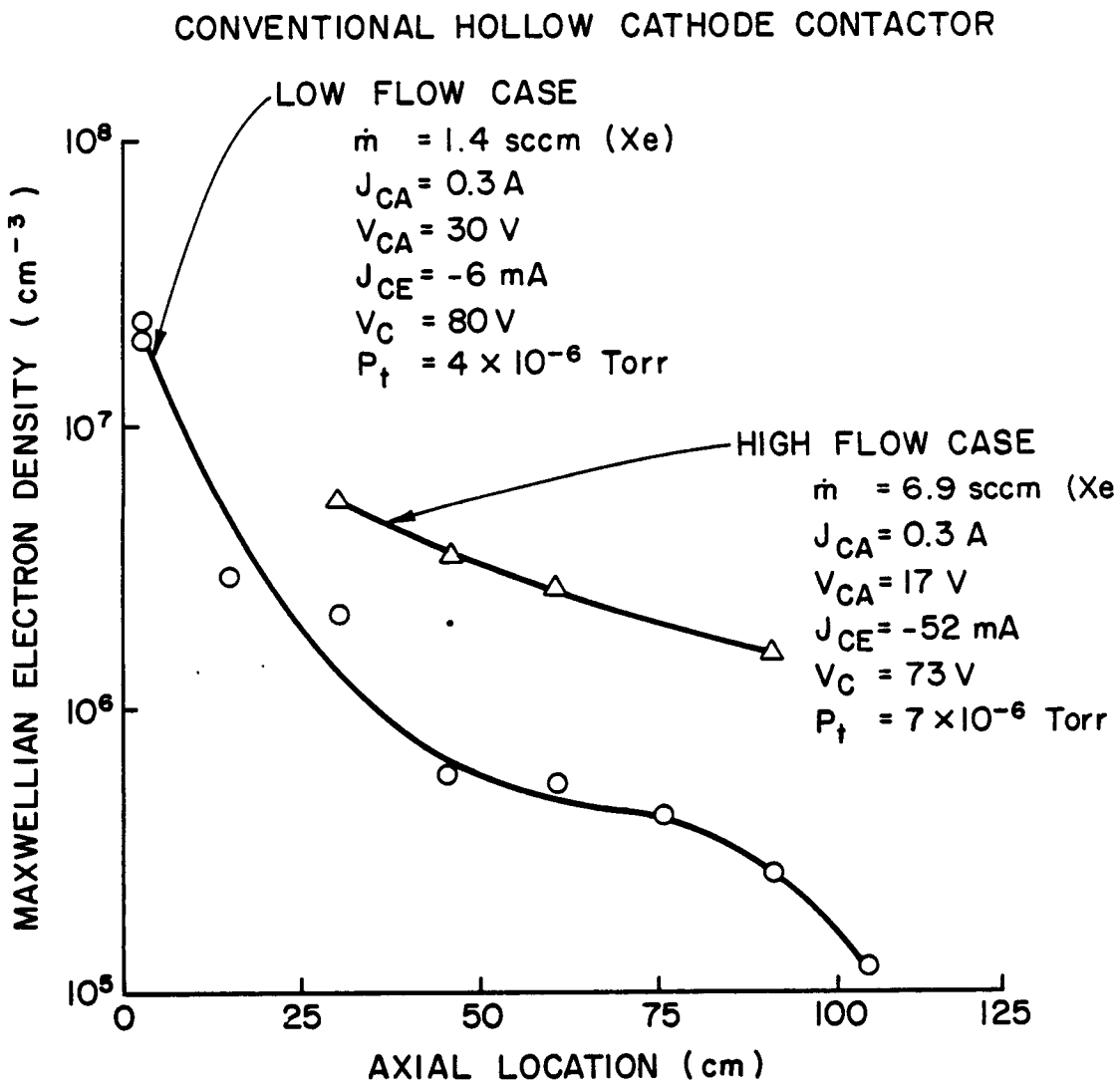

Fig. 10 Plasma Density Profiles

These tests were conducted early in the grant period so the simulator used was actually a hot filament source of electrons[5] rather than a hollow cathode. Still the test results shown in Fig. 11 indicate that the geomagnetic field has no significant effect on the performance of the plasma contactor. Hence for all of the tests described herein the geomagnetic field was not nulled and a 0.5 gauss field existed throughout the interaction region.

The approach used in conducting this test has been to involve the vacuum tank walls in such a way that the most realistic simulation of the space environment would be realized. For a contactor operating in the electron emission mode the tank walls surrounding the contactor and simulator have been used in conjunction with the simulator to collect the electrons emitted by the contactor. This is justified on the basis that the contactor will be completely surrounded in space by a plasma which can collect the emitted electrons. If the simulator anode were forced to collect all of the emitted electrons in these ground tests, they would have to flow to the simulator anode, which is very small. Consequently, it was considered more appropriate to achieve better geometric simulation and use the surrounding tank walls to collect the electrons. For the case of electron collection by the contactor the tank walls cannot realistically serve as a source of electrons so the approach has been to minimize the tank wall participation and to require that all electrons collected by the contactor be supplied from the simulator. Any significant discrepancy between the simulator emission current (J_{SE} in Fig. 3b) and the contactor collection current (J_{CE} in Figs. 3b and 4) suggests the tank is affecting the results and was regarded as justification for rejecting the data.

Conventional Hollow Cathode Contactor

Actual characteristic curves measured using the conventional hollow

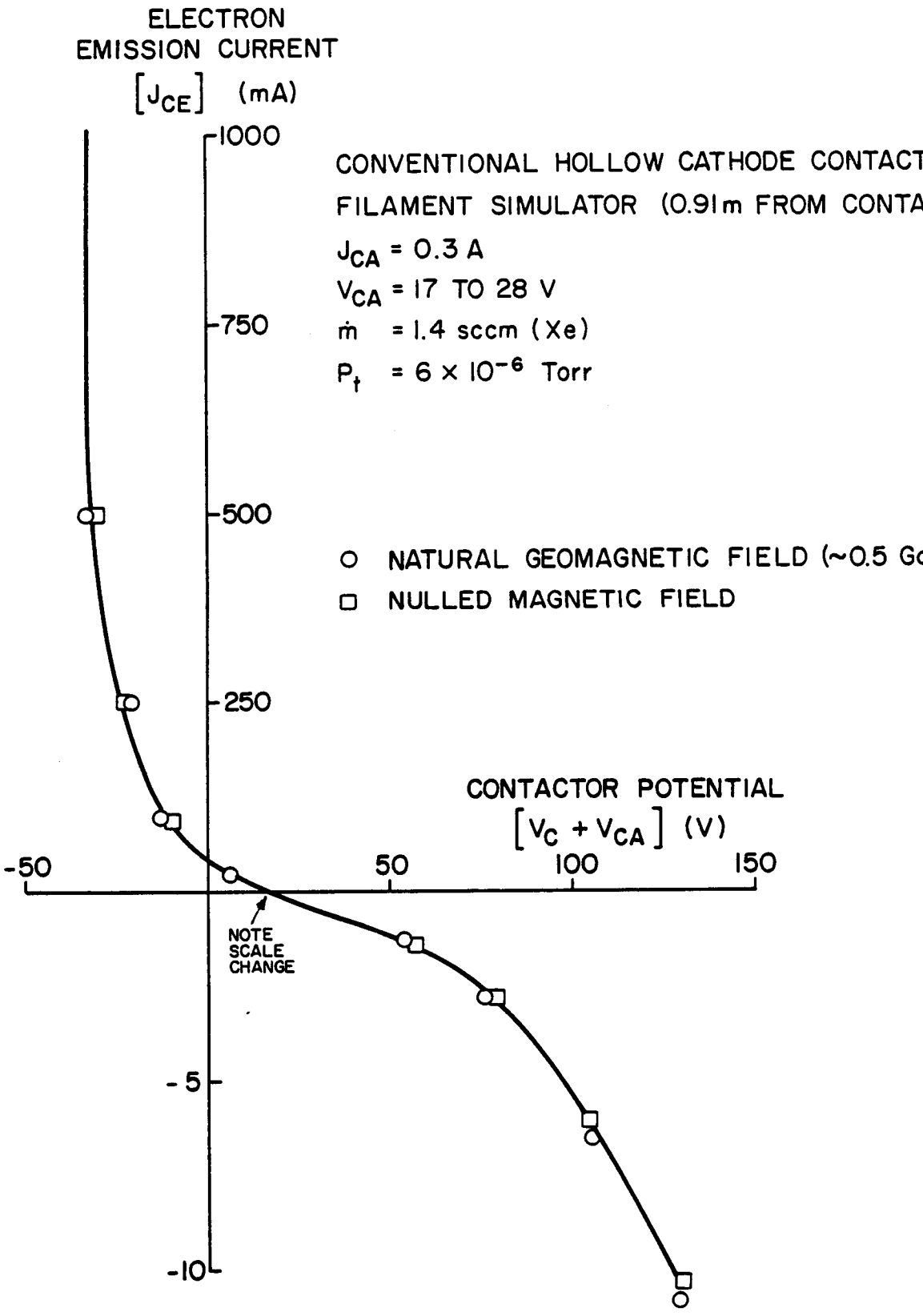

Fig. 11 Effect of Magnetic Field on Contactor Performance

cathode are shown in Fig. 12. Note that although the contactor performs well in the electron emission mode with the simulator on or off, it does not undergo a transition into the ignited mode of electron collection when the simulator is on, conditions are as defined on the figure and contactor potentials are limited to 150 V; consequently, it does not collect large currents from the simulator. These low electron collection currents are plotted on a different scale than the electron emission data as indicated on the figure. The ion emission current data represented by the square symbols (simulator off) in the 4th quadrant show this current remains relatively constant at ~1 mA before it increases slightly at high contactor potentials. This increase in current is presumably due to collection of electrons ejected from the tank wall by high energy ions (~140 eV) rather than any improvement in the ion production capability of the contactor at high coupling potentials.

At each of the solid data points identified by letter in Fig. 12 plasma potential profiles were measured using the emissive probe and these profiles, identified by the same letters, are shown in Figs. 13 and 14. Under electron emission conditions (Curves C, D, and I) the potential profiles are seen to be quite flat except immediately adjacent to the contactor, i.e., within about 5 cm, where a voltage drop indicative of a sheath exits. This must be a double sheath which develops as the contactor emits electrons to and draws ions from the simulated plasma, but the sheath is located close to the contactor in a region that is difficult to probe. If a high plasma density, constant potential region exists adjacent to the contactor is not apparent from these measurements. Curve H in Fig. 14 shows a less severe potential gradient near the contactor than the other electron emission profiles presumably due to its lower emission current, (500 mA as opposed to 650, 1000, and 1000 mA). Under conditions of electron collection (Curves A and B) the profiles are observed to be quite different. In general they show a region of relatively constant

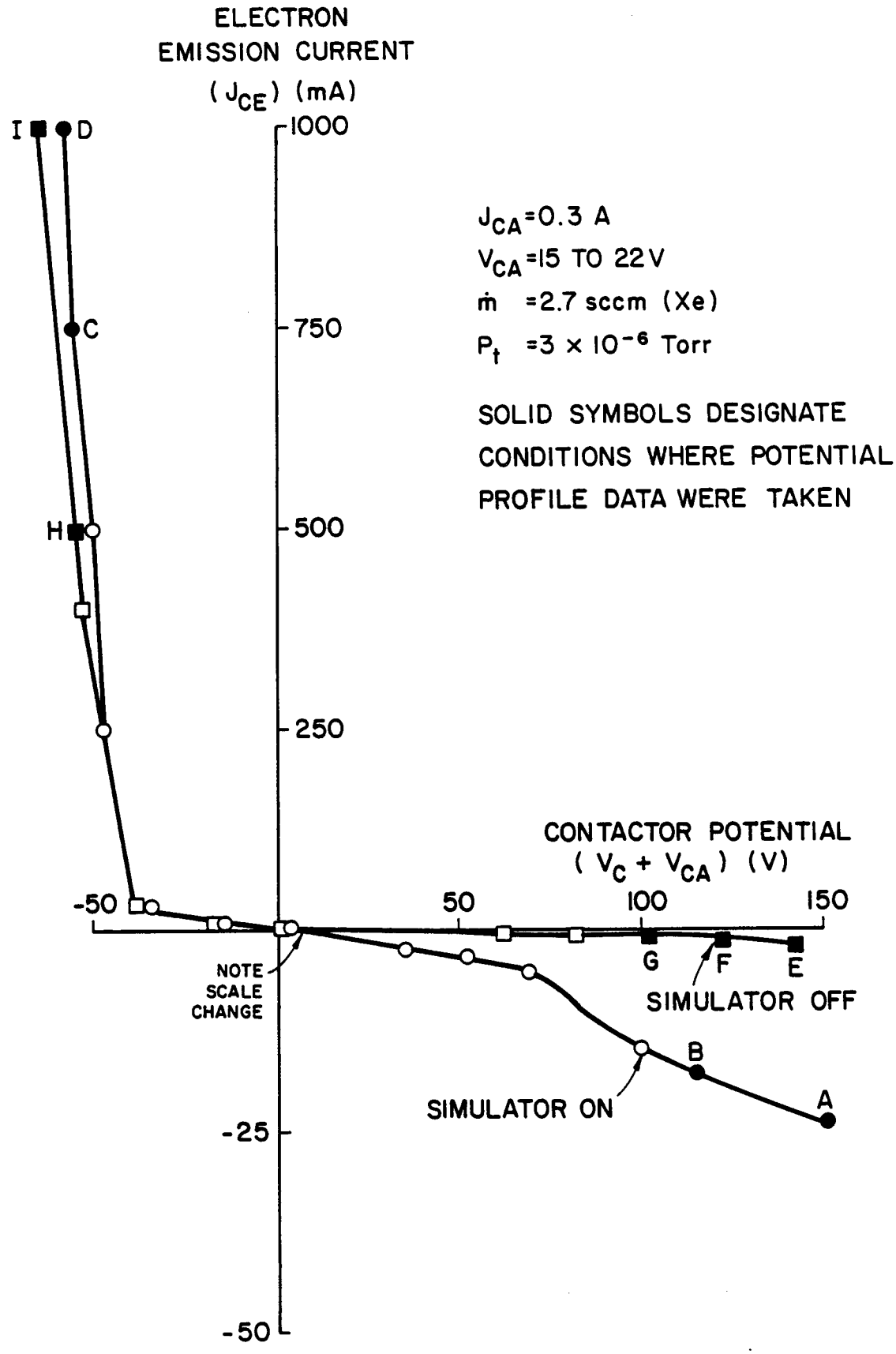

Fig. 12 Conventional Hollow Cathode Characteristics

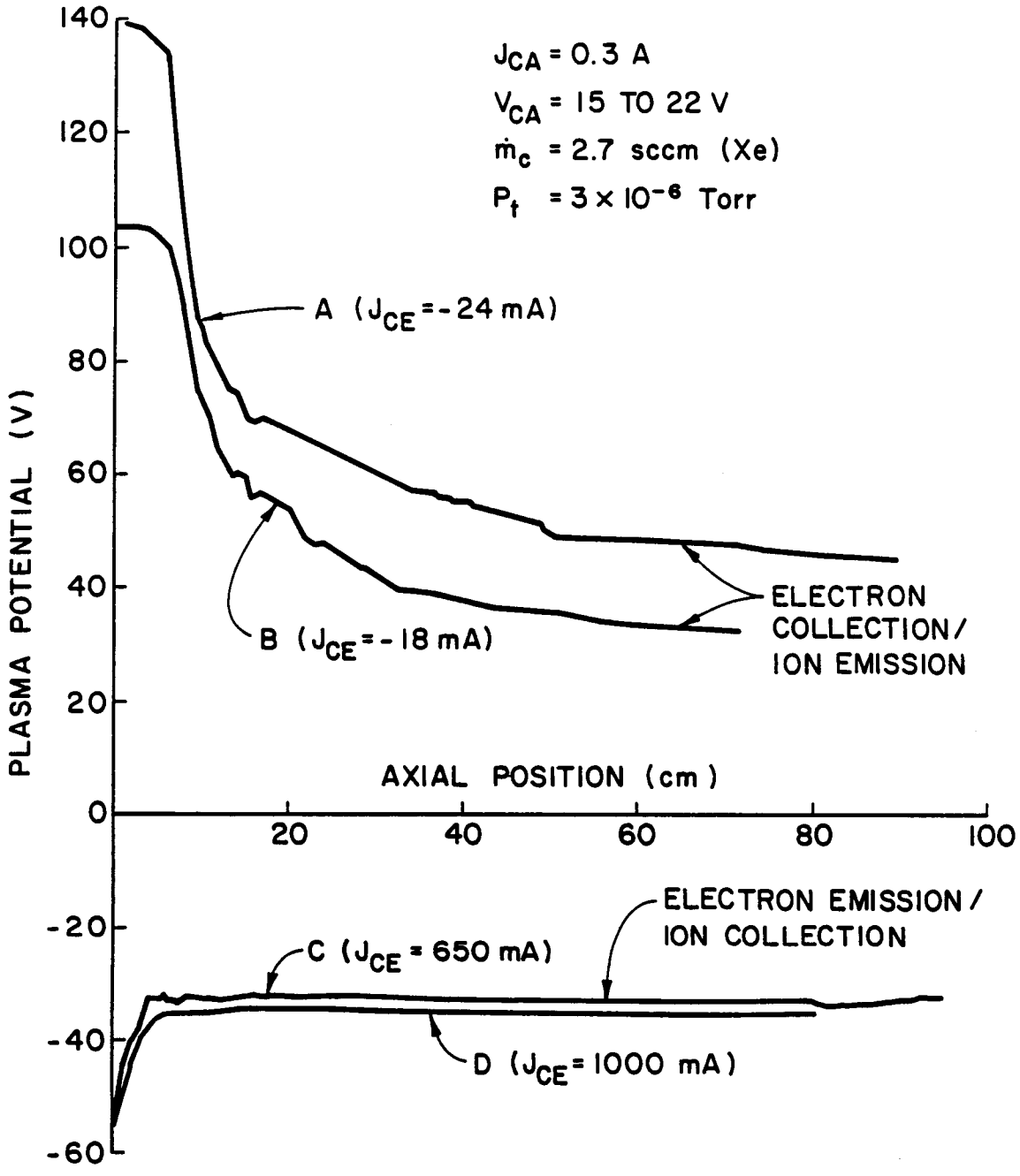

Fig. 13 Typical Plasma Potential Profiles for Conventional Contactor with Simulator on

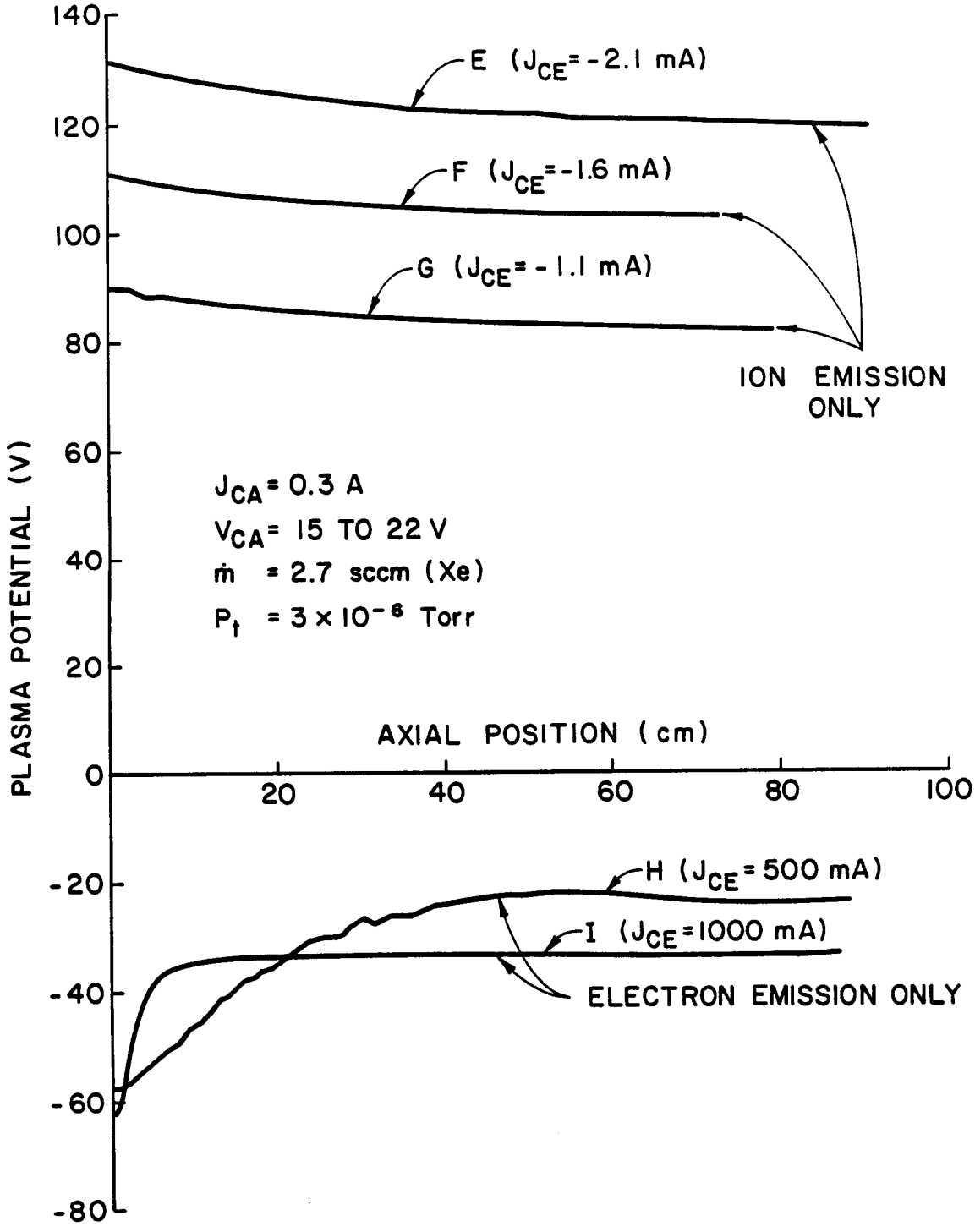

Fig. 14 Typical Plasma Potential Profiles for Conventional contactor with Simulator off

potential plasma adjacent to the contactor followed by a region of steep potential variation and a final region of near constant potential (i.e. they show the double sheath structure identified by the solid line in Fig. 9a). Curves E, F, and G show ion emission only profiles which remain relatively constant at a plasma potential ~20 V below the contactor anode throughout the 1 m long region that was probed. These curves must drop to zero potential at the tank wall so it is suggested that a large sheath develops near the tank wall and simulator anode which collects the ions being produced in the contactor discharge.

An examination of the data of Fig. 13 suggests that the contactor potential ($V_C + V_{CA}$), used to characterize plasma contactor performance in curves like those in Fig. 8 and 12, reflects a higher potential drop than the one actually observed between the contactor and the simulated space plasma. For Curve A in Fig. 13 for example, the contactor potential (i.e. the contactor anode-to-tank potential difference) is 140 - 0 = 140 V while the contactor anode to simulated space plasma potential drop (V_s) identified in Fig. 7 is only 140 - 50 = 90 V. Similarly for Curve D the magnitude of the contactor potential would be 58 - 0 = 58 V while the more correct magnitude (V_s) would be 58 - 37 = 21 V. Use of this contactor sheath potential drop (V_s) removes the potential drop experienced across the sheaths at the tank wall and simulator from the characterizing potential describing plasma contactor performance. Unfortunately most of the data collected during the grant period did not include ambient plasma potential so most of the performance data are presented herein in terms of contactor potential. Where the contactor potential ($V_C + V_{CA}$) has been used in this report as the characterizing potential instead of the observed sheath potential drop across the contactor, the resulting curves are pessimistic representations of the performance of a particular contactor. However, since the simulator operating conditions have been kept fixed

throughout these tests, trends identified by comparing performance curves plotted in terms of contactor potential can be assumed to be correct.

Tests conducted early in the grant period showed that connecting the simulator cathode to ground as opposed to connecting its anode to ground shifted the electron collection portion of the contactor characteristic curve but left the curves otherwise unchanged. This effect is shown in the data of Fig. 15. The potential offset associated with making this change is similar to the change in reference potential introduced by changing the connection (i.e. about equal to the simulator anode voltage). It was expected however, that changing the point of tank connection to the simulator would make little difference in the characteristic curves if the contactor sheath potential (V_s) were used to plot the curves instead of contactor potential ($V_c + V_{CA}$). This has in fact been observed and consequently, it is argued that changing the simulator reference point shifts the characteristic curve along the horizontal axis when the contactor potential ($V_C + V_{CA}$) is used, but does not change the coupling process occurring at the contactor. When this test was repeated using the variable area anode contactor and the data were presented in terms of the contactor-to-simulated space plasma potential difference rather than the contactor anode-to-simulator anode potential difference the data of Fig. 16 were obtained. These results show that changing the point of connection between the tank and the simulator from the simulator anode to the simulator cathode (i.e. changing the simulator reference point) does not change the contactor's performance characteristics. This result was expected and it again suggests that one should use the contactor-to-ambient plasma potential difference to characterize contactor performance.

Ring Cusp Contactor Optimization Study

Experiments conducted on ring cusp contactors at both NASA Lewis[7] and

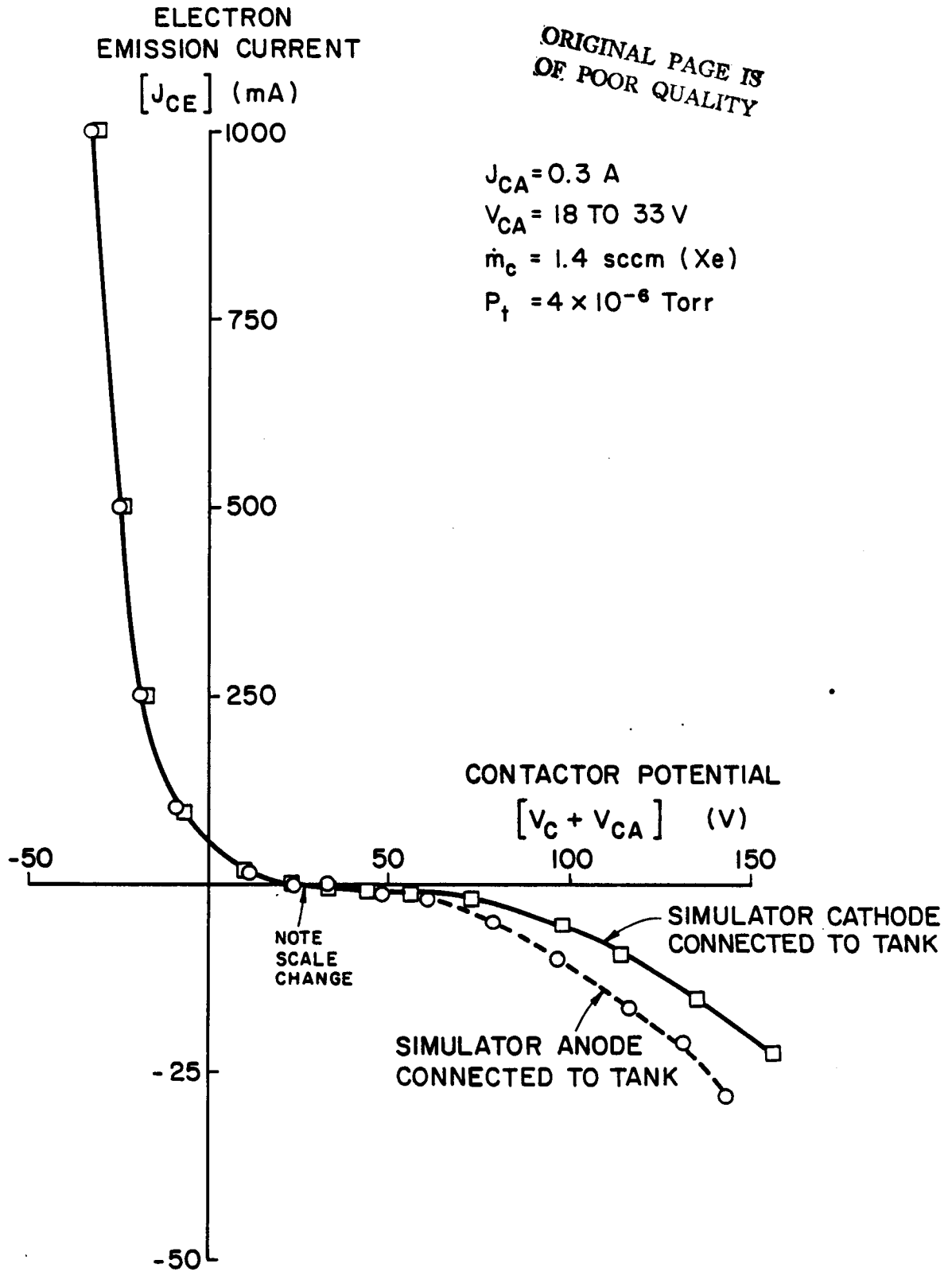

Fig. 15 Effect of Changing Point of Connection to Simulator-Conventional Hollow Cathode Contactor

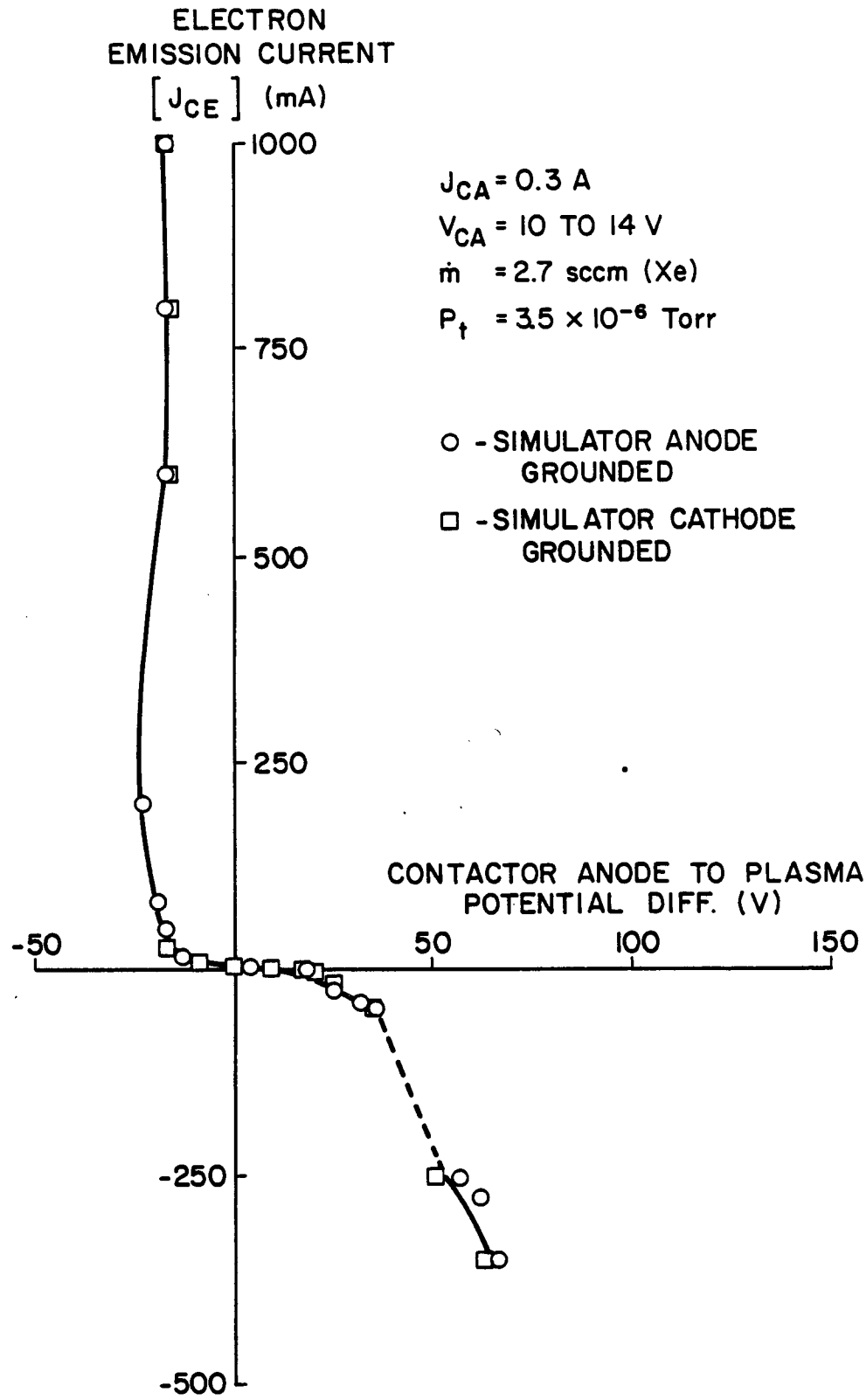

Fig. 16 Effect of Changing Point of Connection to Simulator-12 cm dia Anode Hollow Cathode Contactor

Colorado State University have demonstrated that these contactors are more efficient ion sources than conventional hollow cathodes. This suggests, in light of the model in Appendix A, that they should be better plasma contactors. This conclusion is a consequence of the following logic sequence: 1) Higher ion production rates by a contactor operating at a prescribed power and electron collection current induce an increase in the size of the high density plasma region (r_i in Fig. 2 increases); 2) Because the electron collection current and the ambient plasma density are prescribed, the radius of the outer boundary of the double sheath (r_o in Fig. 2) remains unchanged at a value required to satisfy the condition of equal current densities across this boundary; 3) As a consequence of 1 and 2 the radius ratio r_i/r_o increases and in accordance with the model of Appendix A the voltage drop across the double sheath decreases at the prescribed current level. Hence one concludes that the contactor with the higher ion production would hold a spacecraft closer to ambient plasma potential than a conventional contactor operating at the same current level.

Experiments were conducted on the ring cusp contactor shown in Fig. 7 to optimize its ion production efficiency by adjusting its plasma extraction aperture area. An optimum extraction area was expected because masking down the extraction aperture was expected to induce two competing effects, namely, 1) improvement of neutral atom confinement and hence an increased rate of plasma ion production and 2) reduction of the fraction of these ions that would escape through the smaller extraction aperture. Because of these competing effects an optimum ion production rate was expected at an aperture diameter somewhere between the open ended (no mask) condition of 6.5 cm and zero. This optimum aperture contactor would then be expected to outperform the unoptimized configurations due to its larger extractable ion current at a given operating condition.

The optimum extraction area test conducted on the ring cusp contactor, accomplished using the test apparatus schematic shown in Fig 4a, involved the installation of a series of masks (each having a different aperture area) over the 6.5 cm dia ion source extraction aperture. The masks were moved into place one after the other while the ion source was operating so the effect of changing only the aperture area could be studied. Masks having 2.7, 4.4, 5.5, and 6.5 cm diameter apertures were selected for the study so the aperture area could be changed from 5.7 cm^2 to 33 cm^2 in equal area increments. As the arrangement of Fig. 4a suggests, the mask and the body of the ion source were connected through a switch to a power supply that biased them sufficiently negative so any ions arriving at their surfaces (J_m - ion current to mask and J_b - ion current to body) could be measured. Using these measured currents together with the ion beam current extracted from the source to the vacuum tank, which could also be measured with the simulator off, it was possible to determine the plasma ion energy cost and the extracted plasma ion energy cost over a range of operating conditions. From these measured quantities the parameters defined by Brophy[8] to characterize discharge chamber performance, namely the primary electron utilization factor C_o and the baseline plasma ion cost ε_p^* were computed.

In presenting the data associated with these tests, atomic flowrates will be expressed in milliamperes equivalent (mA eq.). This unit represents the current of atoms that would flow if each atom carried the charge of an electron. It is useful in describing ion source performance because it expresses flowrate in the same units as the ion current being extracted from the ion source. Hence the ratio of ion current to flowrate (the expellant utilization) can be computed directly with no conversion factor if multiply charged ion production is small. Because the sccm unit is more familiar to plasma contactor researchers it will be used to express flowrates for all

contactors except the ring cusp ion source. Conversion between the two sets of units can be made readily be recognizing that a flowrate of 1 sccm of any gas corresponds to 67 mA eq.

The typical plasma ion energy cost curve shown in Fig. 17 pertains to a 4.4 cm dia ion extraction aperture. This curve was obtained by selecting values of C_o and ε_p^* by trial and error and then using them in the discharge chamber model to determine a best fit curve to the measured data points shown. The data were collected by holding the cathode flowrate, $\dot{m}_c$, at 93 mA eq (Xe) and varying the flowrate through the body (main flow plenum), $\dot{m}_b$, from zero to 280 mA eq. (Xe). The scatter in the data about the curve shown in Fig. 17 induced by the changes in flowrate typifies that observed with all of the masks. The systematic scatter about the curve at each flowrate is symptomatic of a minor deficiency in the basic model being applied to describe the curve. This scatter is probably due to changes in baseline plasma ion energy costs that are believed to occur at low discharge voltage conditions, like those being encountered in these tests, that are not considered in the model[8]. Over the range of flows and discharge currents investigated, the discharge voltage varied but it was typically found to be within a few volts of 25 V as indicated in the legend of Fig. 17. Figure 18, which shows a comparison of curve fits obtained for the various aperture diameters investigated, indicates that the smallest diameter aperture (2.7 cm) gives the lowest plasma ion energy cost curve and so from the point-of-view of producing ions only, it would be preferrable. Figure 19 shows the effect of mask aperture diameter on the other important factor, namely the fraction of ions produced that are extracted from the discharge. These data

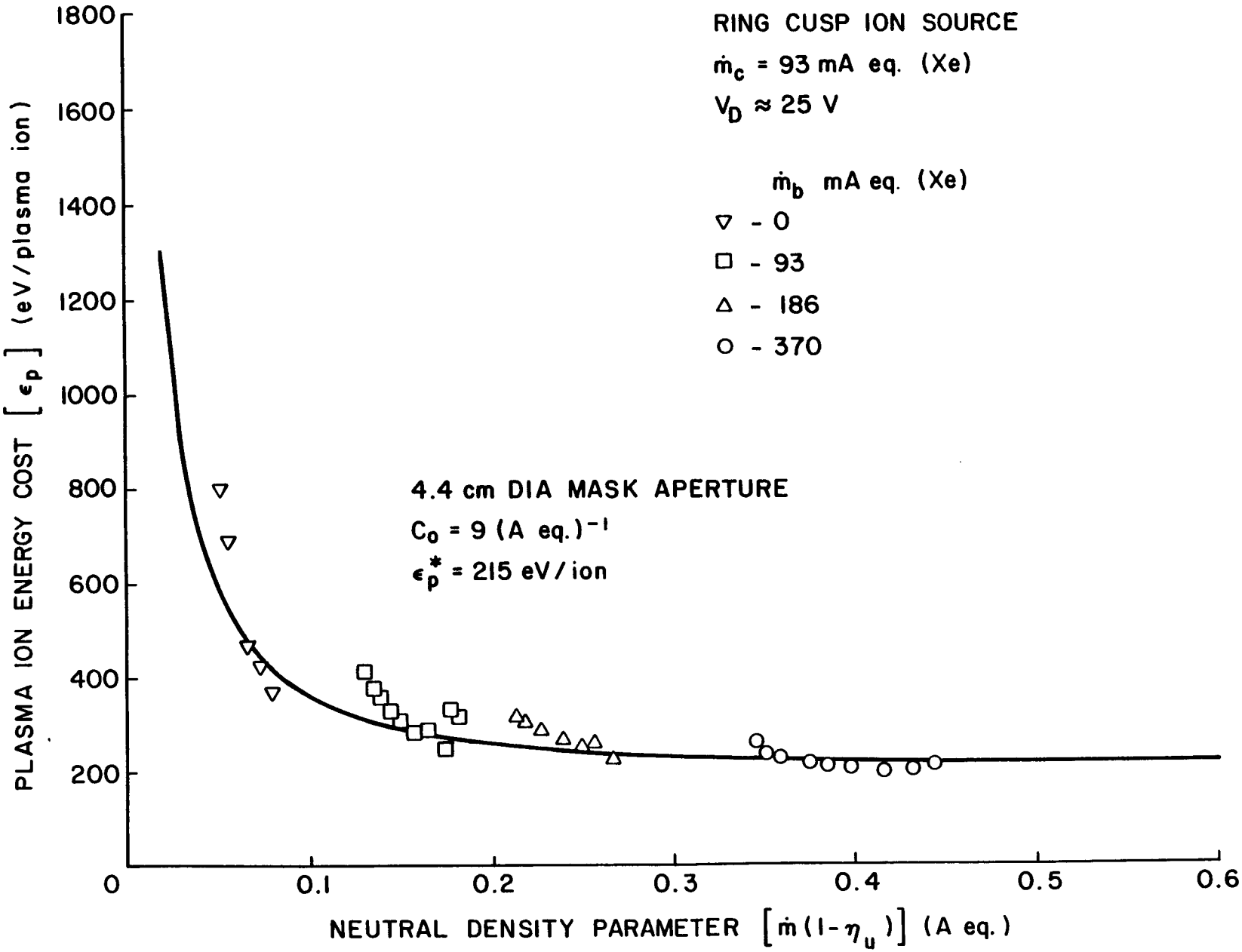
RING CUSP ION SOURCE
$\dot{m}_c$ = 93 mA eq. (Xe)
$V_D \approx 25$ V
$\dot{m}_b$ mA eq. (Xe)
▽ - 0
□ - 93
△ - 186
○ - 370
4.4 cm DIA MASK APERTURE
$C_0 = 9$ (A eq.)$^{-1}$
$\epsilon_p^* = 215$ eV/ion
PLASMA ION ENERGY COST [ϵ_p] (eV/plasma ion)
NEUTRAL DENSITY PARAMETER [$\dot{m}(1-\eta_u)$] (A eq.)
1800
1600
1400
1200
1000
800
600
400
200
0
0.1
0.2
0.3
0.4
0.5
0.6

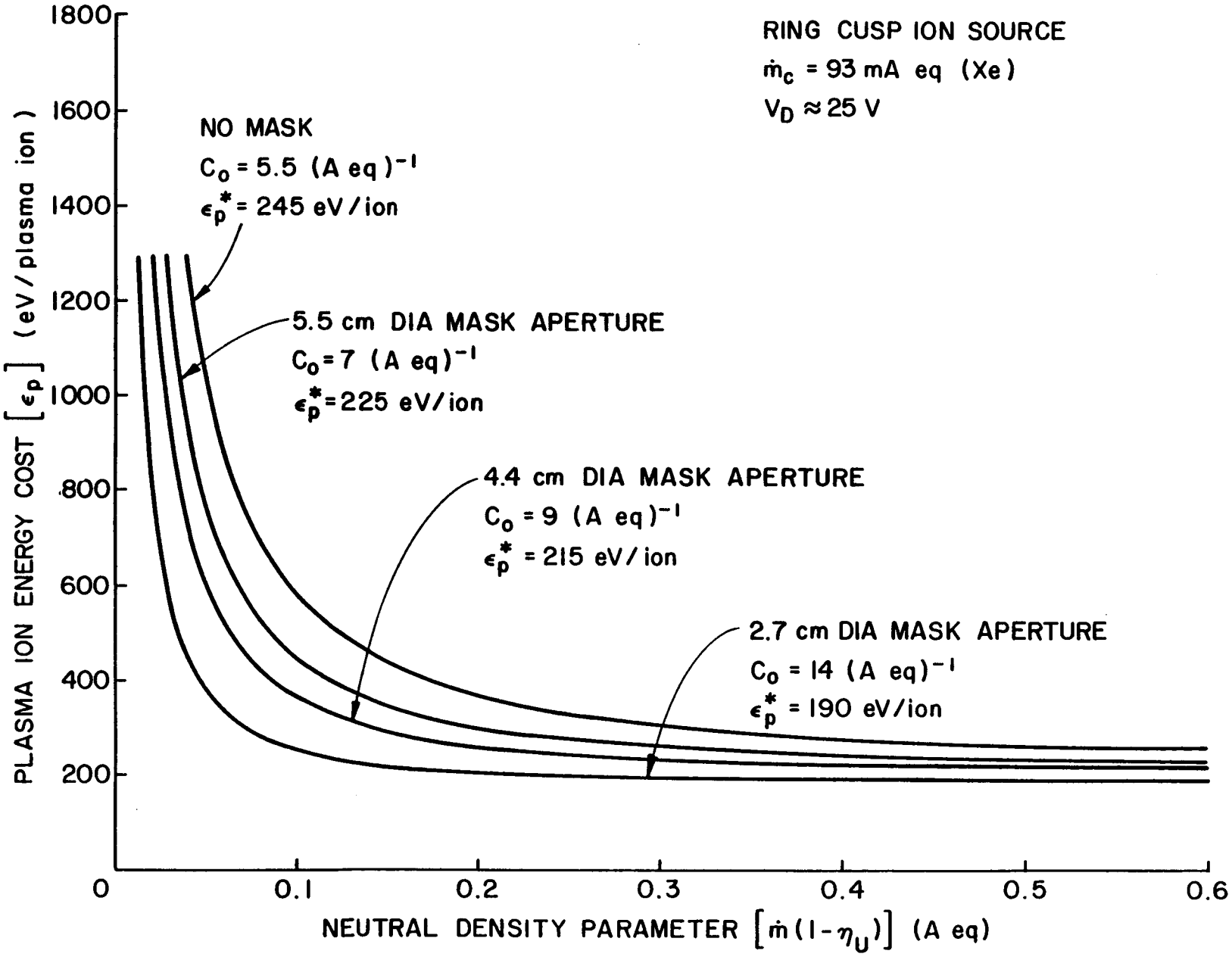

Fig. 18 Effect of Mask Aperture Diameter on Plasma Ion Energy Cost Curves

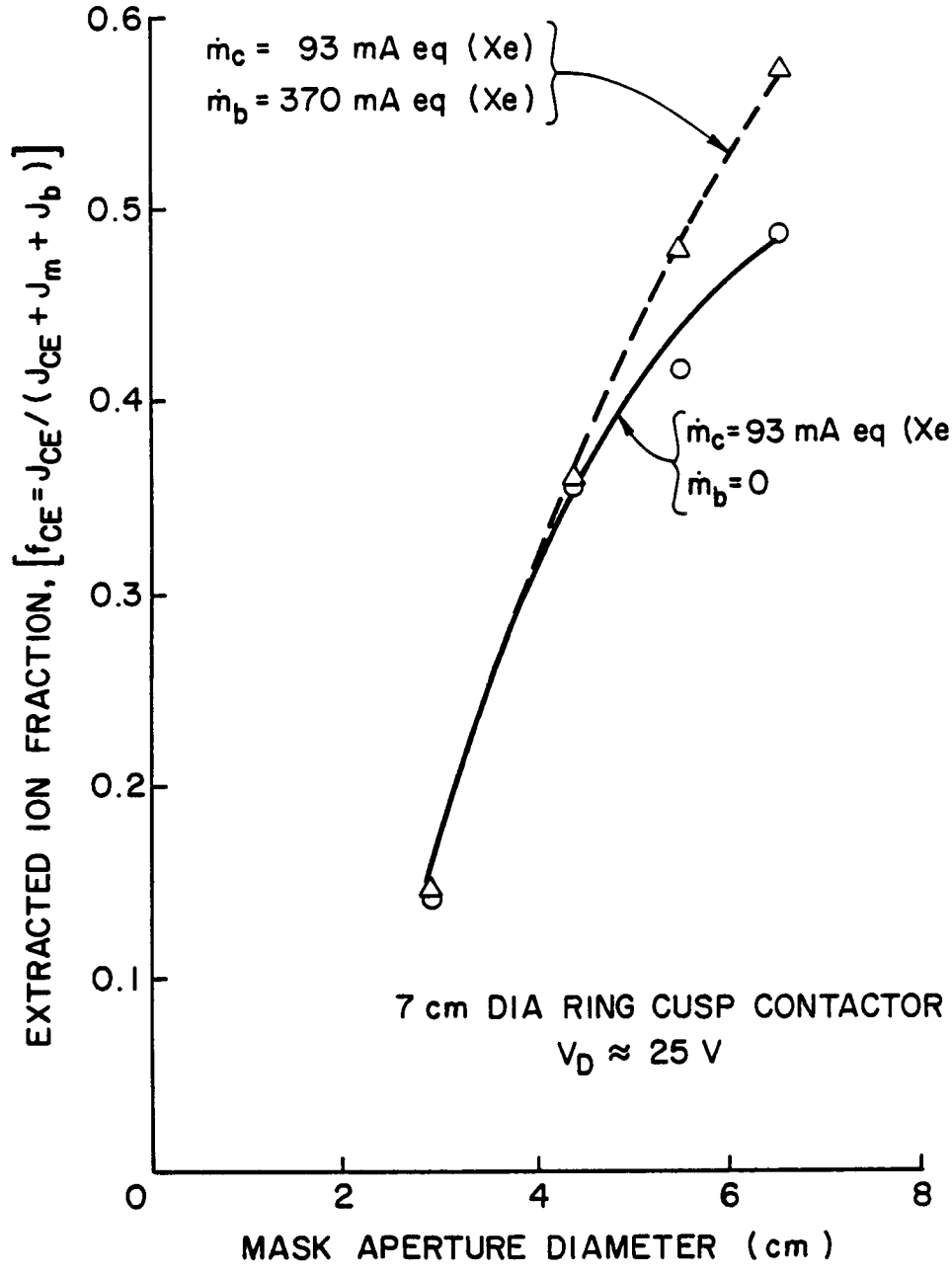

Fig. 19 Effect of Mask Aperture Diameter on Extracted Ion Fraction

indicate that the larger the mask aperture the greater the fraction of ions produced that escape through the aperture. Note in regard to the data of Fig. 19 that the extracted ion fraction is affected by flowrate when the mask diameter is large. Discharge power did not cause the extracted ion fraction to change, however, and this was expected based on the discharge chamber model.[8]

Considering the data of Figs. 18 and 19 together it is apparent that increasing the mask aperture diameter has the beneficial effect of increasing extracted ion fraction and the detrimental effect of increasing plasma ion energy cost. Hence there will be a diameter at which these effects will balance and contactor performance will be optimal. By plotting the extracted ion energy cost versus expellant utilization at a particular flowrate in the manner suggested in Fig. 20, the optimum mask aperture diameter is found to be 5.5 cm. This plot demonstrates that reducing the aperture area from 6.5 cm to 2.7 cm in increments causes the curves to move down and to the right and then back up and to the left again. Since the preferred curve is the one lowest and furthest to the right Fig. 20 suggests that the 5.5 cm dia aperture yields the highest extracted ion production rate per unit energy expenditure. All flowrates investigated yielded the same 5.5 cm dia mask aperture as the optimum, however, increasing the flowrate through the plenum was found to improve the ion production performance of the source. This result, shown in Fig. 21, is a reflection of effect of flowrate on extracted ion fraction indicated by the data of Fig. 19.

It is also of interest to determine whether changing the extraction aperture diameter of the ion source affects its ability to emit electrons to or collect electrons from a simulated plasma. In order to determine this, the

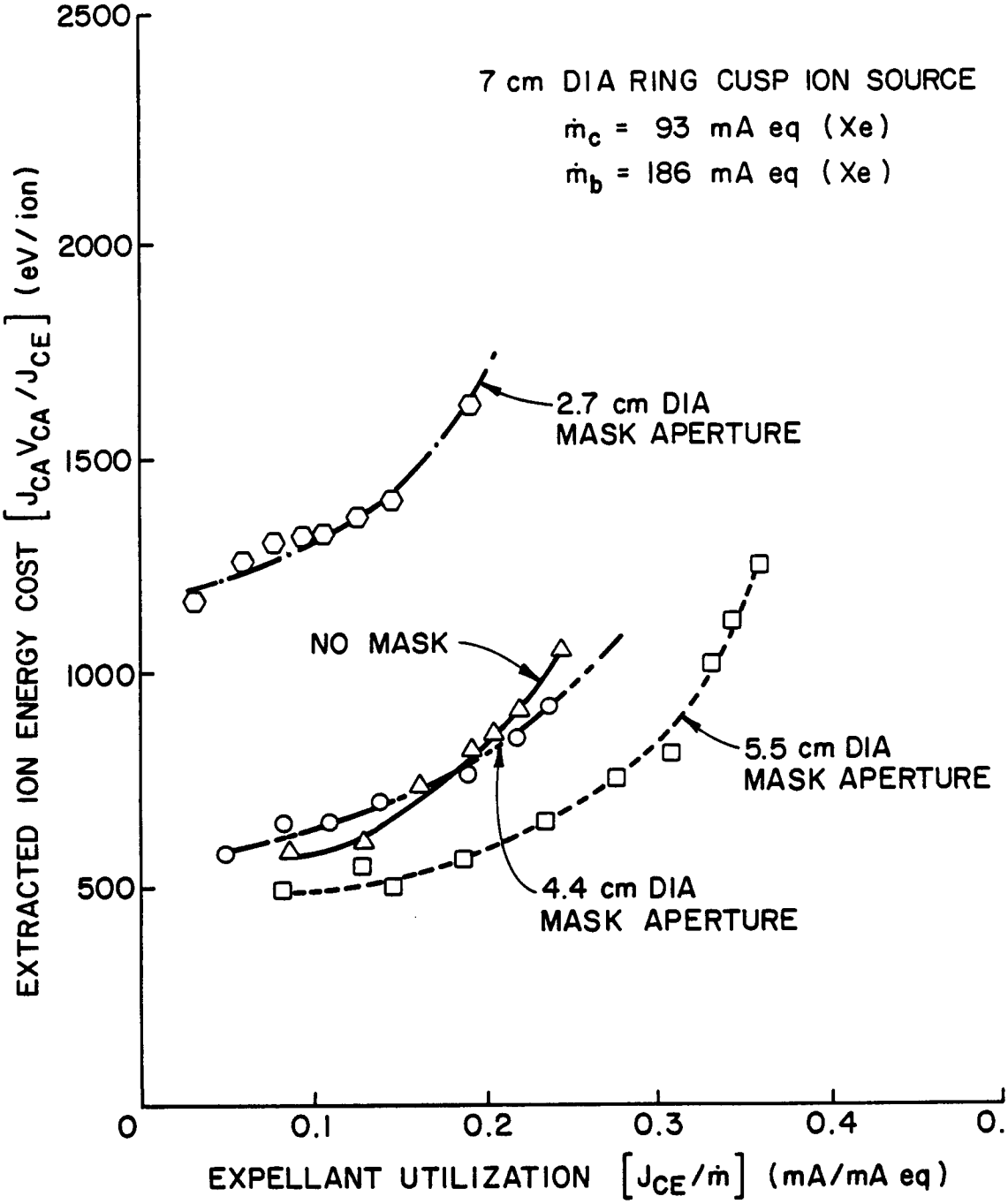

Fig. 20 Effect of Mask Aperture Diameter on Extracted Ion Energy Cost

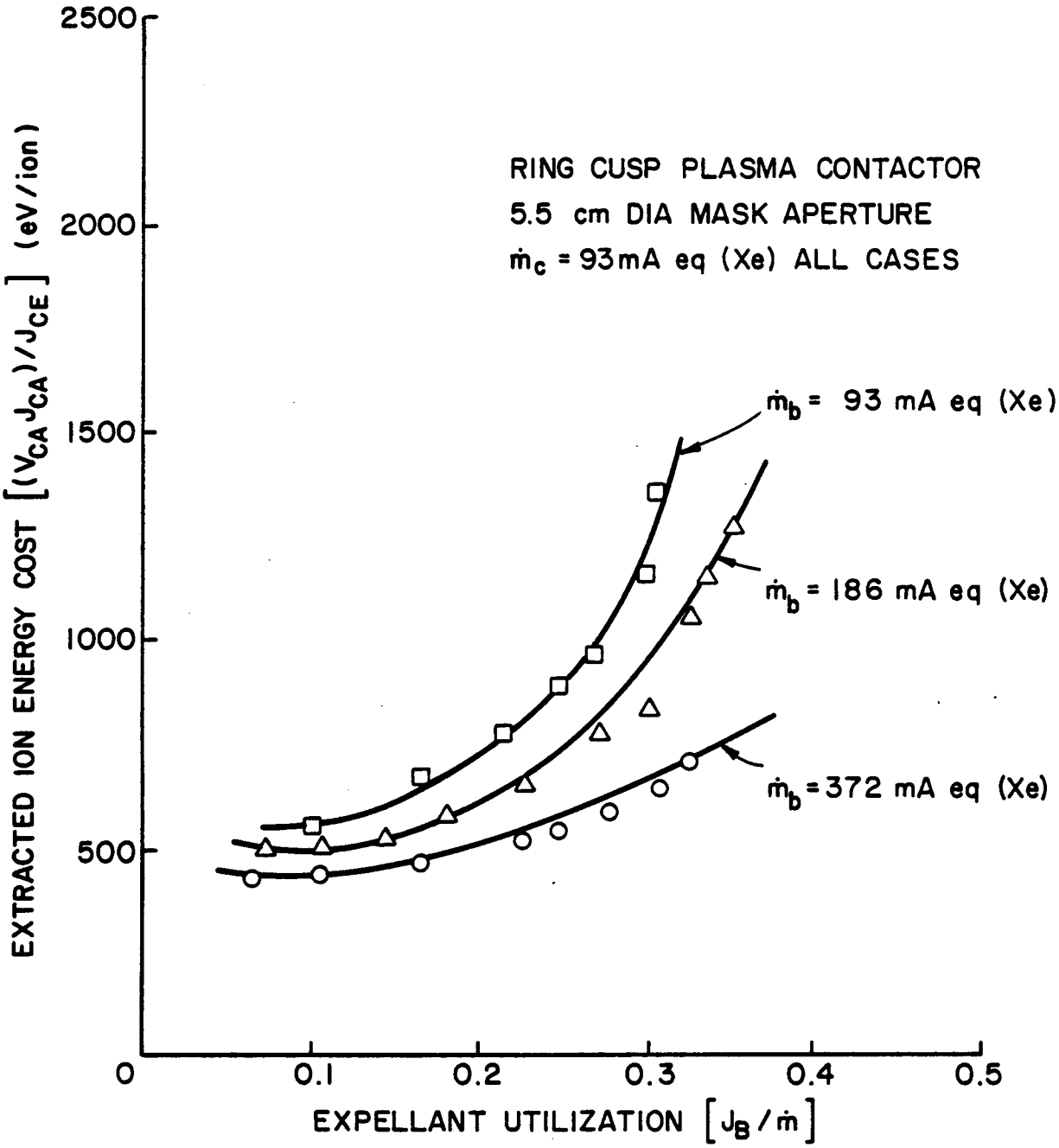

Fig. 21 Effect of Flowrate on Ring Cusp Contactor Ion Cost

simulator was started and the ring cusp contactor was biased using the coupling supply to effect electron emission and collection through the various mask aperture diameters investigated. Figure 22 shows the characteristic curves measured in this way at a contactor discharge power of ~20 W. The curves suggest that installing masks with aperture diameters varying from 4.4 to 6.5 cm results in essentially the same characteristics although the one for the 5.5 cm dia mask does seem to be the best. Note that the very small mask aperture (2.7 cm dia) appears to cause the ion source to perform substantially poorer. Since the spherical double sheath model[3] suggests that reducing the effective radius of the plasma surface from which ions are drawn in the electron collection mode or electrons are drawn in the electron emission mode causes the sheath voltage to increase at a prescribed current level a degradation of performance with this low aperture area was expected. The conclusion of this work is that there is an optimum aperture which should effect the most efficient operation of a plasma contactor. For the 6.5 cm dia ring cusp contactor this aperture diameter is approximately 5.5 cm.

Effect of Anode Area on Contactor Performance

A comparison of typical performance curves observed with the conventional hollow cathode contactor with those associated with the ring cusp plasma contactor (e.g. Fig. 12 vs. Fig. 22) shows that the ring cusp contactor performs better than the conventional one , especially in the electron collection region. It has been suggested in this report that this could be because the ring cusp contactor has a higher ion production rate than the conventional contactor, and it has also been suggested that it could be because the effective area of the ring cusp contactor for contacting the ambient space plasma

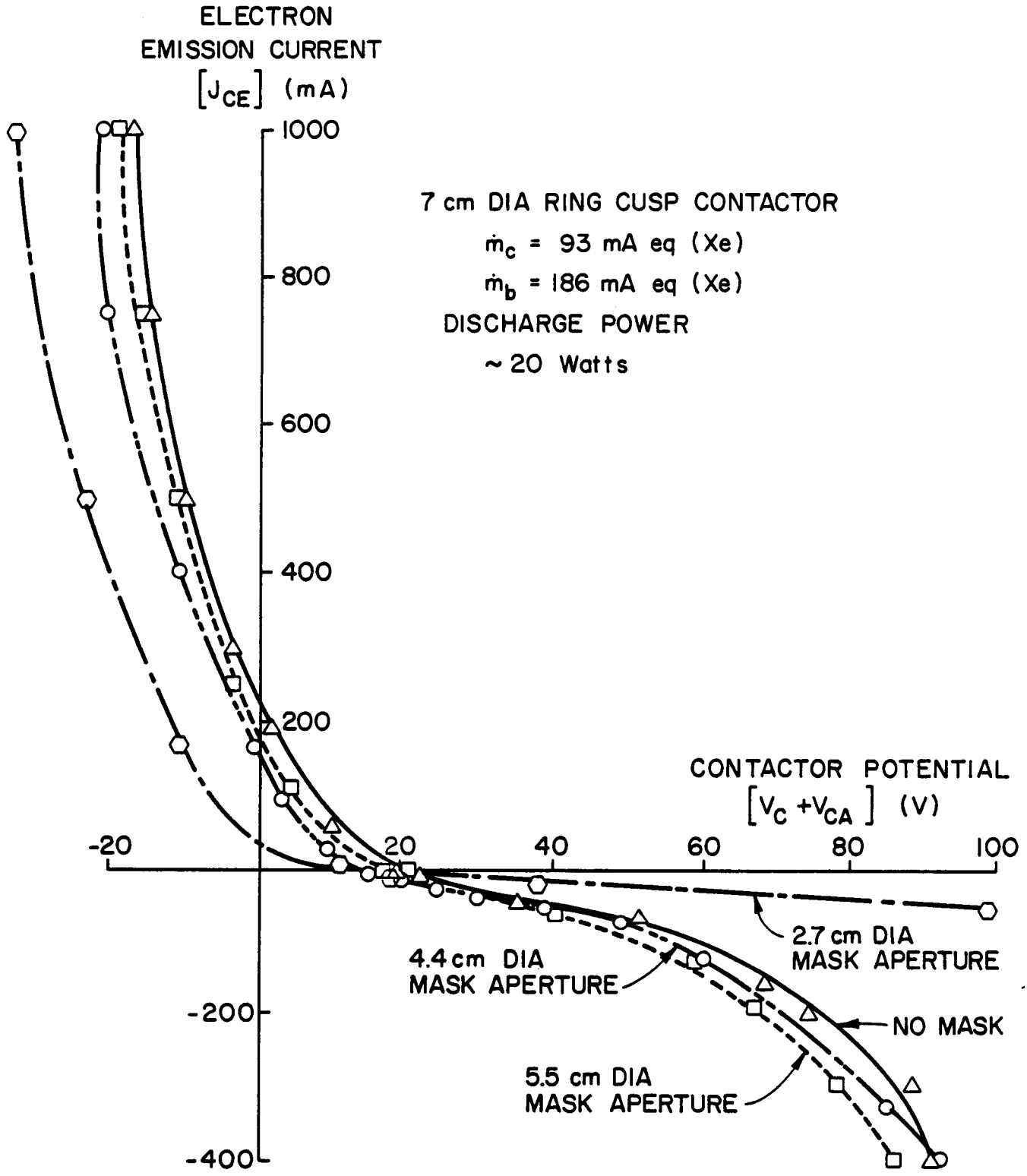

Fig. 22 Effect of Mask Aperture Diameter on Ring Cusp Contractor Performance

is larger than that for the conventional cathode (6.5 cm for the ring cusp contactor vs. 8 mm for the conventional contactor). In order to investigate the effect of anode area on the performance of a contactor, the apparatus shown in Fig. 7 was constructed. It consists of a conventional hollow cathode with a sustaining anode that is identical to the conventional contactor with three added (auxiliary) surfaces that can either be held at anode potential or allowed to float. When floating, it is assumed that these surfaces do not participate significantly in the contacting process and since they can be switched between the floating and the anode potential conditions during operation using the circuity shown in Fig. 4b, the effect of anode area on contactor performance can be examined readily. Curves showing the effect of changing the anode diameter on contactor performance are presented in Fig. 23. Data points have been left off of these curves because of the large number of curves and the tendency for the data points to overlap and clutter the figure, however, the individual curves are representative of the actual performance of the contactor observed. These curves show that with either the sustaining anode or the sustaining anode and anodes 1 or 2, the performance is similar to tne performance of the conventional contactor in the electron collection region, i.e. the electron collection currents are in a range less than 100 mA. However, when anode 3 or all of the anodes are connected the contactor undergoes a transition to what has been termed the ignited mode of electron collection. In this mode a substantial increase in the electron collection current to values over a few 100 mA at potentials less than 100 V are observed. Visual observation of the contactor discharge during these transitions has shown that the transition to the ignited mode is accompanied by the development of a luminous plume having a size similar to the outer diameter of

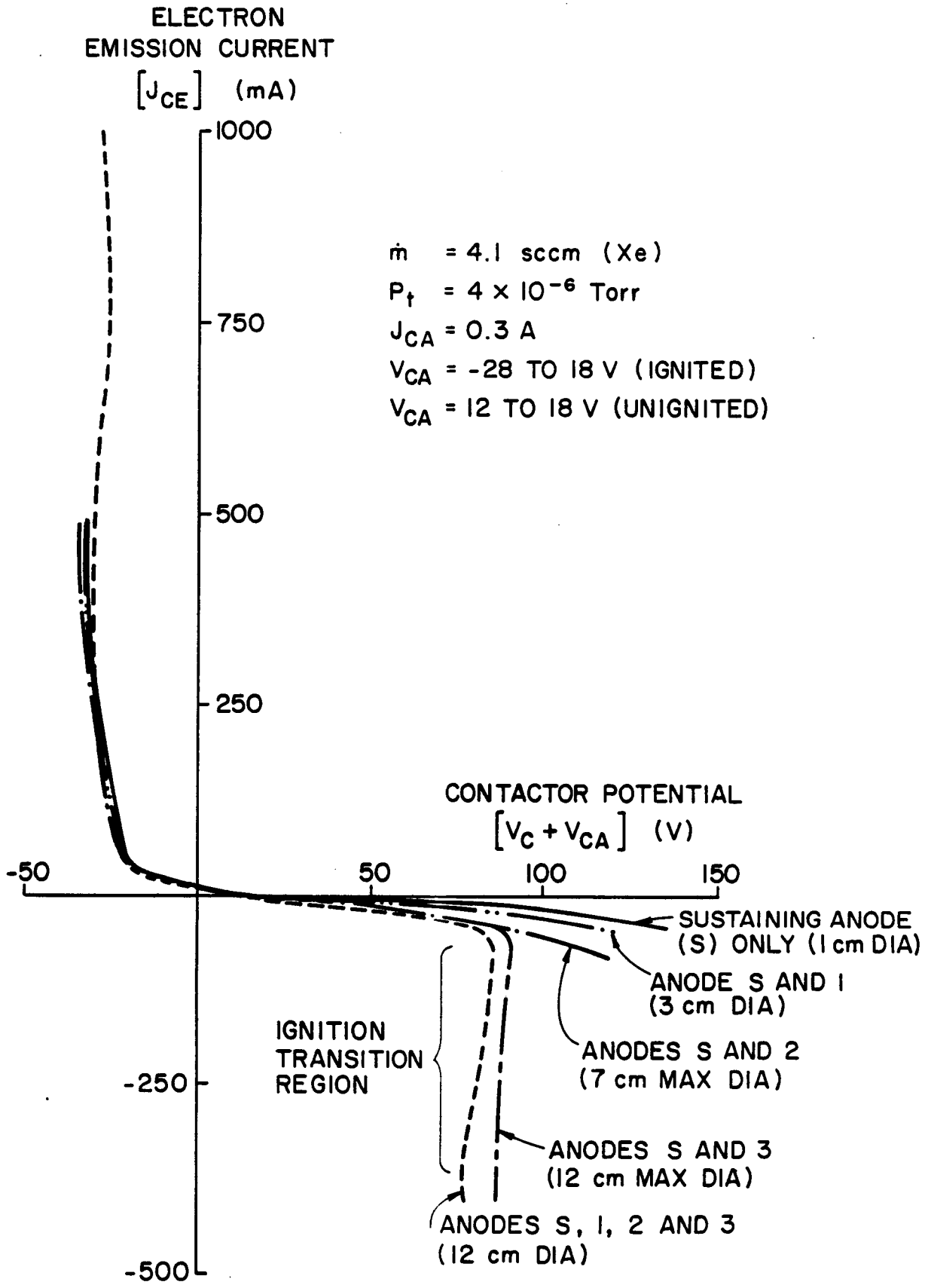

Fig. 23 Effect of Anode Diameter on Contactor Performance

the 3rd anode. Since the observed luminousity is due to atomic or ionic excitation it is suggested that ionization is also occurring and that it could be the cause of the improved contacting performance accompanying the transition to ignited mode electron collection. Figure 24 is a typical comparison of the electron current collected by the contactor (J_{CE}) compared to the electron emission current from the simulator (J_{SE}). These curves are similar and because there is no substantial change in the degree of agreement between them it is argued that the transition to the ignited mode indeed results from plasma phenomena, and not from electron currents being drawn from the vacuum tank walls.

Figure 25 shows a series of plots obtained using the 12 cm dia anode contactor operating under conditions similar to those associated with Fig. 23 but where the contactor discharge did not undergo transition to the ignited mode. The data of Fig. 25 were collected soon after the ignited mode of electron collection was first observed and in this particular test transition to ignited mode operation with the large diameter anode could not be effected. It was believed at the time that transition to the ignited mode was inhibited by an insulating layer of fractionated diffusion pump oil on the anodes that prevented them from functioning properly. When the anode discoloration was removed after the test, transition to ignited mode operation was achieved readily. Since that time, however, the varible anode area contactor has been operated for long periods of time and has become coated to the point where its appearance was worse than it was during this early test. Yet, transition to ignited mode operation has been initiated regularly with no difficulty. This suggests that the coated anode was not the reason for the inability to induce the transition. More recent tests indicate that transition to ignited mode operation may be affected by small changes in simulator

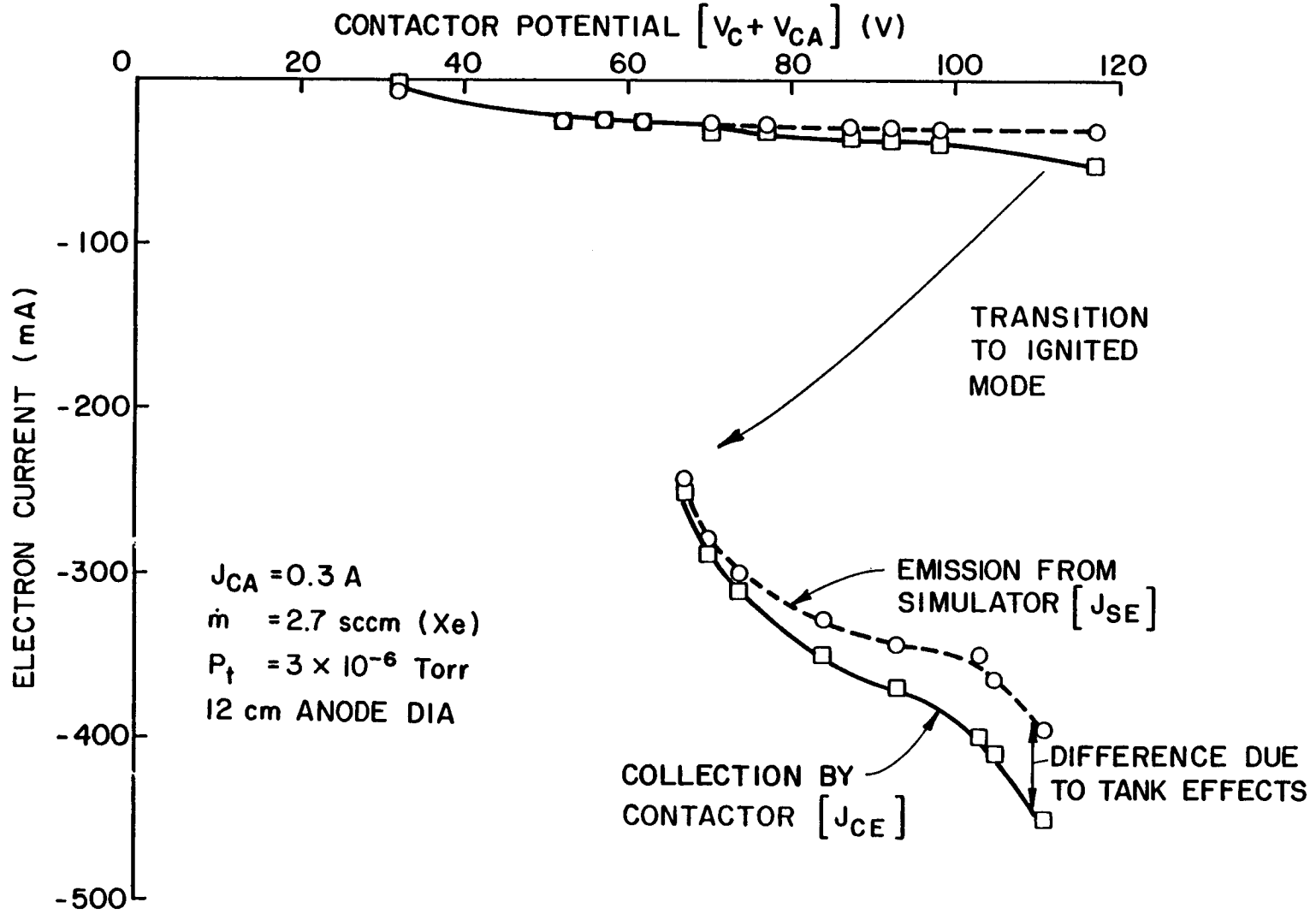

Fig. 24 Perturbing Effect of Vacuum Tank Walls

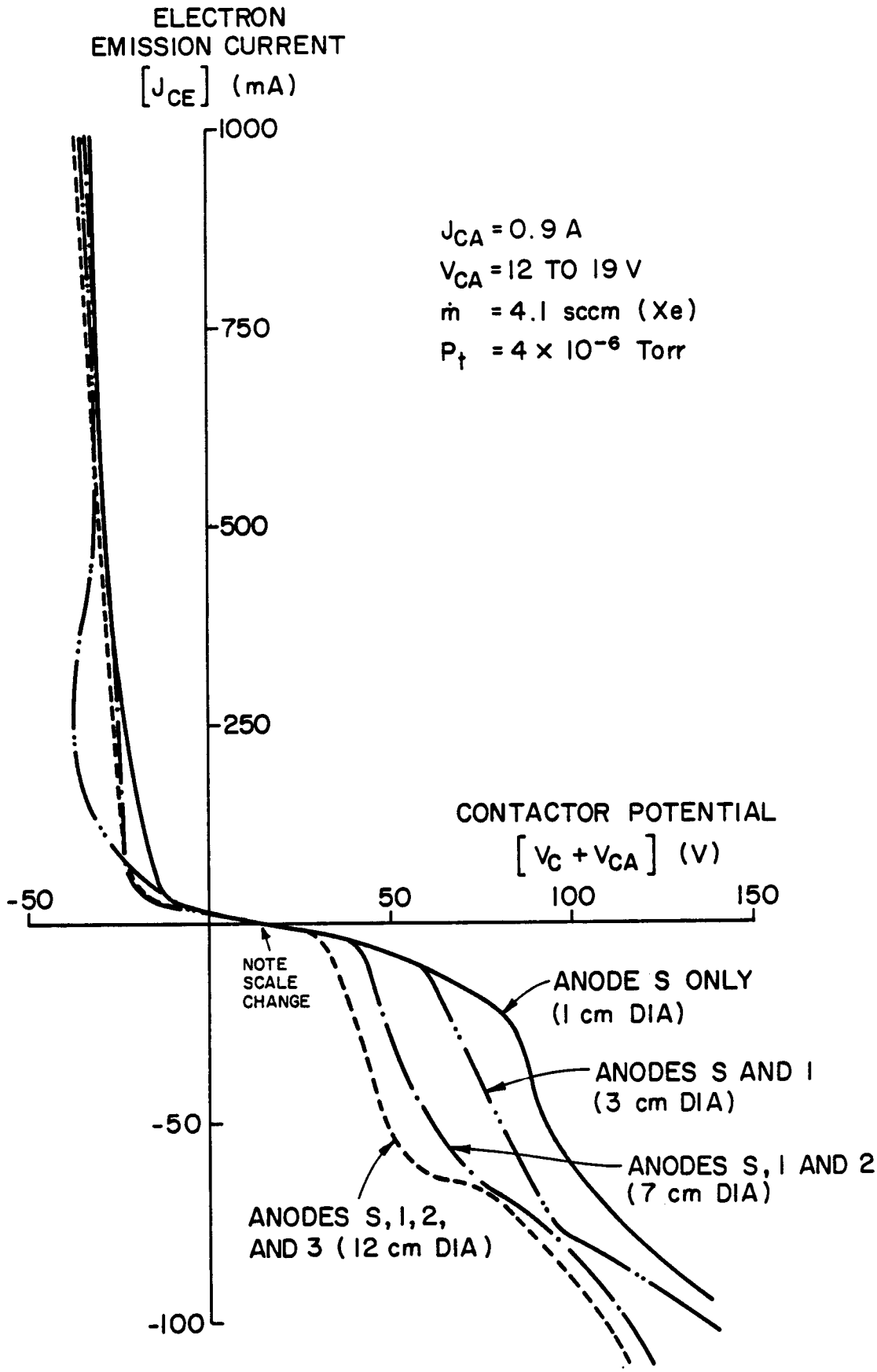

Fig. 25 Anomolous Contactor Performance Curves

operating conditions. At this point it is uncertain why occasional difficulties are encountered in achieving ignited mode operation.

Figure 26 shows the effect of contactor anode current J_{CA} on the transition into ignited mode operation for an anode dia. of 12 cm. These data suggest that increases in the contactor anode current caused the transition to ignited mode operation to shift to progressively lower contactor potentials. If the contactor flowrate is increased from 1.4 sccm to 4.1 sccm the contactor potential at which this transition occurs becomes relatively unaffected by the contactor anode current as shown in Fig. 27. Comparison of Figs. 26 and 27 shows, however, that the increased xenon flowrate itself induces a substantially decreased contactor potential at which the transition occurs. A further increase in contactor flowrate to 6.8 sccm induces an additional decrease in the contactor potential at which this transition occurs as the data of Fig. 28 indicate.

Typical voltage/current characteristic curves for the 12 cm dia anode contactor operating with and without the simulator on are shown in Fig. 29. The data on these two curves can be compared with those of Fig. 12 to see the effect of increasing the contactor anode diameter on the performance curves. This comparison shows that curves obtained with the simulator off are essentially identical while those associated with the simulator on exhibit a dramatic increase in the electron collection current beyond the point of transition into the ignited mode of electron collection. Comparison of the data shows that the contactor anode voltages (V_{CA}) observed over the full range of electron emission currents are the same (i.e. this voltage is independant of the anode diameter). At each of the solid data points identified in Fig. 29, plasma potential profiles along the tank centerline downstream of the contac-

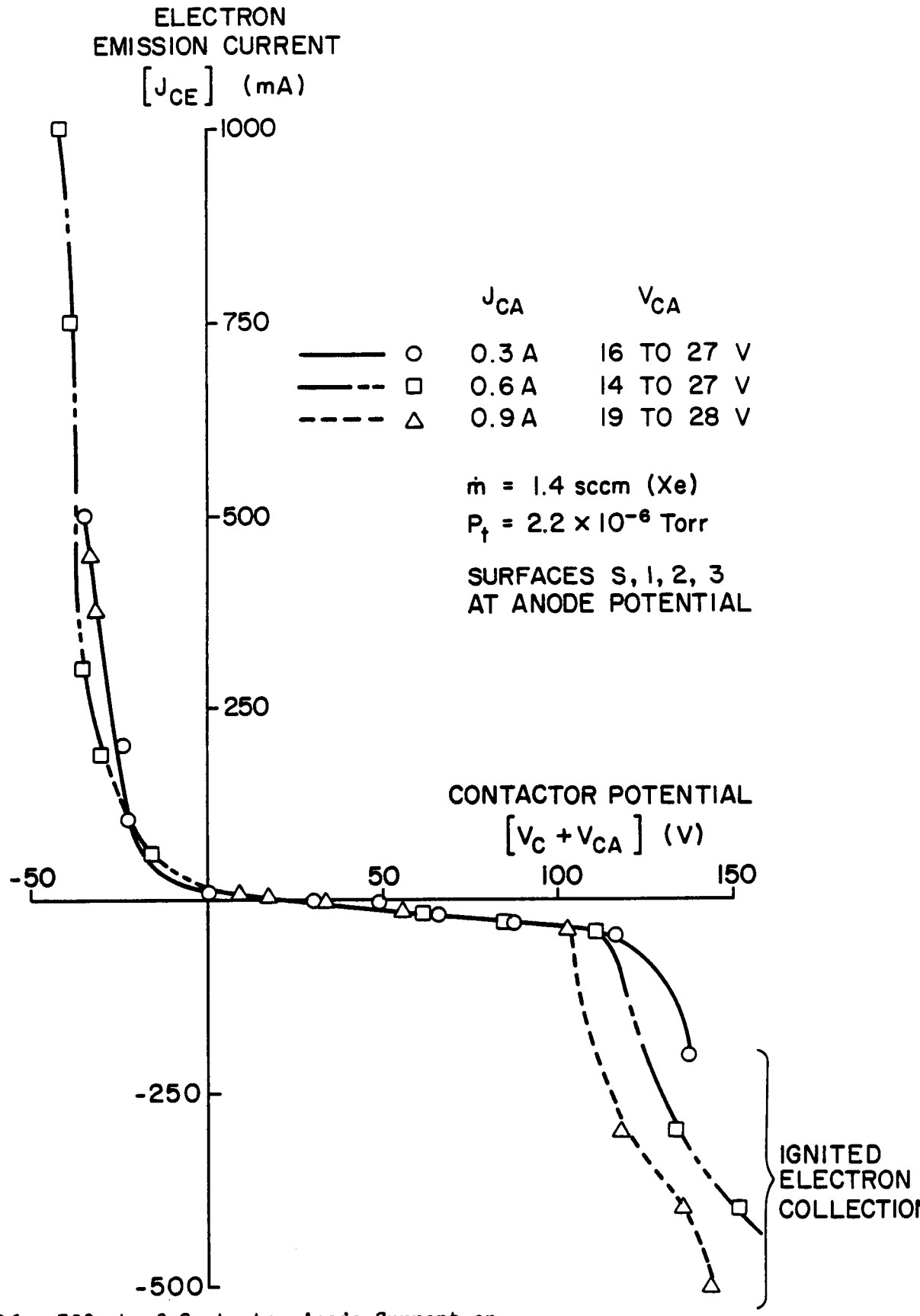

Fig. 26 Effect of Contactor Anode Current on Performance at Low Flowrate

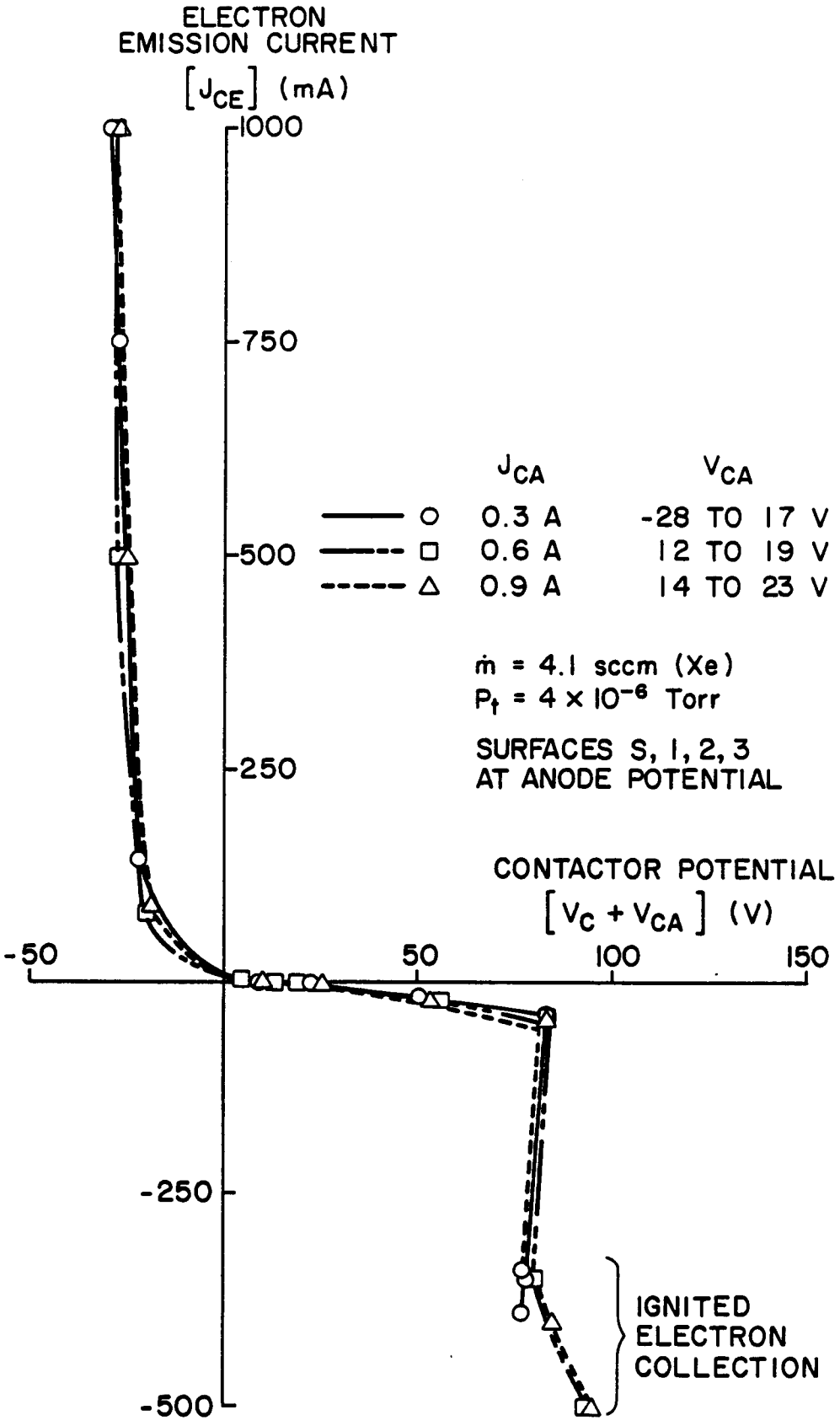

Fig. 27 Effect of Contactor Anode Current on Performance at a Moderate Flowrate

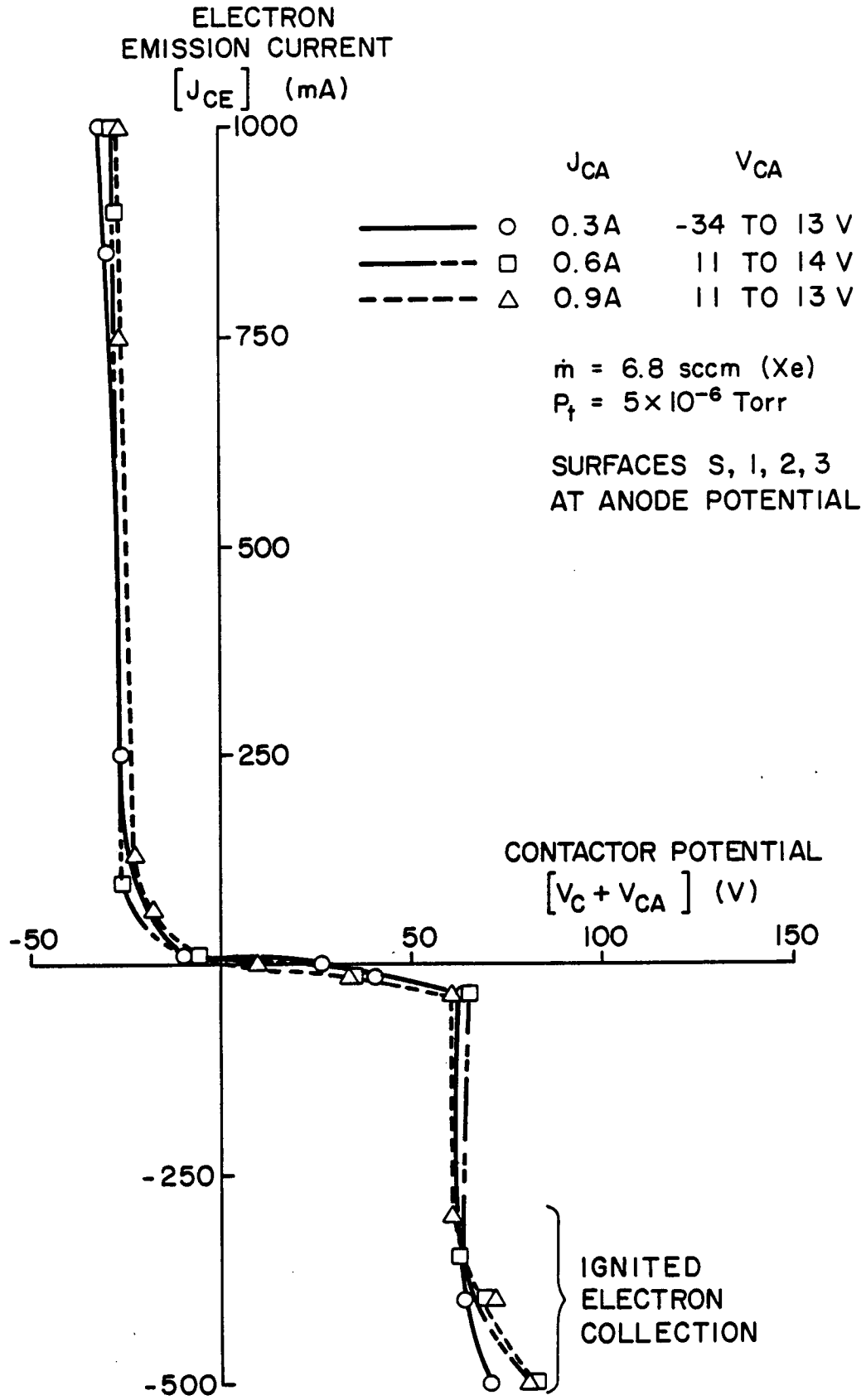

Fig. 28 Effect of Contactor Anode Current on Performance at a High Flowrate

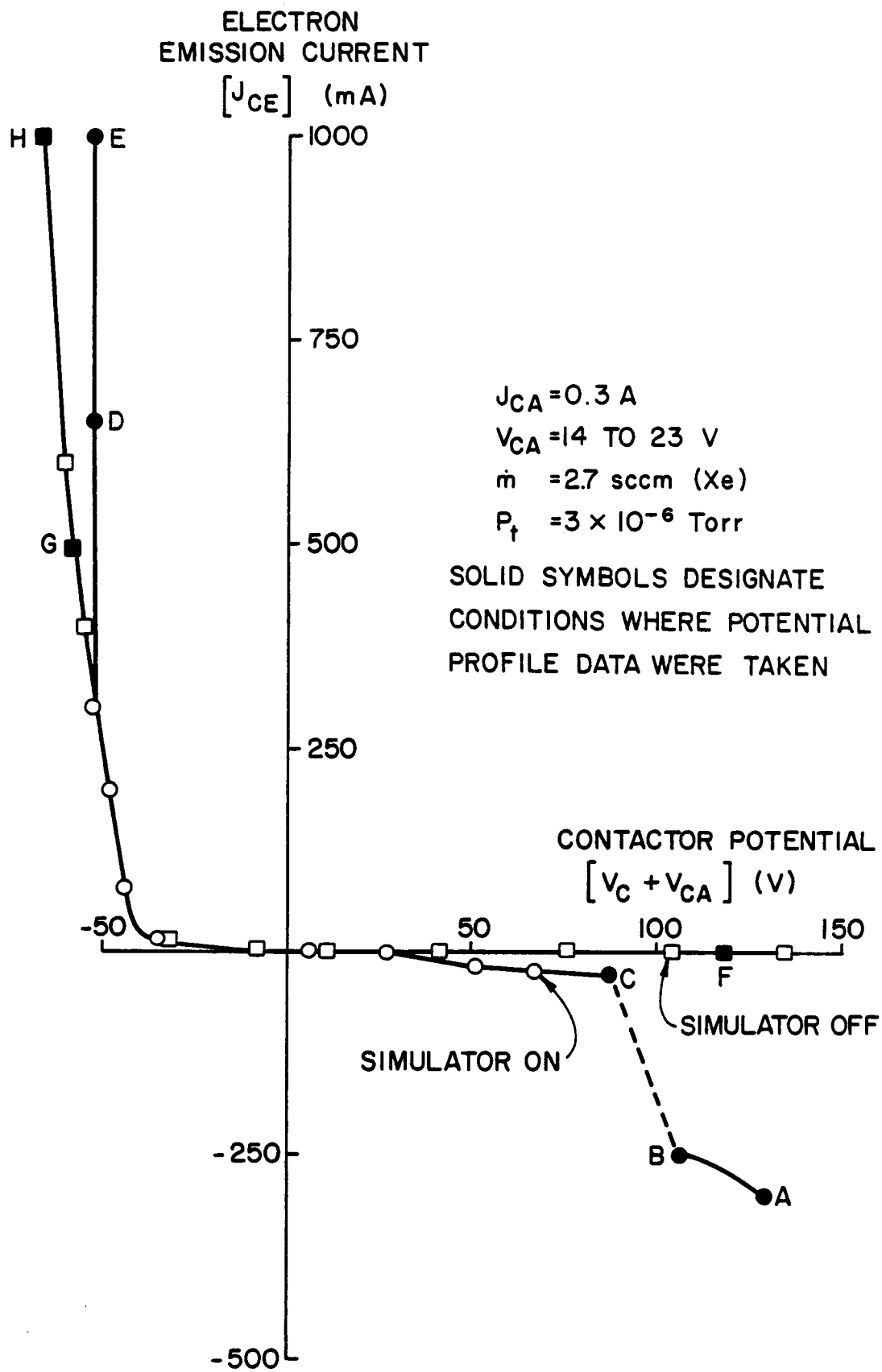

Fig. 29 Typical 12 cm Dia. Anode Contactor Characteristics

tor were measured using the emissive probe. These profiles are identified in Fig. 29 by letter and also in Figs. 30 and 31 by the same letter for the two situations being considered (simulator on and off). Under conditions of the higher electron emission currents (Curves D, E and H) relatively flat potential profiles are observed except within about 5 cm of the contactor, where a voltage drop indicative of a sheath exists. In case G where the simulator is off and the contactor emission current is the lowest, this sheath extends considerably further downstream. It is noted that the same behavior was observed in the curves obtained in Figs. 13 and 14 for the conventional contactor. The similarity of these curves indicates that the anode size has no significant effect on contactor performance when it is operating in the electron emission mode. Note also that the shapes of all of these curves suggest the existence of a sheath. It would be a single sheath when the contactor is emitting electrons to the tank in the case where the simulator is off (Curves G and H) and it would be a double sheath in the case of Curves E and D where electrons are being emitted and ions are available to be drawn from the simulated space plasma.

Under conditions of electron collection/ ion emission (Curves A, B, C and F) the plasma potentials associated with the profiles are positive relative to the tank. With the simulator off (Curve F) the profile is quite flat and is almost identical to the profile observed with the conventional contactor at an ion emission current near 1.4 mA. In general the curves obtained with the simulator on (Curves A, B and C) show a region of relatively constant plasma potential adjacent to the contactor followed by a region of steep potential variation and a final region of relatively constant potential. These profiles are also similar to those obtained in the electron collection mode with the conventional conatactor (Fig. 13).

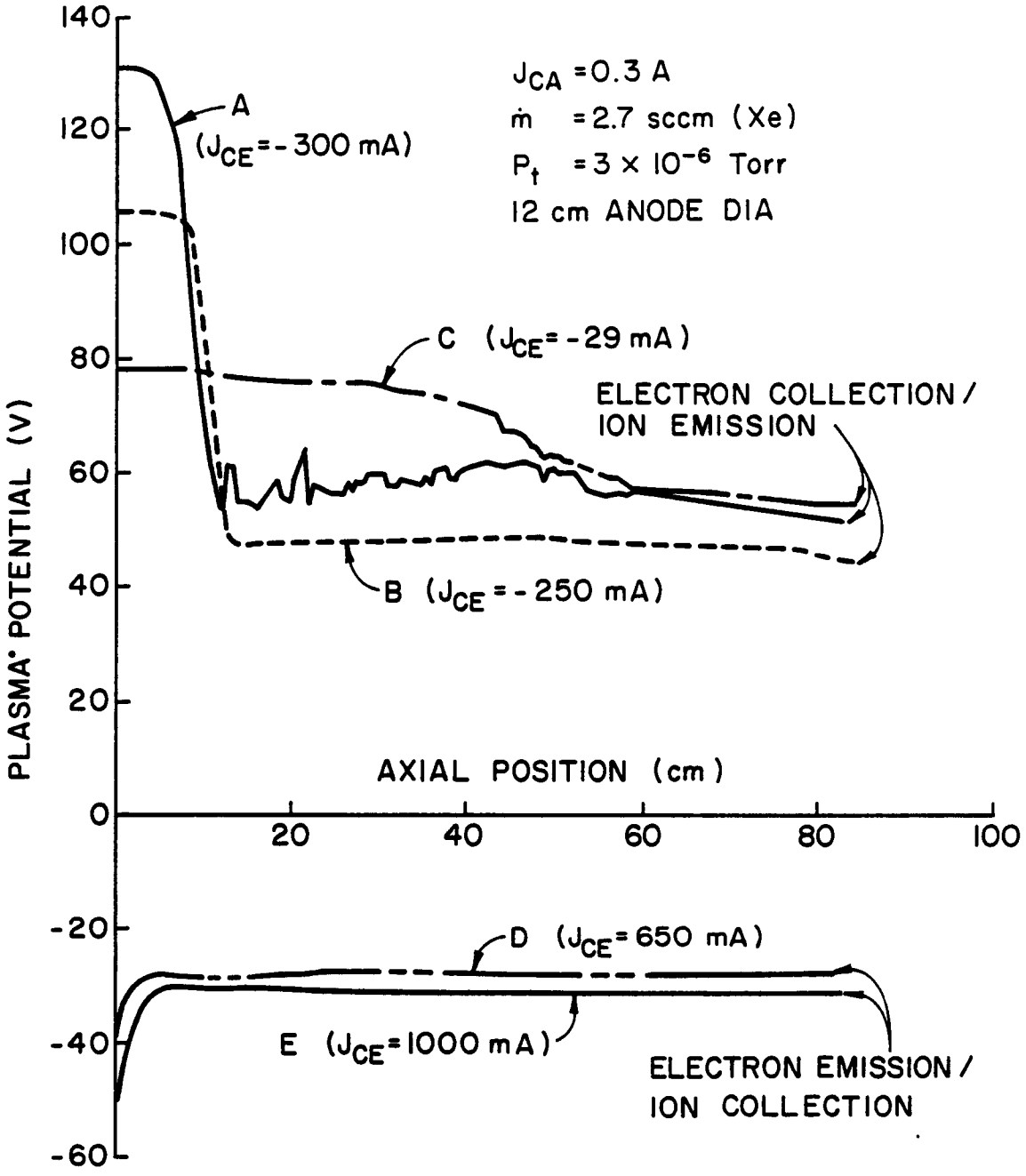

Fig. 30 Typical Plasma Potential Profiles for the 12 cm Dia. Anode Contactor-Simulator on

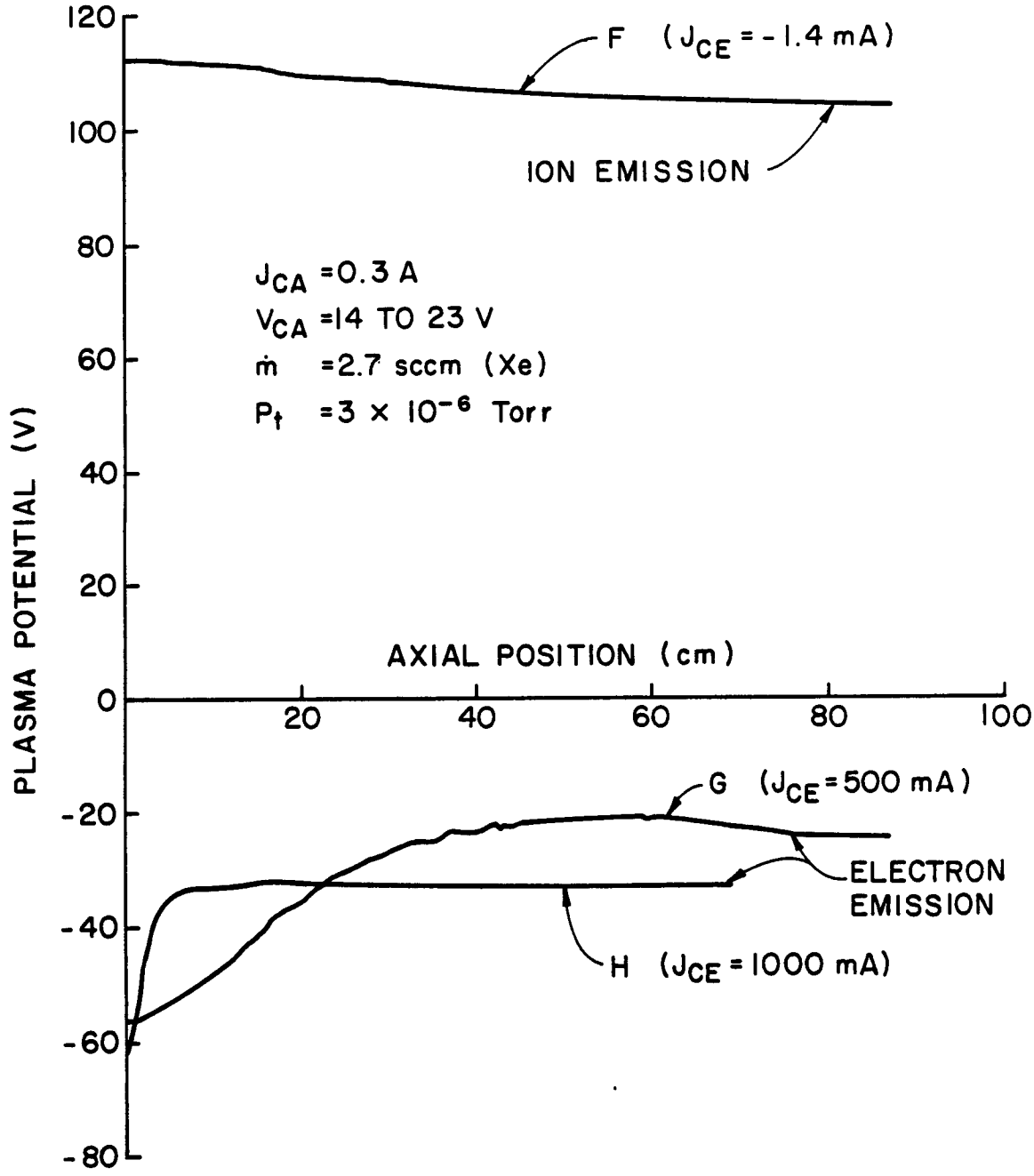

Fig. 31 Typical Plasma Potential Profiles for the 12 cm Dia. Anode Contactor-Simulator off

When several potential profiles sweeps are made with the emissive probe at various radii from the contactor centerline a potential contour map like the one shown in Fig. 32 can be constructed. These data, obtained with the 12 cm dia anode contactor operating in the ignited electron collection mode, are typical and show that the double sheaths suggested by Curves A, B and presumably C of Fig. 30 are really relatively spherical in shape. It is noted that in the case of the Fig. 32 data the contactor cathode was 133 V positive of tank potential and the contactor anode was 156 V positive of that potential. This resulted in an electron collection current of 175 mA. These contours again suggest that the potential is relatively uniform in the region very close to the cathode (i.e. the high density plume region) and that it then drops relatively rapidly from about 140 V down to 50 V. At 50 V a potential well develops about 17 cm downstream of the contactor anode beyond which the potential rises and and then levels off at a value between 50 and 60 V. Data not included in Fig. 32 indicate that the potential remained approximately constant from the outermost contour line to a plane 1 m downstream of the contactor. The fact that the contours take on a somewhat hemispherical shape suggests that electrons are flowing nearly radially inward and ions are flowing nearly radially outward from the high density plasma located within the 140 V contour. It should be noted that electrons could also be flowing to the upstream surface of the anode shown in Fig. 32 so the electron collection process could also be occurring over a full spherical surface.

Since the typical sheath contours of Fig. 32 are essentially spherical and the potential difference across the sheath can be measured using the emissive probe the experimentally measured data can be compared to the predictions of the simple spherical double sheath model mentioned in the introduction to this section and developed fully in Ref. 3 (reproduced in Appendix A). In order to determine the extent to which the model describes the physical

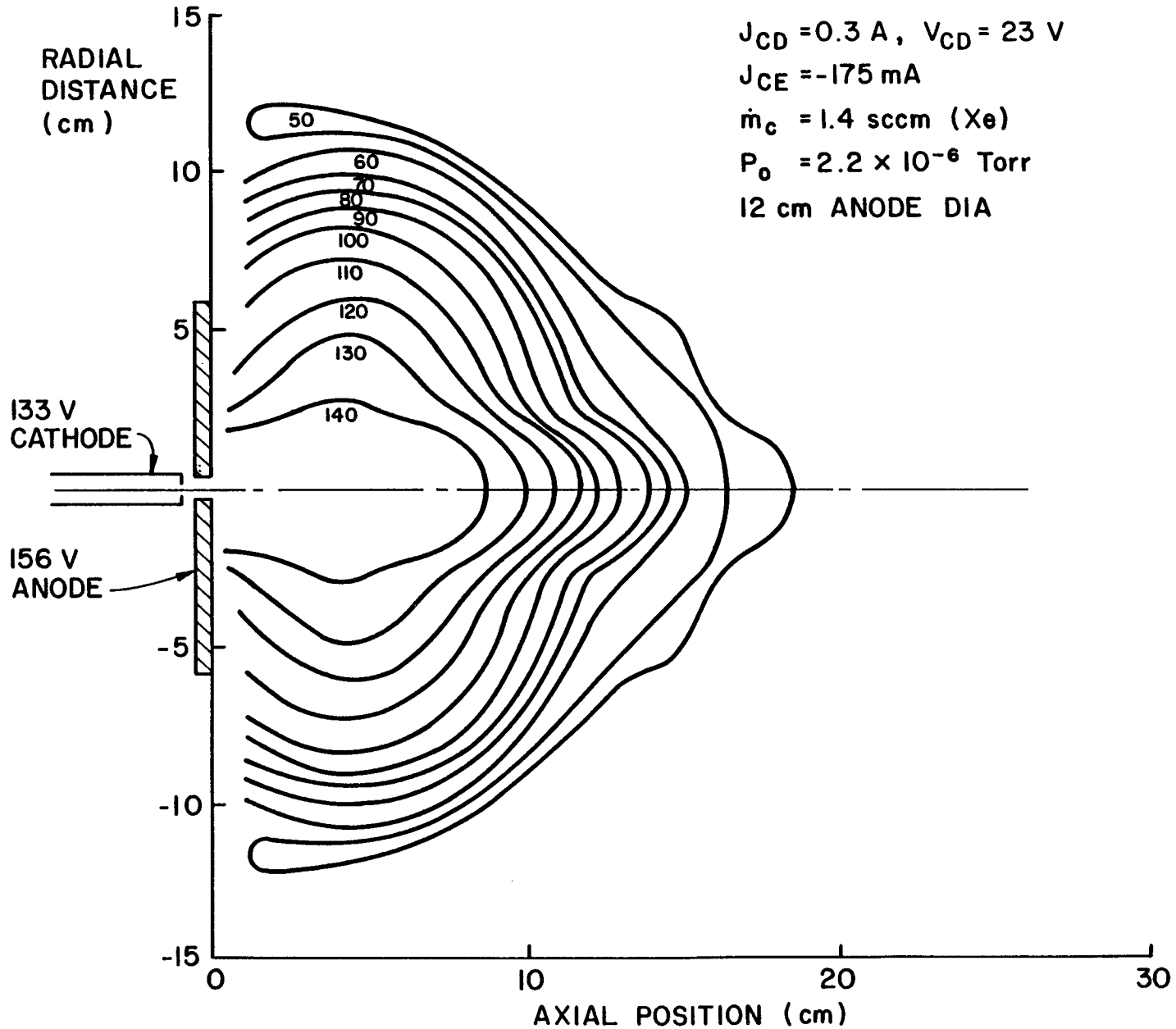

Fig. 32 Typical Potential Contour Map Observed in

behavior of the plasma contacting process as represented by potential profiles like those in Figs. 13 and 30 a number of these profiles were compared to the predictions of the model. The method by which this has been done can be understood by reconsidering Fig. 9a. In order to apply the model, the quantities that must be measured are the experimental voltage drop across the sheath (V_s) in Fig. 9a, and the experimentally determined radii associated with the upstream and downstream boundaries of the double sheath region. In Fig. 9a these are designated r_u and r_d. These points were determined from the experimental profiles by defining the upstream and downstream boundaries as the points of minimum and maximum second derivative of the potential with respect to position respectively. Using the measured potential drop V_s together with the measured electron collection current J_{CE} the normalized current from the outer surface j_o could be computed by substituting $V_i = V_s$ and $J_o = J_{CE}$ into Eq. (1). This value of j_o could then be used to enter Fig. 4 of the paper in Appendix A to determine the theoretical sphere radius ratio r_i/r_o predicted for the collection of the current J_{CE} at a sheath potential drop of magnitude V_s. This theoretically- based radius ratio could then be compared to the measured radius ratio r_u/r_d.

A typical example of the comparison of a measured potential profile with one computed using the equations from Appendix A is shown in Fig. 33. In this case, the electron current from the outer sphere $J_{CE} = J_o$ was 250 mA. The potential drop across the double sheath, $V_s = V_i$ was 103 - 48 = 55 V and the normalized electron current from the outer sphere $j_o = 8.96$ was computed using Eq. 1. From Fig. 4 in Appendix A this value of j_o corresponds to a theoretically based radius ratio (r_i/r_o) of 0.73. The experimentally determined value of the radius ratio r_u/r_d determined from the solid line profile in Fig. 33 is 7.8/12.8 = 0.61. Hence theory predicts a profile that is steeper than the experimentally measured one as Fig. 33 shows.

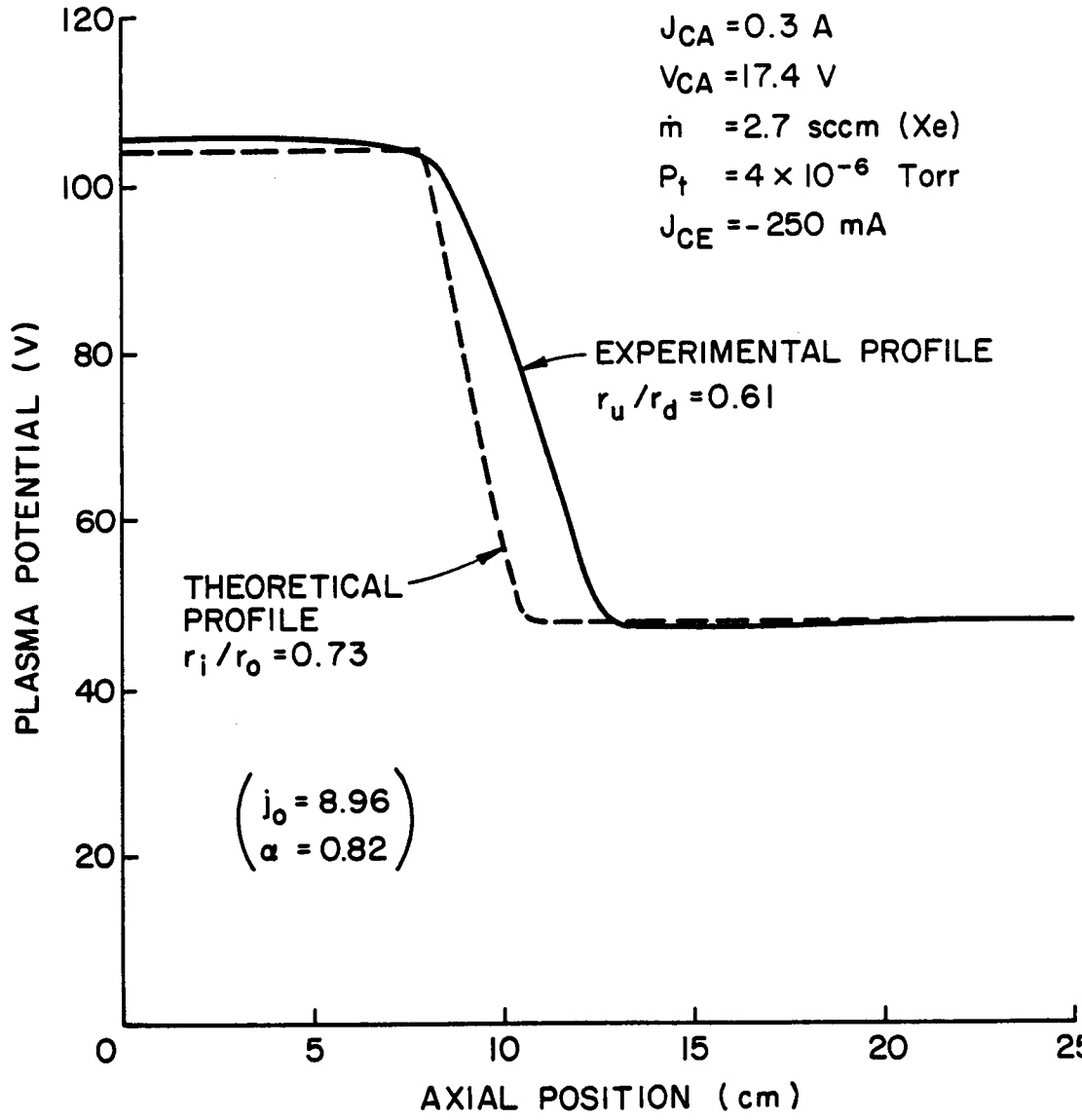

Fig. 33 Typical Comparison of Measured and Predicted Plasma Potential Profiles

Comparison of the experimentally and theoretically-determined radius ratios obtained in the described manner over a wide range of operating conditions is presented in Fig. 34. In obtaining these data the anode diameter of the contactor was varied from 1 to 12 cm, the hollow cathode discharge power was varied from zero to 17 W, the xenon flowrate was varied from 1.2 to 6.8 sccm and this also resulted in tank pressure variations from 2 to 10 x 10^{-6} Torr. The extent to which the theoretical model describes the physical results is reflected in the proximity of the data points shown to the solid, perfect fit line of Fig. 34. Examination of the data in this figure suggests that the predicted radius ratios agree with the measured ones to within about 25% and the predicted ratios are systematically greater than the measured ones. It is noted that points that fall below the -25% error boundary are ones that were obtained either under conditions where significant electron current was being drawn from the tank (approximately 10%) or extra expellant other than that through the hollow cathode orifice was being fed into the vacuum chamber to increase the vacuum tank back pressure. Operation at either of these conditions could be expected to cause the assumptions of the theoretical development to break down because both electron emission from any point other than the outer sphere in the theoretical model and the effects of ionizing collisions in the double sheath have been neglected in model development.

Reconsideration of the potential contour map of Fig. 32 suggests that it might be more appropriate to consider the current flow process to be occurring between hemispherical rather than spherical surfaces. In order to investigate this, the equations developed in Appendix A were redeveloped to yield the current flowing from an outer hemisphere:

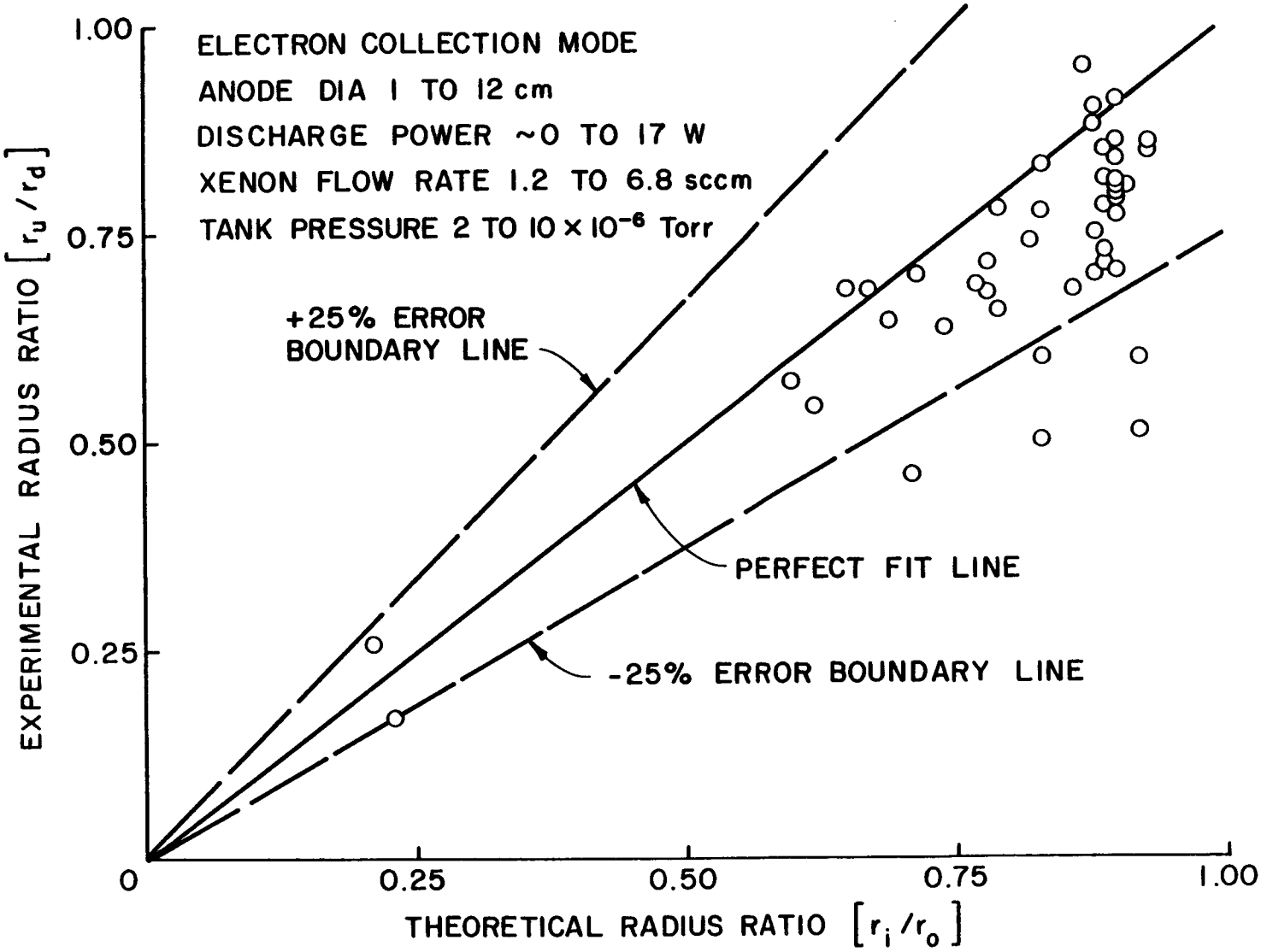

Fig. 34 Radius Ratio Comparison for Spherical

$$J_o = 2\pi\varepsilon_o V_i^{3/2} \sqrt{\frac{2e}{m_o}}\ j_o \qquad (3)$$

Application of this equation in place of Eq. 1 to the same data as that used to obtain the results presented in Fig. 34, yielded the results shown in Fig. 35. Since these data appear to be skewed further from the perfect fit line in the results of Fig. 34, it was concluded that the spherical case represents a better fit to the experimental data than the hemispherical one.

Circuit Considerations at High Electron Collection Currents

In early experiments conducted on plasma contactors during the grant period the electron collection currents were very small compared to the contactor and simulator anode currents (J_{CA} and J_{SA}) identified in Fig. 3. When ignited electron collection operation occurred this was no longer the case. As a result some operational constraints developed which can be best understood by looking at detailed current balances associated with operation at points B and C in Fig. 29. Electron current balance diagrams associated with these two operating conditions are presented in Fig. 36. In the unignited situation (Fig. 36a) 38 mA of electron collection current is picked up at the contactor anode and this combines with 262 mA of electron emission from the contactor cathode to the contactor anode to produce the 300 mA contactor anode current which was being maintained by the anode power supply during the test. At the simulator where the 38 mA electron current collected at the contactor was produced, a 262 mA electron current had to be collected at the simulator anode because a 300 mA electron emission current from the simulator cathode was being maintained by the simulator anode power supply. In this particular case the electron current drawn to the contactor anode from the simulator cathode was small compared to the anode and cathode currents being maintained at the contactor and

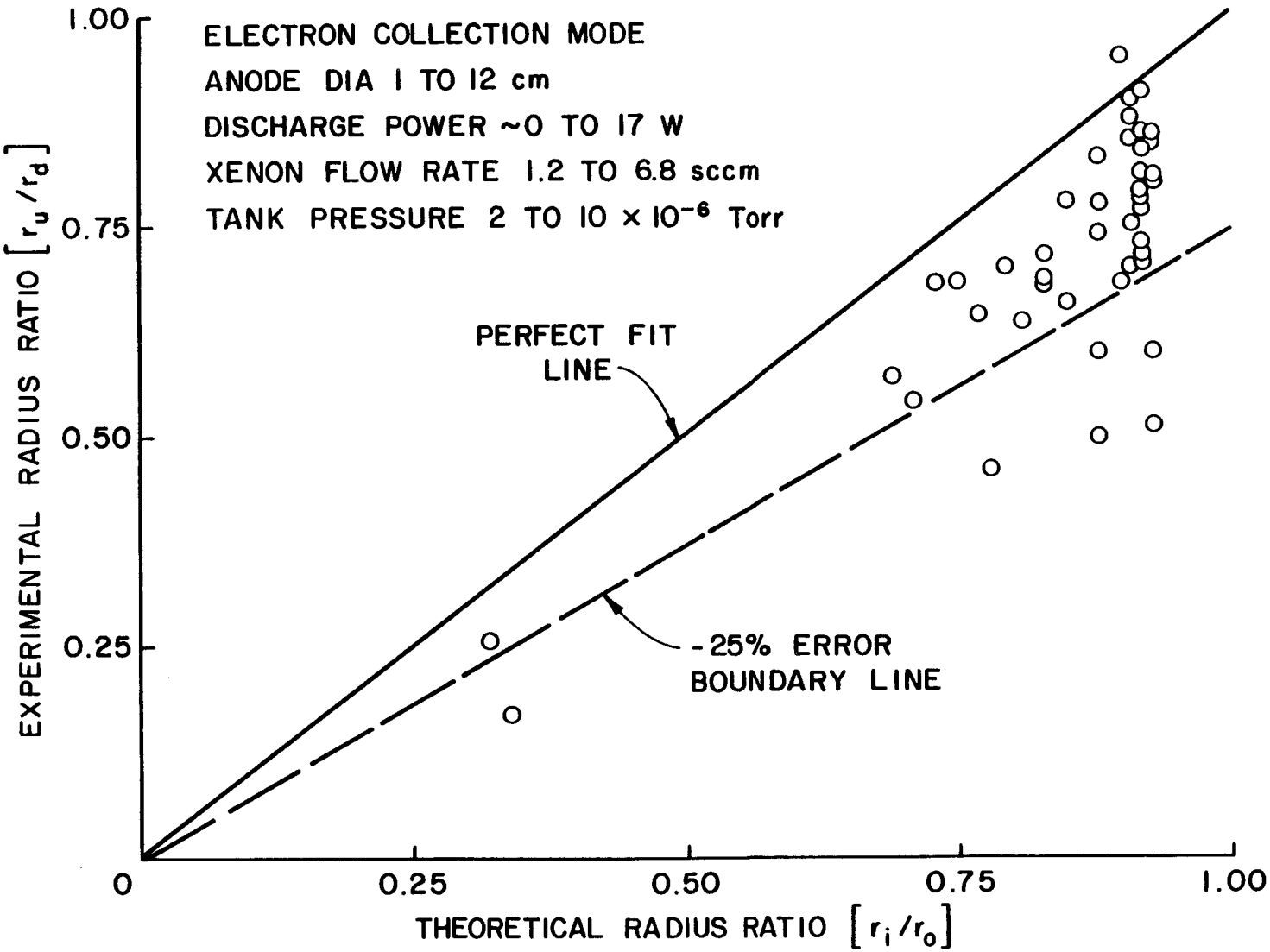

Fig. 35 Radius Ratio Comparison for Hemispherical Double Sheath Model

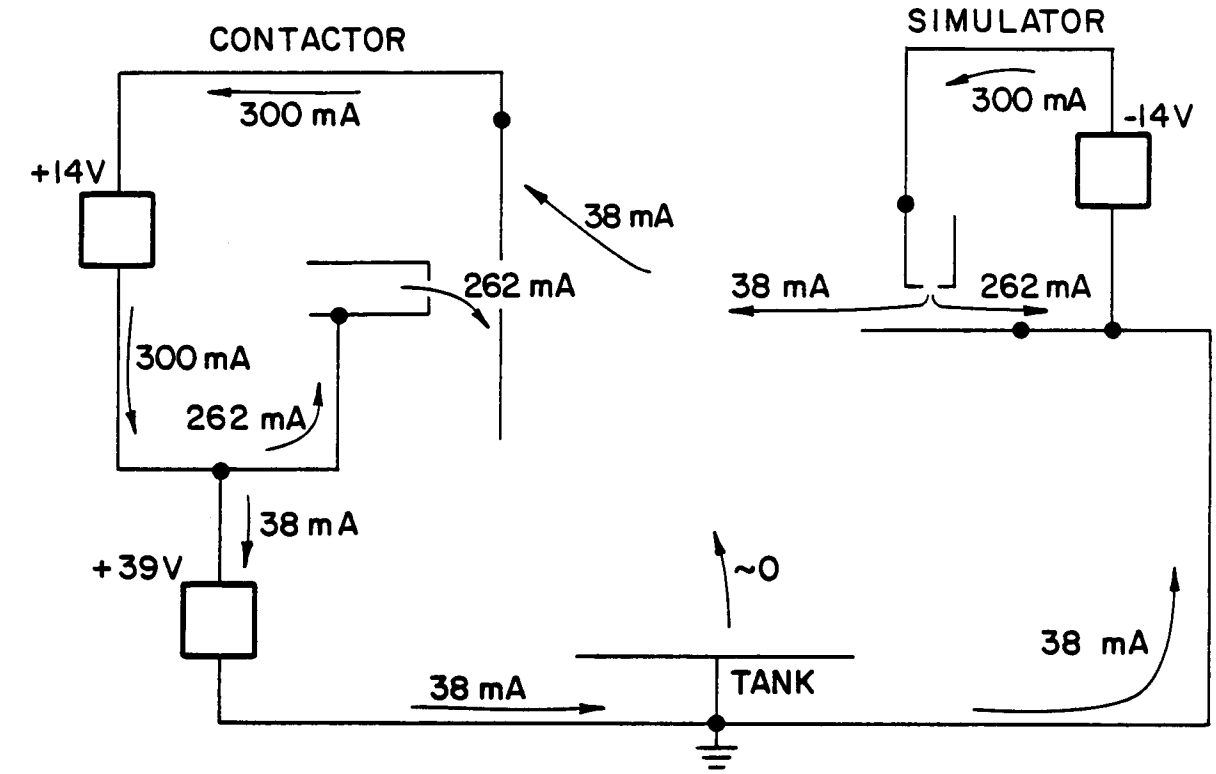

a. CONDITION C (UNIGNITED)

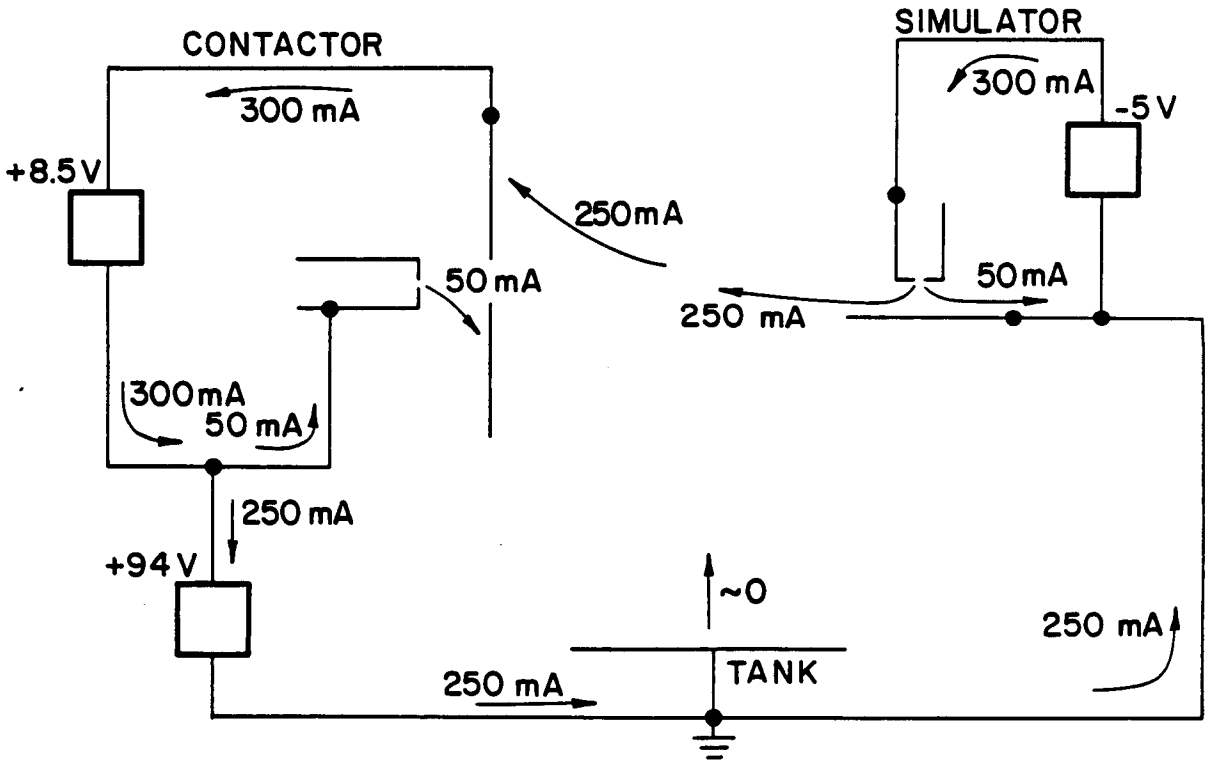

b. CONDITION B (IGNITED)

Fig. 36 Effect of Transition to Ignited Mode Operation on Electron Current Balance

simulator, respectively.

When the contactor underwent transition to the ignited mode, however, the situation changed (Fig. 36b) because a 250 mA electron current was conducted between the simulator and the contactor and this current was comparable to the currents being maintained to the contactor anode and simulator cathode. Under this operating condition a limitation on the contactor anode and simulator cathode currents effectively limited the electron current flowing between the simulator cathode and contactor anode. This effect is illustrated even more dramatically at operating Condition A defined in Fig. 29 which corresponds to the current balance situation of Fig. 37a. In this case limiting the simulator cathode and contactor anode currents results in a limitation on the current that can flow through the plasma to the extent that no current is collected at the simulator anode, 18 mA is drawn from the tank wall, and 30 mA of electrons are collected at the contactor cathode. In order to accommodate this operating condition the simulator anode is actually negative of the simulator cathode and the contactor anode is only 1.5 V positive of the contactor cathode. This situation can be rectified so a prescribed current can continue to flow through the simulator anode/cathode loop if the point of connection between the vacuum tank and the simulator is transferred from the simulator anode to the simulator cathode in the manner suggested in Fig. 37b. When the connection is made in this way, it is possible to sustain the desired simulator anode/cathode loop current (300 mA in this case) while supplying any contactor collection current that may be demanded. Further, the experiment-disturbing electron current drawn from the vacuum tank wall drops to zero as the data of Fig. 37b indicate. In Fig. 37b, however, one notices that the current that can be collected at the contactor is still limited by the contactor anode current which is being held at a specified value (~330 mA). Switching the point of coupling power supply connection from the contactor cathode to the contac-

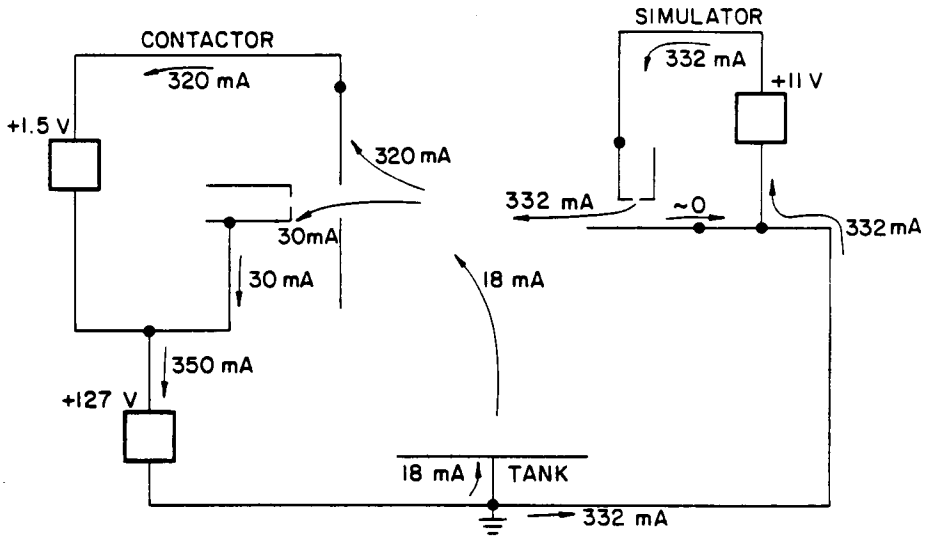

a. GROUNDED SIMULATOR ANODE

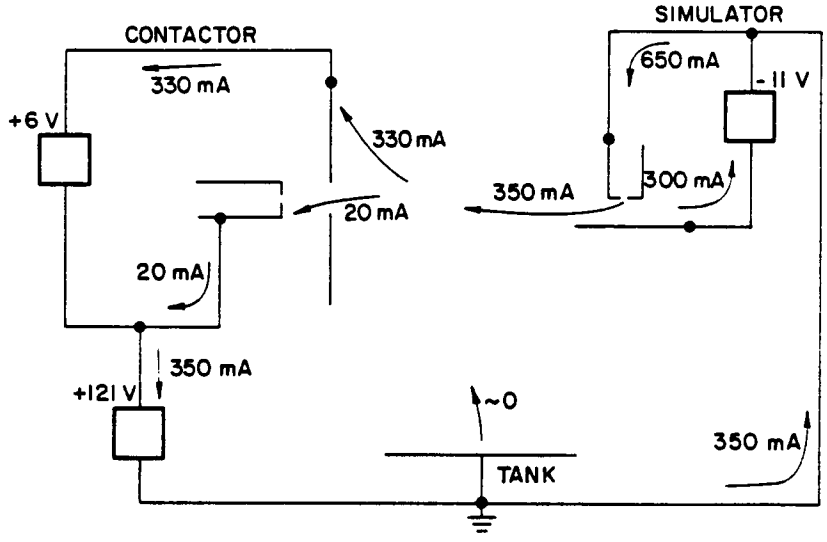

b. GROUNDED SIMULATOR CATHODE

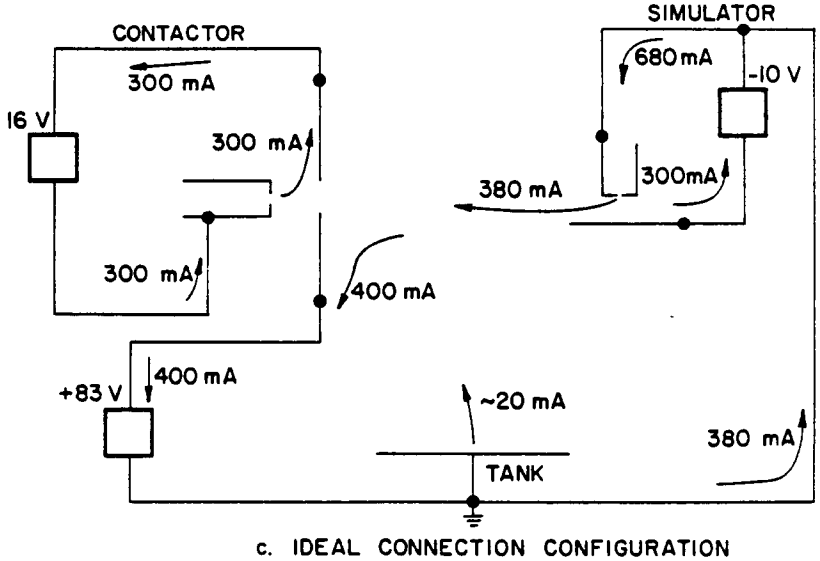

c. IDEAL CONNECTION CONFIGURATION

Fig. 37 Effect of Simulator-to-Tank Connection Point on Electron Collection Current Balance (Condition A)

tor anode alleviates this situation when the contactor is operating in the electron collection mode. By doing this the contactor operating current (i.e. in the loop between the contactor cathode and anode) can be controlled independent of the current collected from the simulated space plasma at the contactor anode. A typical current balance diagram showing the currents and voltages measured with this preferred connection arrangement in presented in Fig. 37c.

When the contactor is being operated in the electron emission mode (condition E in Fig. 29) and the simulator anode is grounded the current balance diagram shown in Fig. 38a is observed. In this case, the system handles any current demanded in the electron emission process while holding the anode current at the contactor and cathode current at the simulator constant. Switching the point of vacuum tank connection from the simulator anode to the simulator cathode results in the electron current balance shown in Fig. 38b. In this case controlling the contactor anode current enhances the electron collection current at the simulator anode to a small extent. However, the bulk of the electron current is being collected on the tank in this mode of operation and as a result having the tank connected to the simulator cathode is not particularly detrimental. In general, however, the results presented in Figs. 36 to 38 indicate the logical fact that electron emission occurs from a cathode and electron collection occurs at an anode. Hence one can conclude that a contactor operating in the electron emission mode should be connected with its cathode to the coupling supply and it would be preferable in this case for the simulator anode to be connected to the tank. In the electron collection mode on the other hand, the coupling supply should be connected to the contactor anode and the tank should be connected to the simulator cathode.

Characterizing Plasma Contactor Performance

Throughout this report contactor potential has been used as the

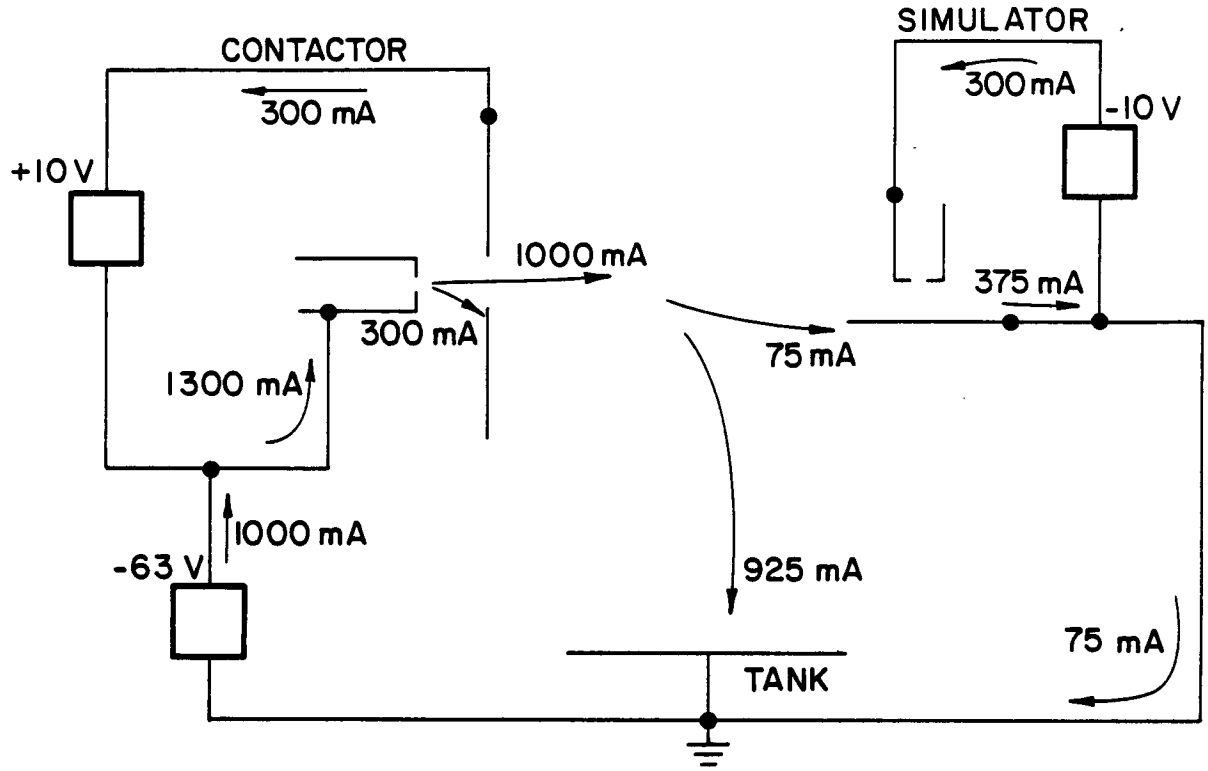

a. GROUNDED SIMULATOR ANODE

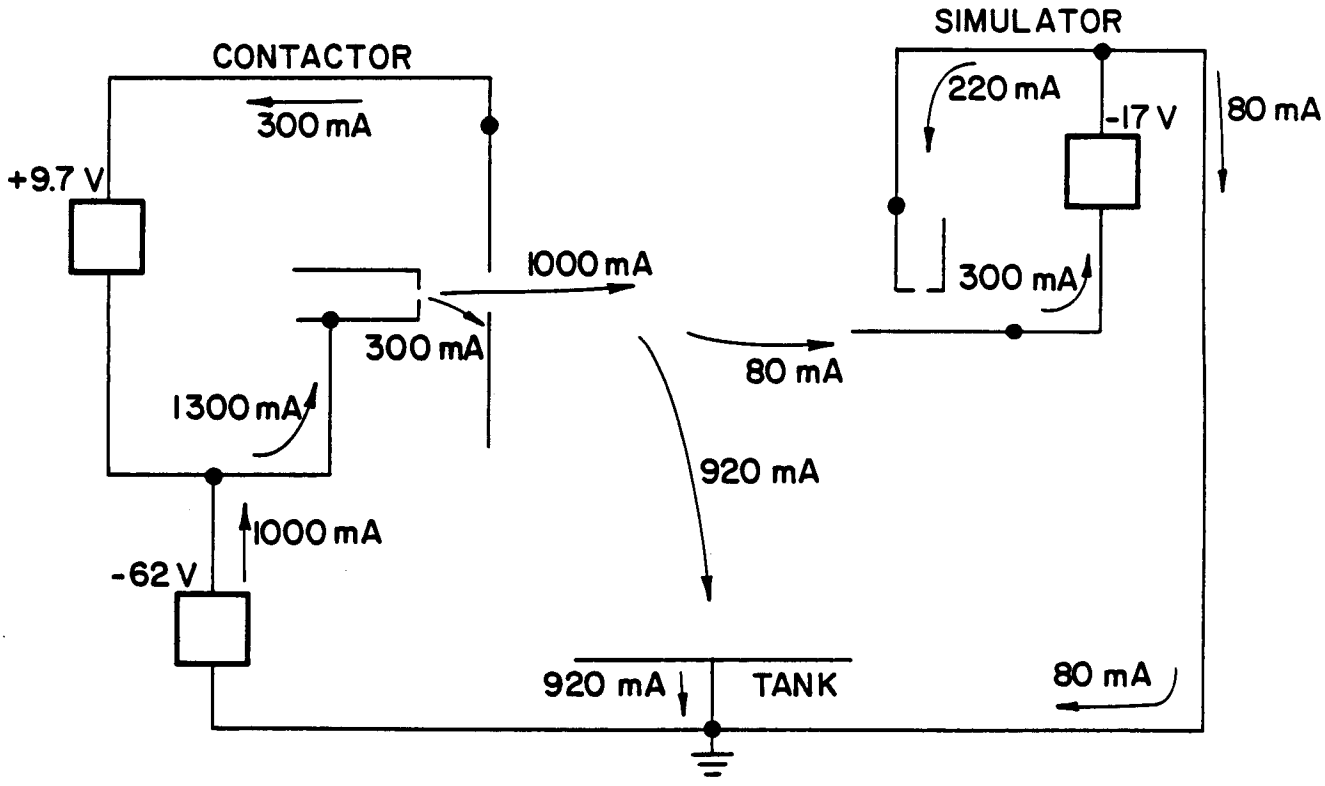

b. GROUNDED SIMULATOR CATHODE

Fig. 38 Effect of Simulator-to-Tank Connection Point on Electron Emission Current Balance (Condition E)

independent variable to characterize contactor performance on plots of electron emission current. Contactor potential has been defined as the potential difference between the anode of the contactor and the anode of the simulator which has also been connected to vacuum tank ground. This potential difference actually represents the potential difference across two contactors, namely the contactor under test and the simulator. It had been hoped that the potential drop associated with the simulator might be small and that the plasma it produced would have a potential relatively near simulator anode potential and it was for this reason that the tank connection was initially made to the simulator anode.

Plasma potential measurements like those shown in Fig. 13, 14, 30 and 31 have implied that a substantial potential drop exists at the simulator and that contactor potential is not a particularly good indicator of contactor performance. By using the emissive probe it is possible to measure the potential difference between the contactor anode and space plasma potential beyond the sheath region (i.e. in the constant potential regions of Figs. 13 and 30 at a location about 1 m downstream of of the sheath). When one does this, a curve like the one shown in Fig. 39 is obtained. This particular curve corresponds exactly to the one represented by the circular symbols in Fig. 29 so comparison of these curves shows the difference obtained when one uses the contactor anode-to-plasma potential difference rather than the contactor potential in plotting a typical contactor performance curve.

Because the data in Fig. 39 were collected using the electrical circuit configuration of Fig. 37b the electron current that could be collected from the simulator-generated plasma was limited to 300 mA because the contactor anode current was limited to 300 mA. When the contactor anode current was increased to 0.9 A, the data of Fig. 40 were obtained. In

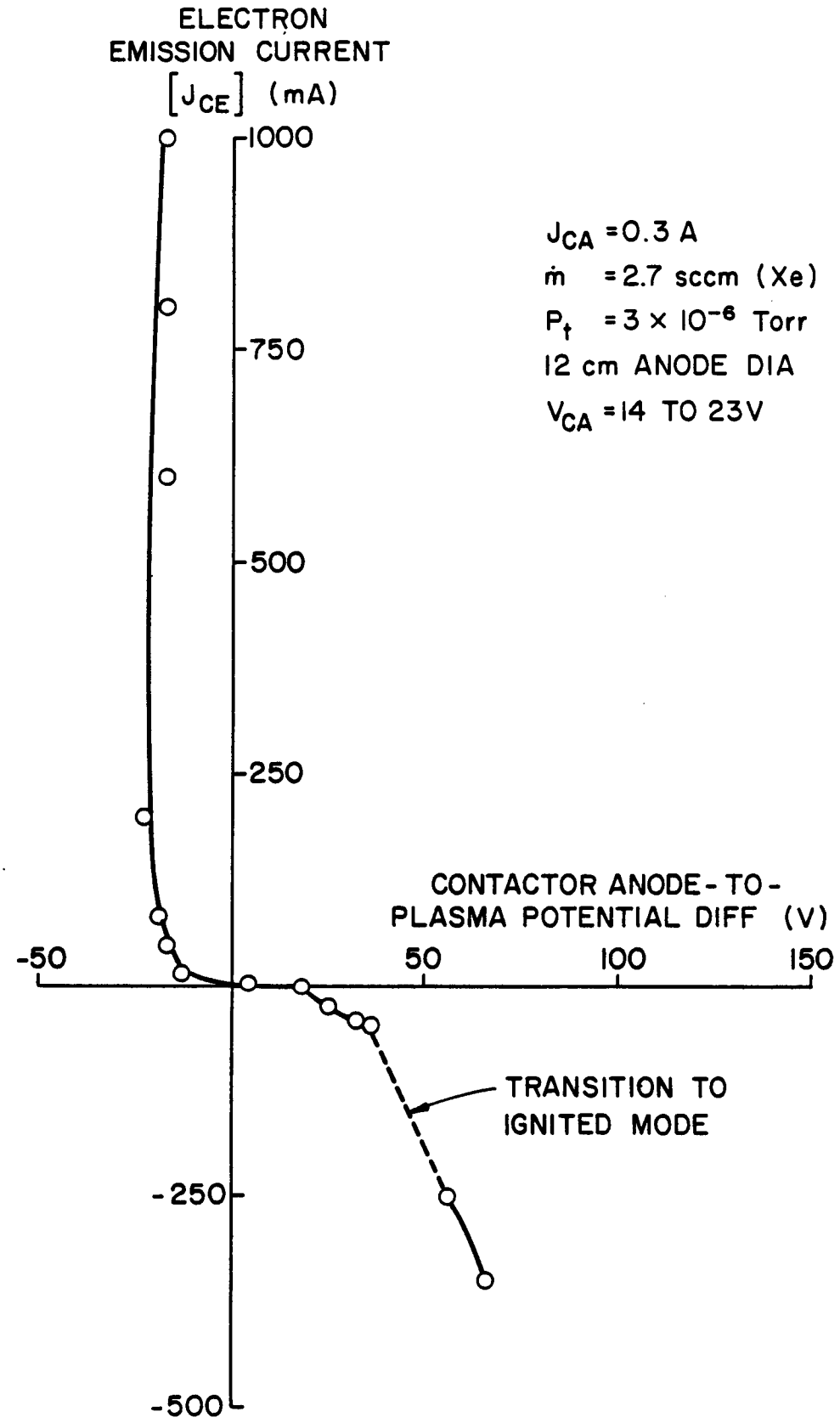

Fig. 39 Contactor Anode-to-Ambient Plasma Potential Difference vs. Emission Current-Low Anode Current Case

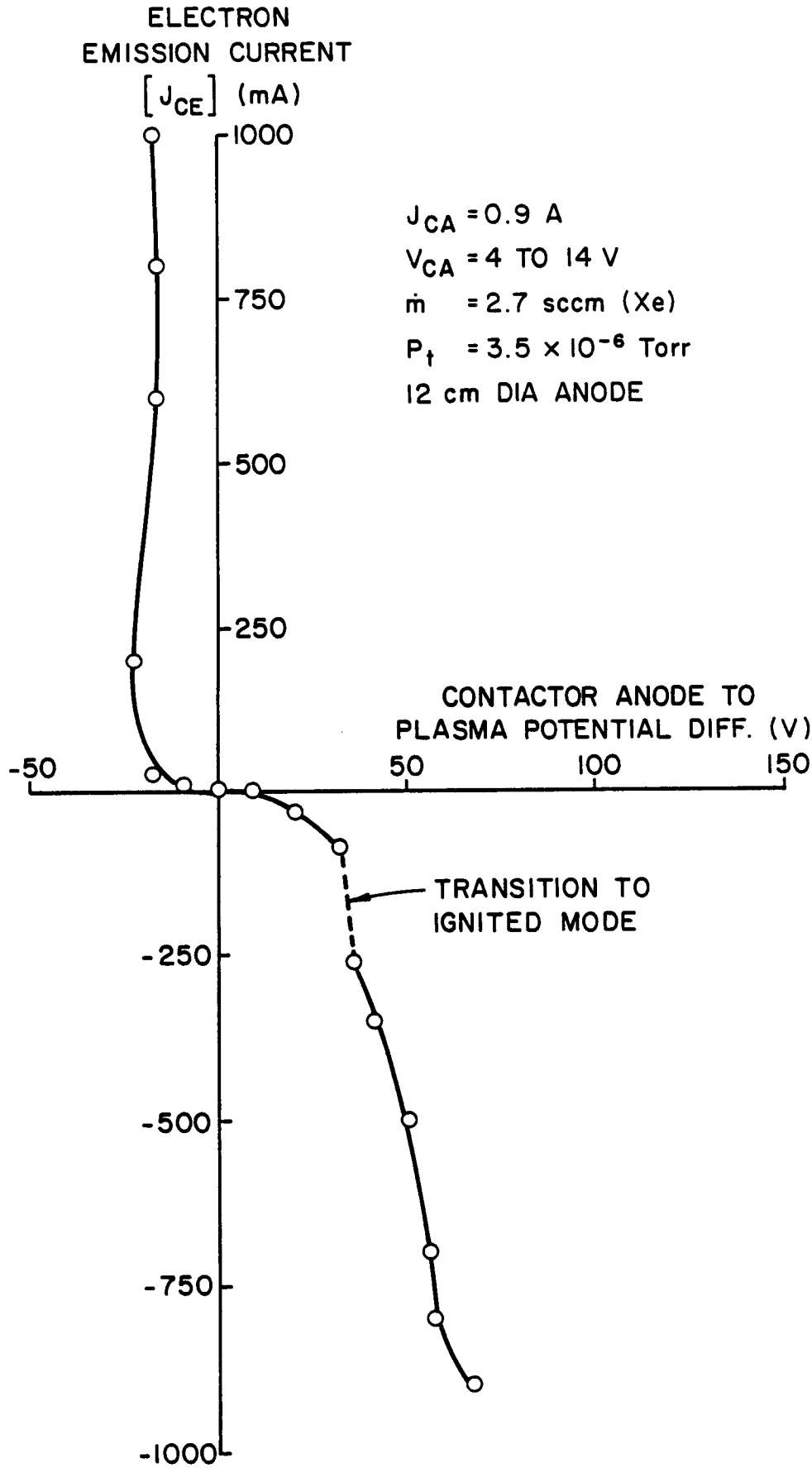

Fig. 40 Contactor Anode-to Ambient Plasma Potential Difference vs. Emission Current-High Anode Current Case

this case it is apparent that the contactor electron collection current can be increased until the higher contactor anode current being maintained (0.9A) is reached. It is also apparent that the curve takes on a shape very much like the ideal contactor curve, i.e. one that is essentially vertical. Finally it is noted that the data of Figs. 39 and 40 were obtained with the simulator and contactor connected in the manner as shown in Fig. 37b. This facilitated electron emission from the simulator at any level demanded while the simulator discharge current was being maintained at 300 mA, however, it was necessary to increase the contactor anode current to 0.9 A in order to achieve the 0.9 A electron collection current. This suggests that it is probably desirable to modify the system circuitry so that either the contactor anode or cathode can be connected to the coupling supply and so the connection can be switched during contactor operation. Future plans call for the simulator cathode to be connected to the tank and the contactor anode connected to the coupling power supply when electrons are being collected by the contactor. When electrons are being emitted from the contactor the contactor cathode will be connected to the coupling supply and the simulator anode will be connected to tank ground.

Electron Current Distribution on the Anode

The variable area anode is instrumented so the current from each segment of anode can be monitored. Hence the current distribution to a 12 cm dia anode can be determined using the apparatus of Fig. 4b with the contactor and simulator connected as shown in Fig. 37b. When this is done at the contactor operating conditions that produced the data of Fig. 40, the current distribution shown in Fig. 41 is measured. In Fig. 41 the vertical distance between the horizontal axis and the solid line containing circular data sym-

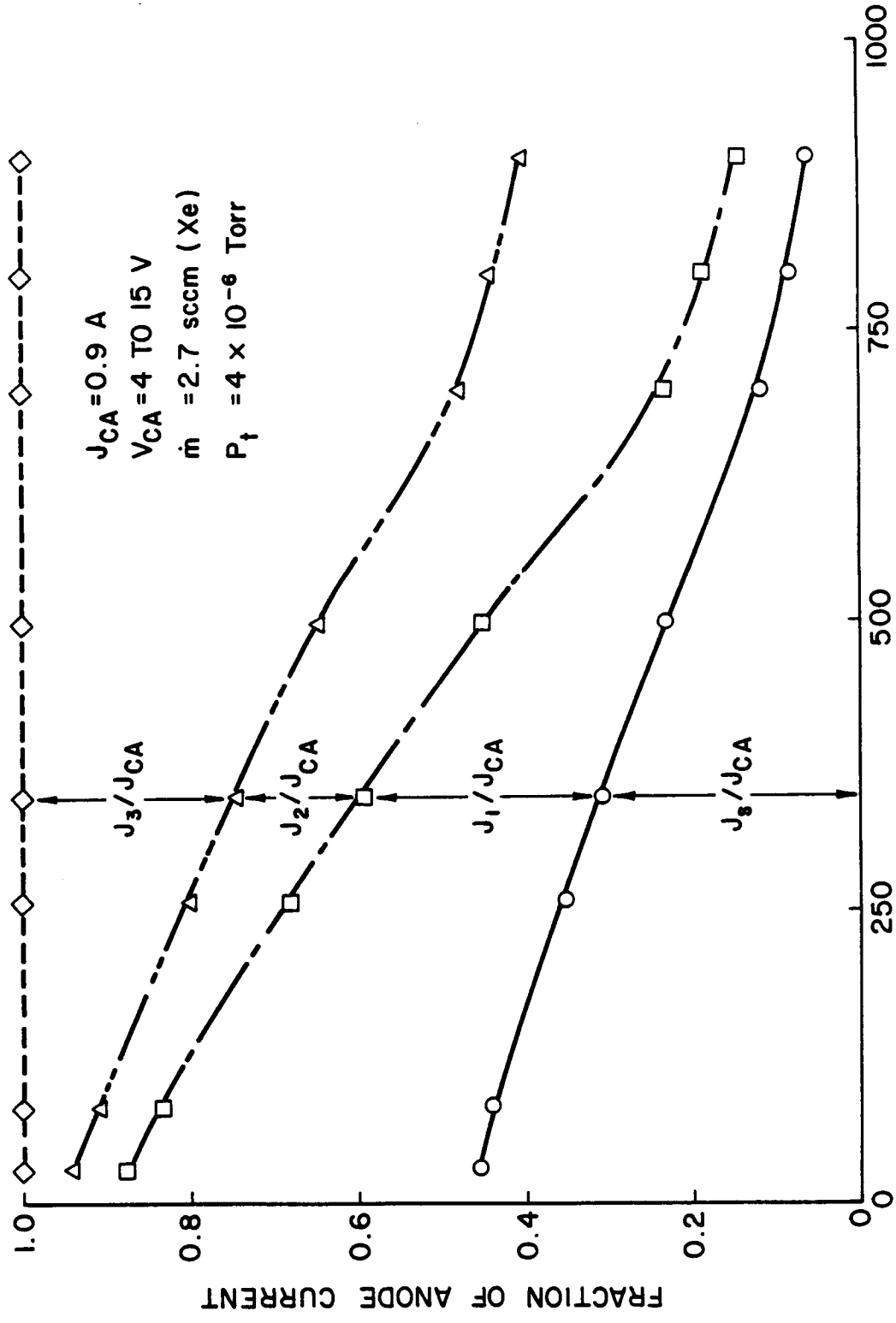

Fig. 41 Anode Current Distribution

bols represents current drawn to the sustaining anode while the vertical separation between the diamond and triangular data symbols represents for example, the current to the outermost anode segment (J_3- see Fig. 7). All currents are normalized using the total contactor anode current and the data are plotted as a function of this total electron current being collected at the anode. It should be recalled in viewing these data that the contactor anode current is limited to 0.9 A, so this is the maximum current that can be collected. The data of Fig. 41 suggest that the sustaining anode and anode 1 (see Fig. 7) collect the bulk of this current when the electron current being collected from the simulated space plasma is small. As the electron collection current is increased, however, less current flows to these anodes and the bulk of the current begins to flow to the anode with the largest surface area (anode 3). This result is particularly interesting when viewed in the light of the equipotential contour map shown in Fig. 32. These data suggest that electrons are drawn radially in toward the cathode and this in turn suggests that they might be drawn preferentially toward anodes S and 1. The fact that the data of Fig. 41 show that the opposite is true indicates that electrons being drawn in through the sheath surrounding the contactor experience substantial scattering probably in the high density plume region. As a result they are able to change their direction from radial trajectories to random ones so they can be collected on the anodes in what appears to be direct proportion to the anode surface areas.

Conclusions

Based on the results collected during this grant period it is concluded that changes in magnetic field in the range from near zero to 0.5 gauss do not induce substantial changes in the characteristic curves that describe plasma

contactors performance. Increasing the contactor anode area facilitates transition into the ignited mode of electron collection. This mode is characterized by substantially lower voltage drops than those observed for contactors collecting electrons at a given current in the unignited mode. Double sheaths appear to develop in both the electron emission and collection modes of operation but they are generally difficult to probe at high currents in the electron emission mode because sheath boundaries are located close to the contactor. In the electron collection mode a structure develops which includes a high density constant potential plasma region immediately adjacent to the contactor, a double sheath region and a low density plasma region from which electrons are collected. A simple model of the double sheath region yields radius ratios associated with the inner and outer boundaries of the region that agree with measured radius ratios to within about 25%.

At the high electron collection currents associated with the ignited mode of operation it is preferable to connect the simulator cathode to the vacuum tank and the contactor anode to the coupling power supply that is used to bias the contactor relative to the simulator in order to induce current flow. When the contactor is operating in the electron emission mode its cathode should be connected to the tank. Hence it is desirable to switch the connection points as operation is switched from the emission to the collection mode of operation. It is believed that it will also be desirable to operate contactors in space so the one emitting electrons has its cathode connected to the tether and the one collecting electrons has its anode connected to the tether.

HIGH PRESSURE HOLLOW CATHODE RESEARCH

Craig Luebben

Arcjet thrusters are attractive because their specific impulse may be close to optimum for many near-earth missions. These thrusters typically use a solid thoriated tungsten cathode that is prone to overheat during operation and melt at the small spot on its tip where electron emission occurs. Thus, these cathodes may not be suitable for long term space applications. The orificed hollow cathode used in ion thrusters emits electrons from a relatively large surface area on its cylindrical insert so it is not as prone to overheating. But hollow cathodes typically operate at interelectrode pressures (i.e. between the anode and cathode exterior) of 10^{-3} Torr, whereas arcjet thrusters operate at pressures of 1000 Torr or greater. The major objective of this research effort has been to develop a hollow cathode that operates satisfactorily on ammonia at high pressures and to identify the factors that facilitate this high pressure operation. Ammonia has been selected for the study because it is an attractive propellant for many arcjet propulsion missions. The approach used in the study has been to increase the operating pressure range gradually from the low values where hollow cathodes operate satisfactorily and their characteristics are known and understood to the high pressures where arcjets operate. When conditions limiting the extent to which pressure could be increased have been encountered, the reason for the limitation has been investigated and the test apparatus and/or procedure has been modified in an effort to overcome the limitation and understand the physical reason for its occurrence.

Apparatus and Procedure

A conceptual diagram illustrating the features of the apparatus used in

this study is shown in Fig. 42. This apparatus is located within a vacuum bell jar in such a way that the interelectrode pressure can be controlled over a pressure range from ~10^{-2} to 10^{3} Torr. The principal elements of this test apparatus are the hollow cathode and the anode. The hollow cathode, which had been fabricated initially in the conventional way using a tantalum tube body electron beam welded to a thoriated tungsten orifice plate was replaced by cathodes fabricated from insulating materials. This allowed the insert, which is located within the cathode body, to be electrically isolated from the cathode body and the orifice plate. Various orifice plate materials were tested, including boron nitride, tantalum and graphite. The typical insert was a cylinder with a diameter of a few millimeters made by rolling several layers of 0.013 mm thick tantalum foil treated with the low work function Chemical R-500*. This type of insert has been used because a previous study[9] showed that this insert, which is easy to fabricate, performs as well in short term tests as other more costly inserts. The anode used in the tests had a diameter that ranged from 2 cm to 5 cm and was made of tantalum when it was radiation cooled and of copper when it was water cooled.

All tests were conducted using ammonia as the working fluid (expellant) and the valving arrangement shown in Fig. 42 allowed this fluid to be directed in two different flow patterns. Normal flow, which is used in ion thruster hollow cathodes, involves flow through the hollow cathode from the cathode interior region to the interelectrode region and then out of the system through the vacuum pumps. The normal flow configuration is achieved by positioning the valves shown in Fig. 42 in the manner designated in the first row of Table I.

*Chemical R-500 is a double carbonate ($BaCO_3$, $SrCO_3$) mixture that has been manufactured by the J.R. Baker Chemical Co., Phillipsburg, N.J. but is no longer made.

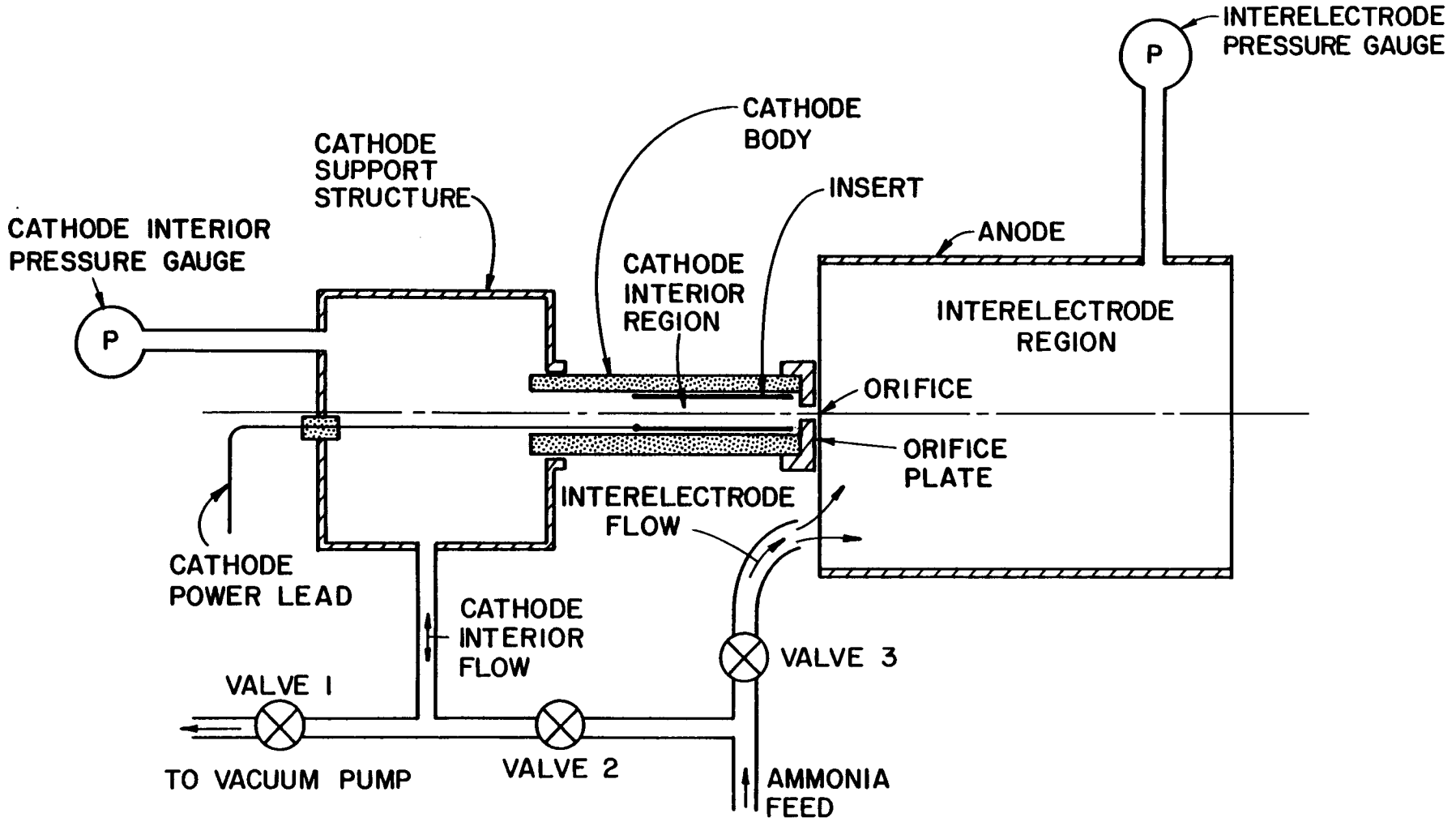

Fig. 42 Hollow Cathode Test Apparatus Schematic

Table I

Expellant Flow Configurations

Pattern Designation	Valve Positions		
	Valve 1	Valve 2	Valve 3
Normal	Closed	Open	Closed
Reverse	Open	Closed	Open

During preliminary testing it was determined that high interior cathode pressures resulted in very small emission spots on the insert which eventually resulted in insert melting and failure.[9] Hence it was determined that the cathode interior pressure should be held low relative to the high interelectrode pressures and the reverse flow pattern was found to be preferable to the normal one. With reverse flow the expellant was fed through the interelectrode region into the cathode interior region through the cathode orifice and then out through the pumping system. This flow pattern was achieved by positioning the valves as shown on row 2 of Table I. It should be noted that while a vacuum pump had to be connected to the cathode interior region to achieve reverse flow in the laboratory, this could be achieved in space by simply venting the cathode interior to space. The normal flow configuration was generally used, at low interelectrode pressures, to initiate the discharge. Once the discharge had been started and stabilized the flow valves could be repositioned to permit testing in the reverse flow configuration. The pressure gauges shown in Fig. 42 were provided to measure the cathode interior and interelectrode pressures during operation.

The schematic of Fig. 42 shows a horizontal orientation for the apparatus and this orientation was indeed used during the early test period. At high interelectrode pressures, however, heated expellant appeared to rise in this apparatus thereby enhancing the probability of current flow from the cathode orifice to the upper anode surface and possibly perturbing the test results. In order to minimize these effects the apparatus of Fig. 43 was built. This apparatus has two features that help to prevent the expellant buoyancy problem just mentioned, namely a vertical orientation of the cathode axis and vortex inducing tubes suggested by Hardy[10] to facilitate the formation of a swirling flow in the interelectrode region. The apparatus in Fig. 43, however, includes the same basic features identified in the discussion of Fig. 42. The vortex inducing tubes shown in Fig. 43 are located approximately 2 mm above the face of the orifice plate, and the ammonia injection ports into the interelectrode region have a diameter of 0.1 mm and an inclination of 45^{o} relative to tne tangent to the anode. The anode itself is a 2 cm dia copper tube which has copper cooling coils silver soldered to its exterior surface. The water, which circulates through these coils, is supplied through polyflo tubing which serves to isolate the anode electrically from the water source. This circulating water cools the cathode indirectly by conducting heat from it to the anode through the boron nitride cathode body. The entire apparatus shown in Fig. 43 is enclosed within a vacuum bell jar. Flow through the vortex inducing tubes therefore increases the interelectrode region pressure and escapes through the cathode orifice and through anode structure joints into the bell jar.

The apparatus suggested in Figs. 42 and 43 is designed to have a great deal of flexibility so changes, introduced to overcome the problems encountered during operation at ever increasing interelectrode pressures, can be made. A summary of the hollow cathode design and operational parameters that

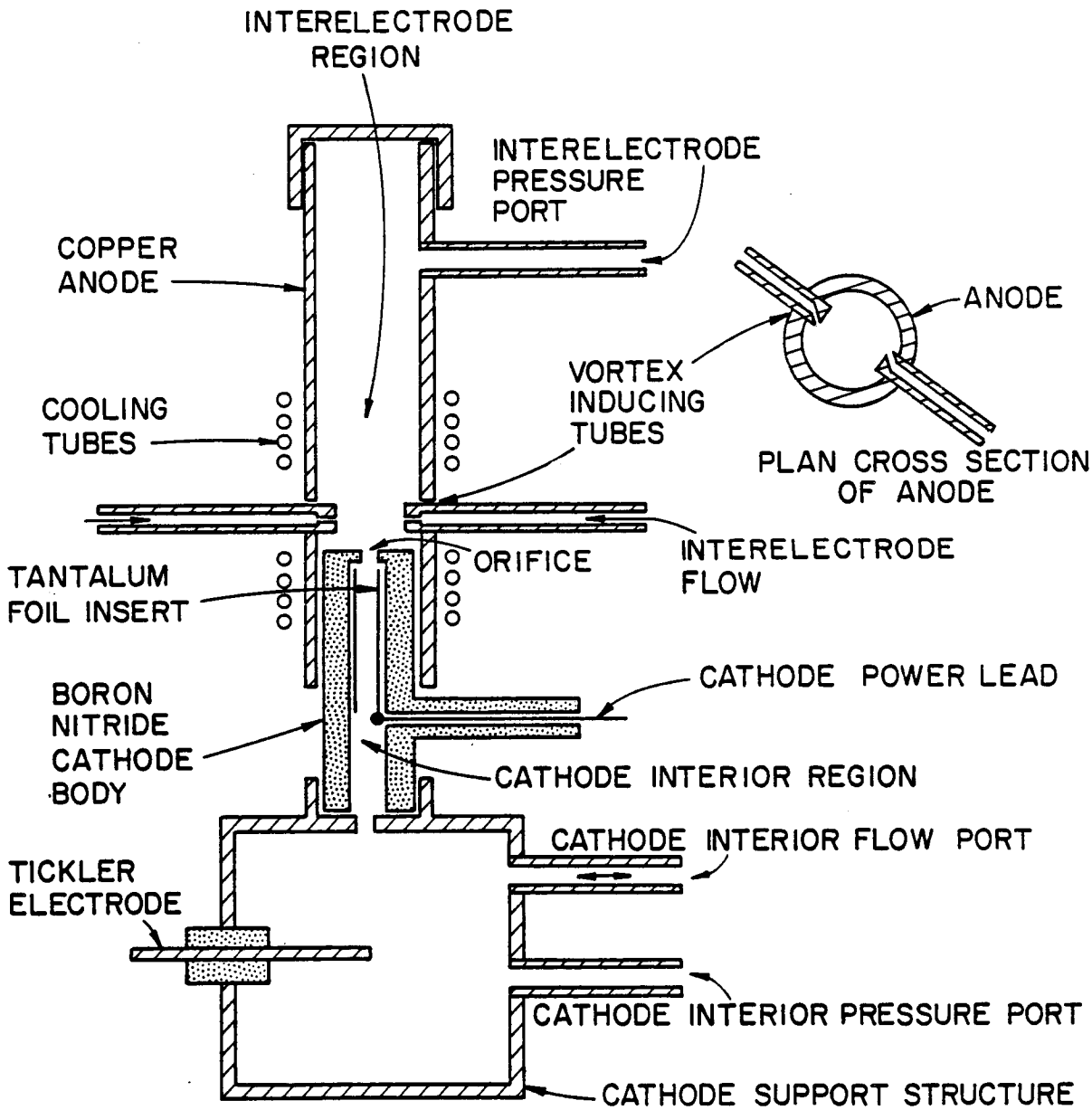

Fig. 43 Vertically Oriented Test Apparatus

were varied in the study is presented in Table II. Many of these parameters are self-explanatory, however, some explanation of the cathode configurations associated with the various orifice plates is needed. Boron nitride orifice plates were made by simply machining round stock to produce the cathode body and orifice configuration suggested by Fig. 43.

Table II

Parameters Varied in Hollow Cathode Study

Parameter	Changes introduced
Cathode tube material	. boron nitride . tantalum w/quartz insulator
Cathode orifice diameter	. open-ended (5.0 mm) . 0.25 to 1.8 mm
Cathode orifice region material	. boron nitride . tungsten . graphite
Orifice region configuration	. plate, orifice on centerline . cylindrical cap, orifice on center . semi-conical cap, orifice on center . semi-conical cap, offset orifice
Anode/cathode cooling	. radiation cooled . water-cooled
Expellant flow	. normal flow . reverse flow
Discharge current	. 4 A to 14 A
Cathode/anode axis orientation-anode dia.	. horizontal-5 cm dia. . vertical (with vortex flow stabilization)-2 cm dia.

When this orifice plate was replaced by a tungsten one, a cavity was machined in the boron nitride body and the tungsten orifice plate was cemented in place using ceramic adhesive as suggested in Fig. 44. In this apparatus the insert

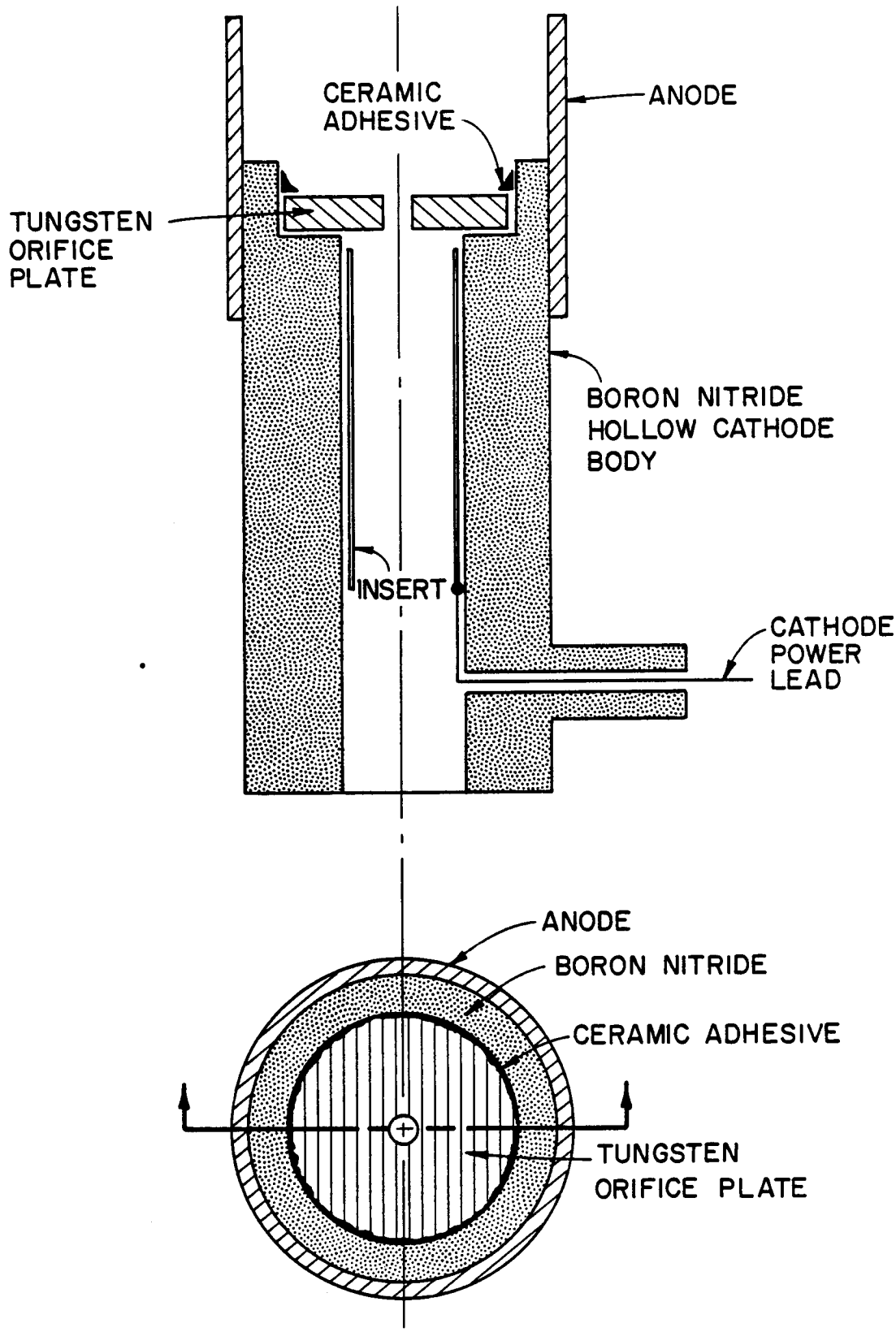

Fig. 44 Boron Nitride Body/Tungsten Orifice Plate Hollow Cathode

was displaced upstream of the orifice plate by a few millimeters so it would remain isolated electrically from the plate. Graphite orifice caps with various configurations were also used. They were installed in the manner suggested in Fig. 45 so the insert and the graphite orifice cap remained isolated from each other. The graphite caps were relatively easy to machine so a variety of them having the shapes and orifice hole positions indicated in Fig. 45b were investigated.

Experiments conducted during the previous grant period[9] had shown the necessity of keeping the insert isolated from the orifice plate to prevent emission from occurring at the orifice plate at high interelectrode pressures. Installation of the tantalum cathode body configuration of Fig. 46 therefore necessitated provision for insulation between the insert and the tantalum tube. This was accomplished by installing a quartz tube between them as suggested in Fig. 46. It was hoped that the quartz tube would facilitate radiation from the hot insert to the cathode body, so thermal conduction from the insert to the quartz tube would be small, anode water-cooling coils would remove heat through the boron nitride cathode body at a sufficiently rapid rate and the quartz tube would not melt.

In order to conduct a test, ammonia was fed in the normal flow configuration at a sufficiently high rate to produce a cathode interior pressure of approximately 10 Torr and the anode was biased to about 400 V. Frequently this condition was sufficient to result in electrical breakdown initiating a discharge between the cathode and anode. However, on some occasions breakdowns occurred at locations away from the anode and cathode and the tickler electrode shown in Fig. 43 was therefore installed to facilitate startup. In order to use this electrode the anode was kept initially at a potential near

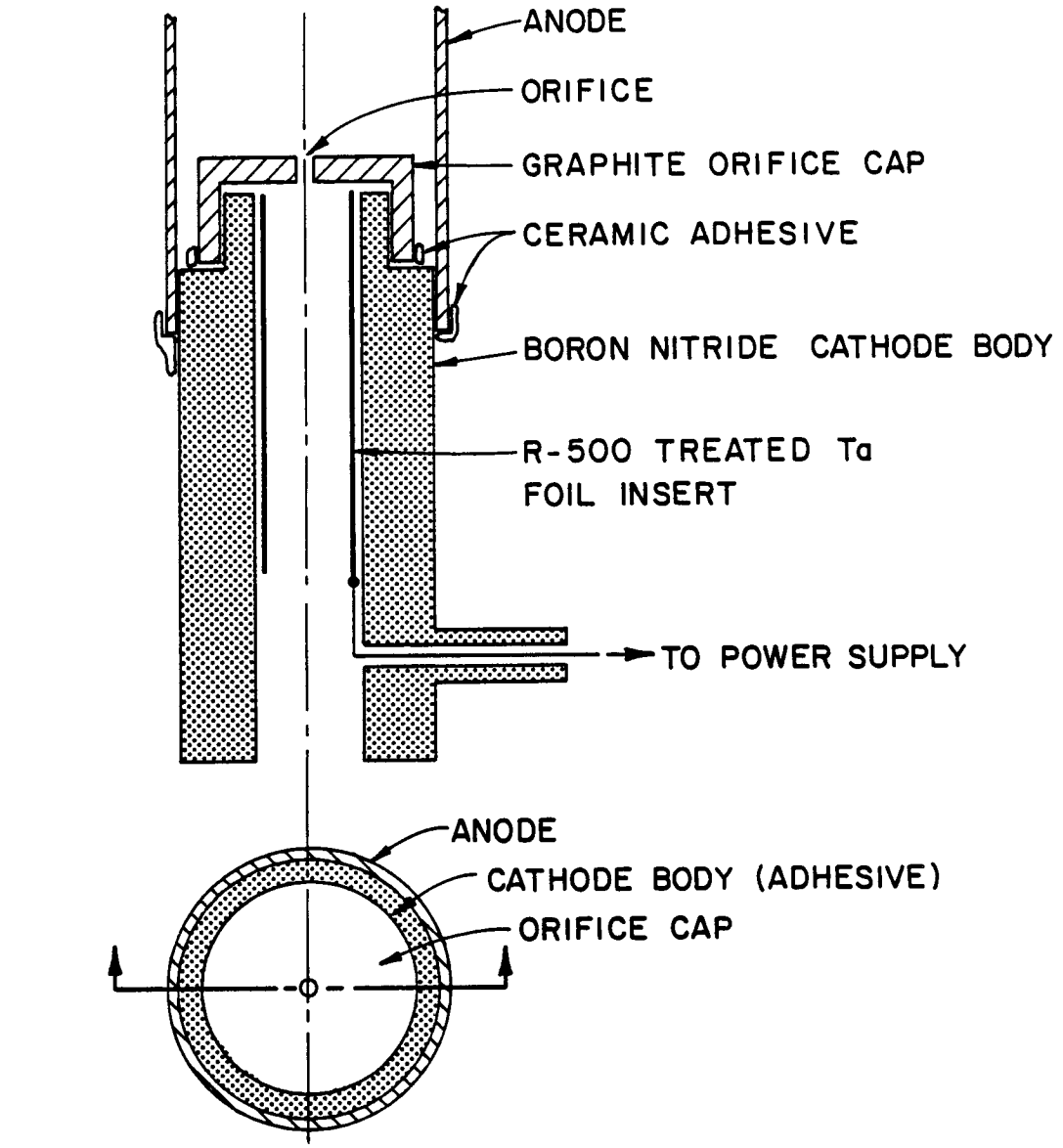

a. GRAPHITE ORIFICE CAP CONFIGURATION (WITH CYLINDRICAL CAP HAVING ORIFICE ON CENTER)

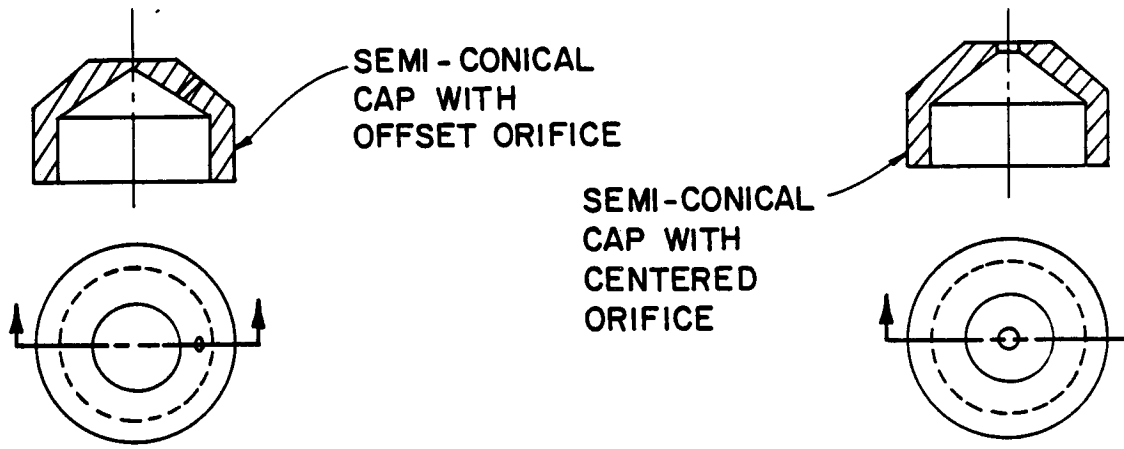

b. ALTERNATIVE CAPS

Fig. 45 Graphite Orifice Cap Hollow Cathode

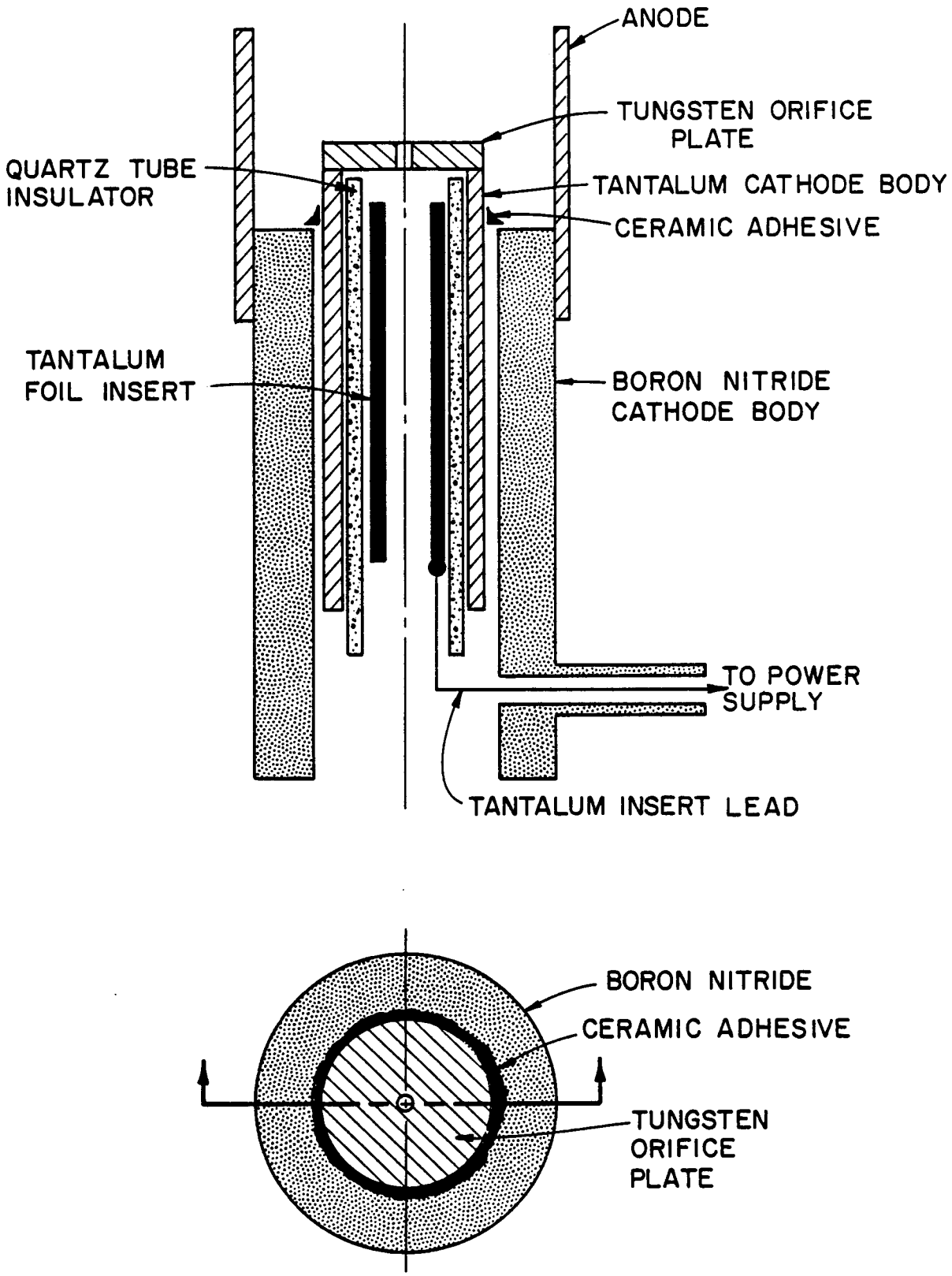

Fig. 46 Hollow Cathode with Quartz Tube Insulation

tnat of the cathode insert and a potential of about 500 V was applied between the tickler and the insert. This typically caused an electron current of approximately 4 to 5 mA to flow. The plasma produced by this low current discharge generally supplied sufficient electrons so that biasing the main anode to a few hundred volts positive of the insert resulted in a discharge between tne anode and the cathode insert. Once the main discharge had established itself in the current range between 4 and 14 A the tickler discharge was shut down. After the discharge had stabilized for several minutes, Valve 3 (Fig. 42) was opened to allow expellant to flow through the vortex inducing tubes. Valve 1 was then opened and Valve 2 was closed to facilitate transfer to the reverse flow configuration. Once operation had stabilized in the reverse flow configuration the ammonia flow into the interelectrode region could be increased to increase the interelectrode pressure. Typically the test then proceeded as the interelectrode pressure was increased in steps while the discharge current was held constant and anode voltage and interelectrode and cathode interior pressures were recorded. While it was also possible to throttle the flow through Valve 1 early tests showed that the cathode interior pressure should be kept as low as possible to prevent damage to the insert. As a result Valve 1 was generally kept at its full open position.

The insert lead shown connecting the insert to the power supply in Figs. 44 through 46 is an 0.8 mm thick by 4 mm wide tantalum ribbon. This lead has a sufficiently large cross-sectional area so the voltage drop along its length remains small at the maximum current levels expected in the experiment. As a result it does not overheat.

Results

Previously reported data have shown some important characteristics of conventional hollow cathode discharges that develop as interelectrode pressure is increased.[9] Of primary importance is the fact that interior cathode pressure increases and as a result the area of the electron emission spot on the insert decreases with increasing interelectrode pressure. Not only has this been observed experimentally on a number of occasions, but it is consistent with the model developed by Siegfried.[11] Such decreases in spot size can lead to insert failure due to localized overheating. It has also been observed that increases in interelectrode pressure cause a discharge localization between adjacent points on the cathode and anode which eventually develops into a very fine spoke or filament of current between these points. This is an undesirable current structure for arcjet applications because it would result in relatively poor heating of the arcjet propellant. The occurrence of these phenomena result in two effects illustrated by the data of Fig. 47 and the associated visual observation of the discharge. First, the anode voltage tends to increase as interelectrode pressure is increased. Second, the site of electron emission tends to occur from a small spot on the cathode nearest the anode, even if there is a lower work function site on the cathode somewhat further from the anode. In the case of the data of Fig. 47, this emission spot migration occurred near interelectrode pressures of 10 Torr.

Typical data showing the voltage drop distribution between the cathode and the anode are presented in Fig. 48. These data were obtained using an emissive probe like the one described in Ref. 9 together with a hollow cathode having a boron nitride body that was open ended (no orifice plate) and a 5 cm dia tantalum anode. These data are relatively typical and have been seen with many

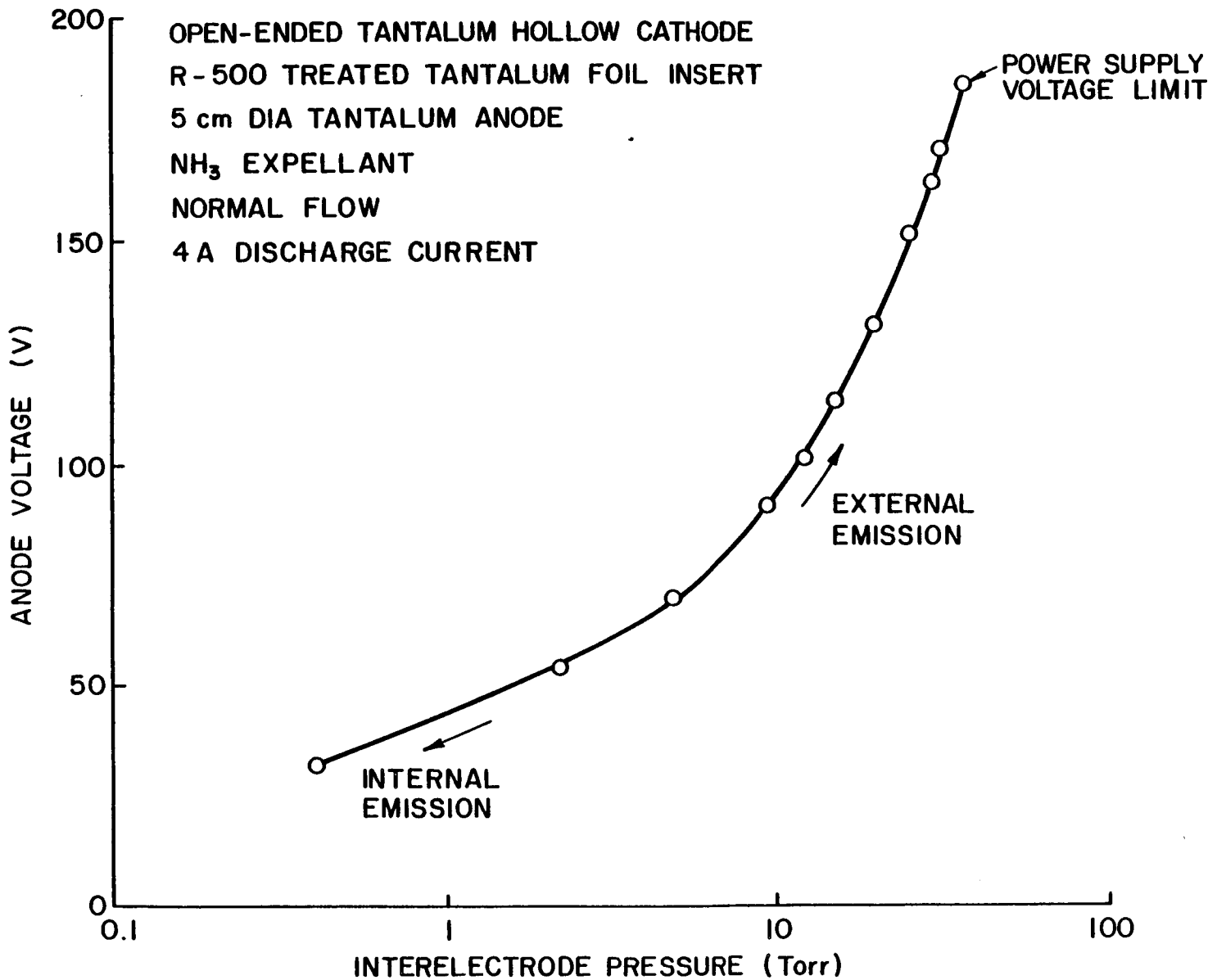
OPEN-ENDED TANTALUM HOLLOW CATHODE
R-500 TREATED TANTALUM FOIL INSERT
5 cm DIA TANTALUM ANODE
NH_3 EXPELLANT
NORMAL FLOW
4 A DISCHARGE CURRENT
POWER SUPPLY VOLTAGE LIMIT
EXTERNAL EMISSION
INTERNAL EMISSION
ANODE VOLTAGE (V)
200
150
100
50
0
0.1
1
10
100
INTERELECTRODE PRESSURE (Torr)

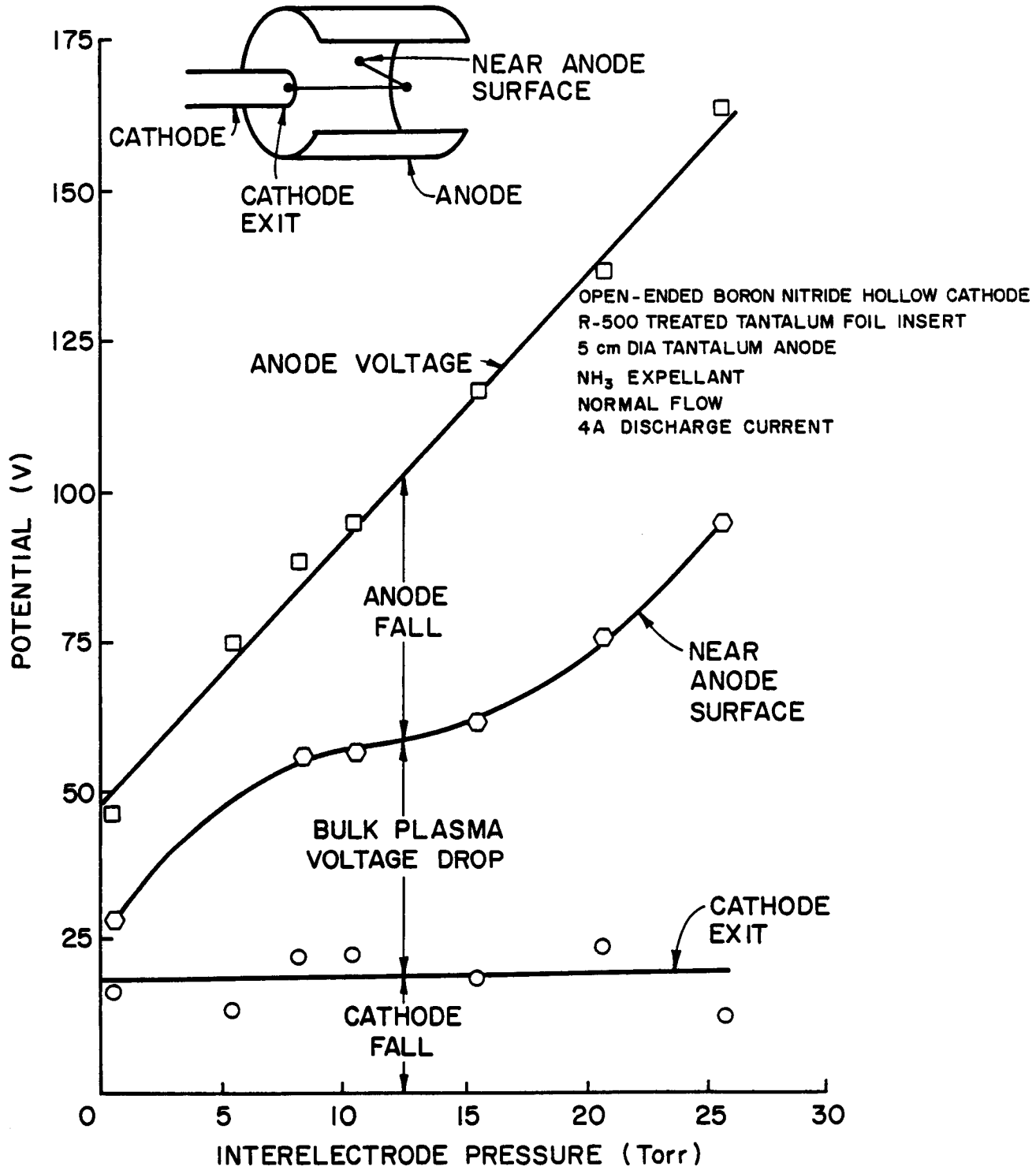

Fig. 48 Typical Plasma Potential Profile

C-2

different anode and cathode configurations. They show that the cathode fall, i.e. the voltage drop between the cathode and the point in the plasma immediately adjacent to it, remains relatively constant as interelectrode pressure increases. The voltage drop through the voltage plasma and at the anode, however, increases with interelectrode pressure. It should be noted that it is preferable for the bulk plasma voltage drop to dominate the total voltage drop because it is the bulk plasma voltage drop that determines the power going into propellant heating in an arcjet application. The cathode and anode fall voltages on tne other hand are proportional to the power going into heating the cathode and anode.

The capacity of a hollow cathode to sustain lower cathode interior pressures at prescribed interelectrode pressures by using reverse rather than normal flow is demonstrated by the data of Fig. 49. For example, at an interelectrode pressure of 50 Torr, a 4 A discharge current and a 0.51 mm dia orifice the data of Fig. 49 show the interior pressure in the reverse flow case is 13 Torr compared with 50 Torr for normal flow. These date were obtained using a cathode body and orifice plate made of boron nitride. In both the normal and reverse flow situations, operation had to be terminated because the orifice enlarged due to what appeared to be melting. In fact, the nonlinearity of the reverse flow data above about 60 Torr suggests that in the reverse flow case, the orifice may have begun to enlarge at an interelectrode pressure near 60 Torr. Had orifice enlargement not occurred it is believed tne cathode interior pressure would have only been about 20 Torr at an interelectrode pressure of 90 Torr rather than 30 Torr as the data show. Above 90 Torr in the reverse flow case dramatic enlargement of the boron nitride cathode orifice occurred, the cathode interior pressure increased rapidly and the test had to be stopped. Note from the data of Fig. 49,

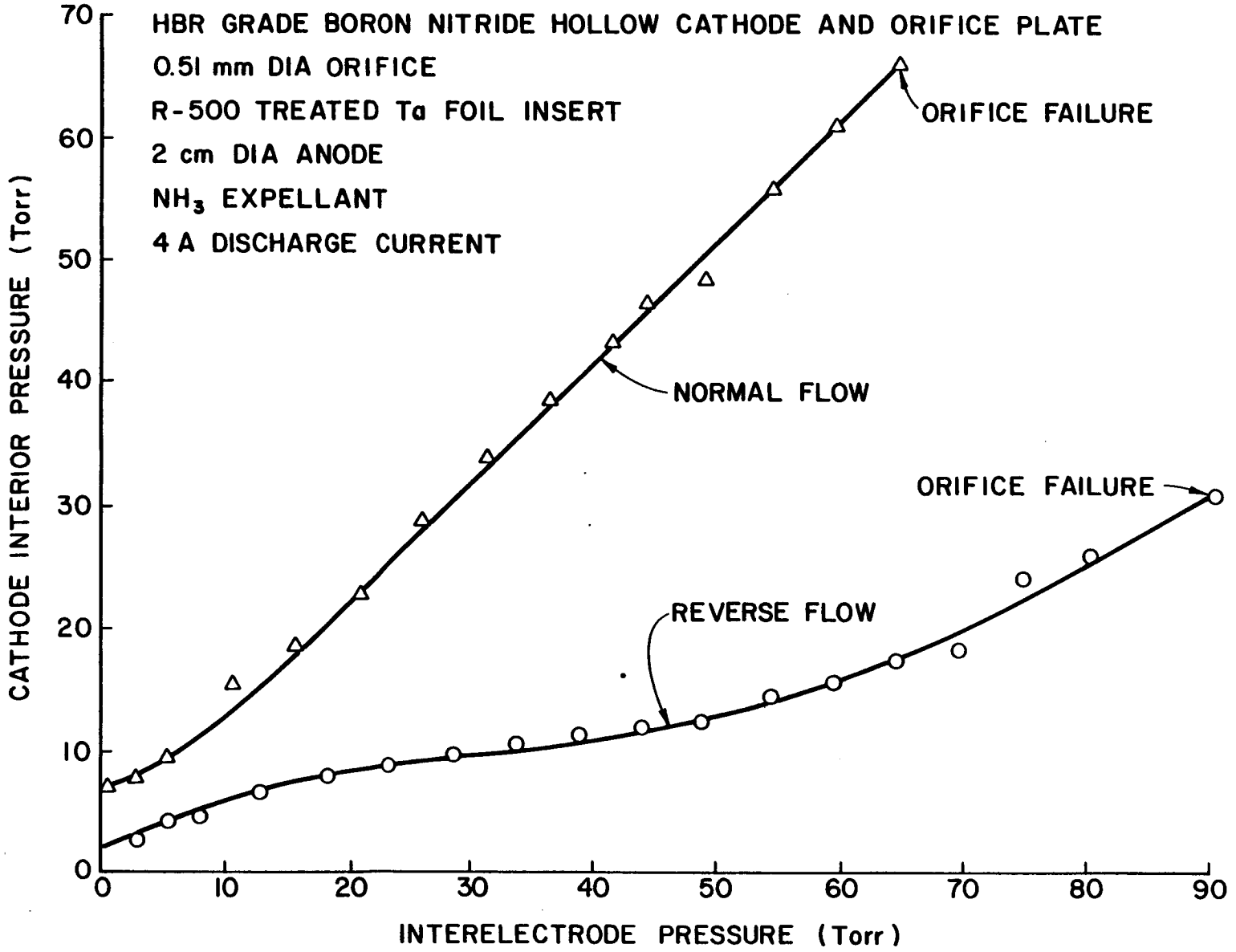

Fig. 49 Effect of Flow Direction on Cathode Interior Pressure

however, that higher interelectrode pressures were realized before orifice failure with reverse flow than with normal flow (90 Torr for reverse flow versus 65 Torr for normal flow).

An objective of the study was to achieve operation on ammonia at interelectrode pressure approaching 1,000 Torr. Both analytical and experimental results obtained suggest that the cathode interior pressure should be around 10 Torr or less to sustain a diffuse emission from the cathode insert. In order to estimate of the orifice size required to achieve this, the data of Fig. 50 were collected while ammonia was flowing through the cathode orifice in the reverse direction but no discharge was occurring. While it was recognized that the actual relationship between interior and interelectrode pressures would be a function of discharge current, these data did provide an indication that the orifice diameter would have to be less than ~0.5 mm to realize a sufficiently low cathode interior pressures to assure diffuse emission from the insert. These data were also used to estimate whether a cathode orifice was enlarging during a test by simply comparing the interior and interelectrode pressures; this was generally done by turning off the discharge and making a comparison. Tests conducted with various orifice sizes at a 4 A discharge current suggested that a change in cathode orifice diameter affected the cathode interior pressure but did not influence its interelectrode pressure vs. anode voltage characteristic. This result, shown by the data of Fig. 51, indicates essentially the same anode voltage versus interelectrode pressure plot for orifice diameters ranging from 0.5 to 1.8 mm. For all of the tests conducted with the boron nitride cathode orifice plates, the orifice plate tended to fail because of orifice enlargement due to what appeared to be melting. In one attempt to overcome this problem, copper cooling coils were cemented to the boron nitride but they did not facilitate

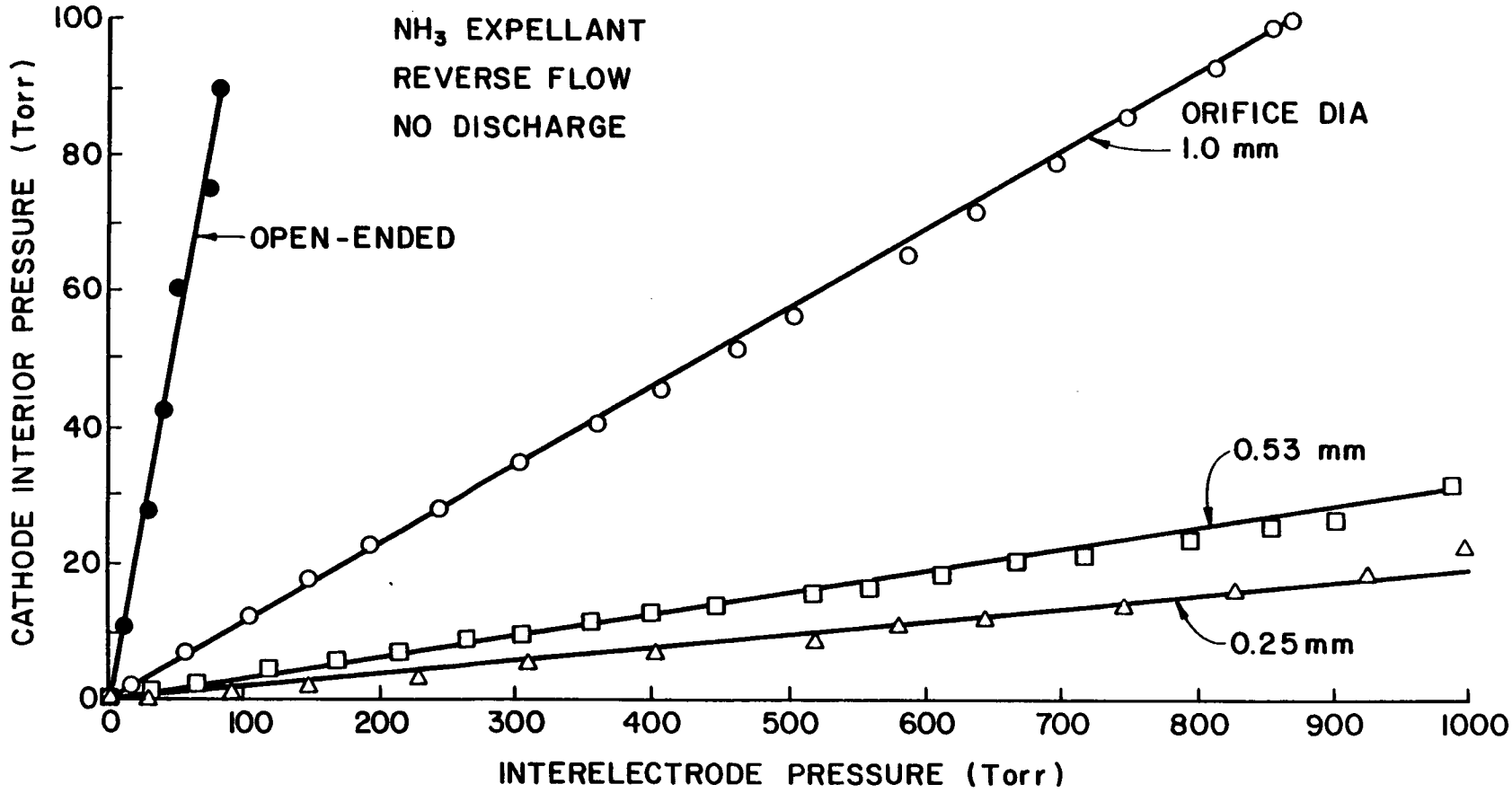

Fig. 50 Effect of Orifice Diameter on Pressure Distribution for no Discharge Case

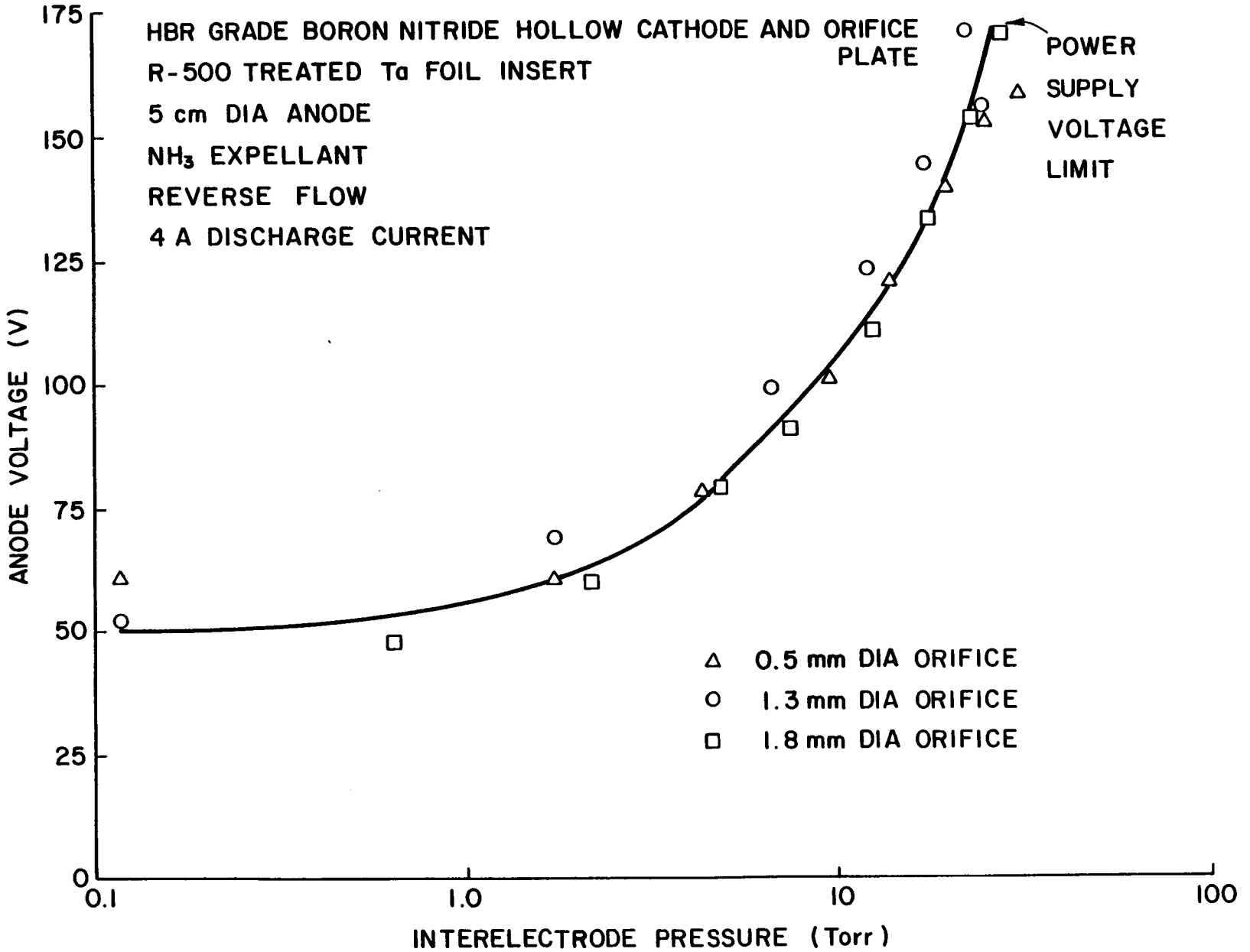

Fig. 51 Effect of Orifice Diameter on

operation without melting at higher pressures.

The data presented in Figs. 48 through 51 were all collected using the horizontal orientation of the cathode axis and a cathode body and orifice plate made of HBR grade boron nitride. It was postulated that the experiments might be extended to higher pressures if the melting temperature of the boron nitride orifice plate could be increased and if flow changes could be introduced to encourage an electron current path along the centerline of the cathode at the orifice. In order to accomplish this, the vertically oriented test apparatus utilizing vortex stabilized flow, shown in Fig. 43, was used. In addition, the boron nitride grade was improved from the 1200°C melting point HBR grade to the 2000°C melting temperature HBC grade. These changes were insufficient to prevent boron nitride orifice plate melting, although they did facilitate some increase in the interelectrode pressure that could be sustained before orifice plate failure occurred.

Using the apparatus of Fig. 43 it was possible to demonstrate that increases in discharge current facilitated a larger pressure drop across the cathode orifice in the reverse flow configuration. Typical data demonstrating this are presented in Fig. 52 where the changes in interelectrode pressure are plotted as a function of discharge current for a cathode with a relatively large (0.94 mm dia) orifice in which expellant flows were controlled so cathode interior pressure remained constant. The data of Fig. 52 were actually obtained by increasing the discharge current while a fixed expellant flow rate through the vortex tubes and a fixed pumping environment on the cathode interior were maintained. Anode voltage decreased slightly as current was increased through the range indicated. Increasing the expellant flow induced increases in both inter-electrode and cathode interior pressures and produced the

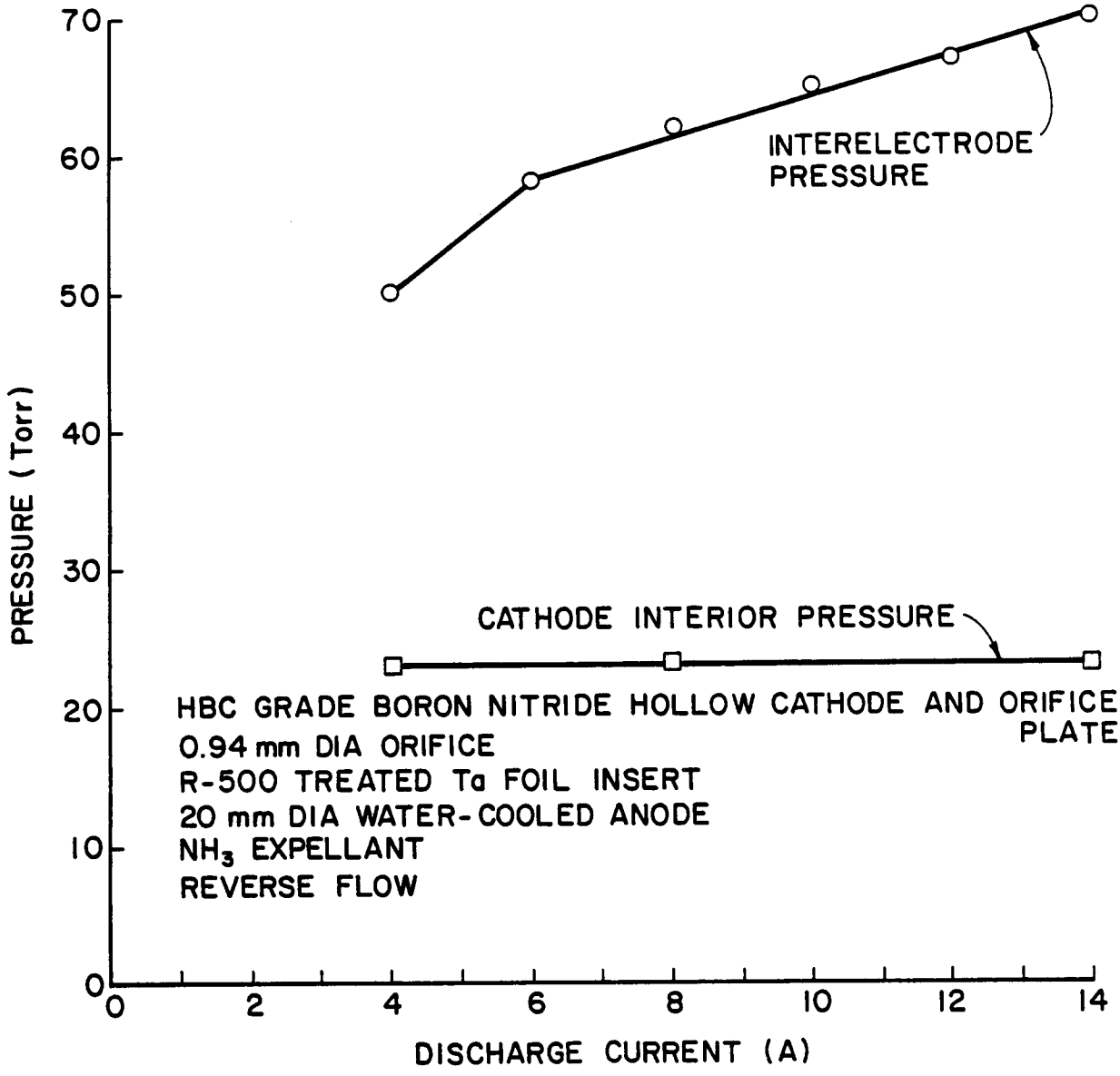

Fig. 52 Effect of Discharge Current on Operating Pressures at Constant Reverse Flow

voltage versus inter-electrode pressure curves shown in Fig. 53. In cases reported in Figs. 52 and 53 the higher current results in a lower anode voltage due to a negative resistance phenomenon that has been recognized and described previously.[9] This occurs because plasma resistivity is proportional to the ratio of electron collision frequency to electron density and increasing the discharge current causes the electron density to increase more rapidly than the collision frequency. As the data of Fig. 53 suggest the discharge extinguished repeatedly at a 50 Torr interelectrode pressure but at pressures near 220 Torr it began to fail as a result of boron nitride melting which led to orifice erosion followed by rapid degradation of the insert. This degradation occurred when the orifice had enlarged to the point where cathode interior pressures were sufficiently large so the emission spot on the insert was small and localized overheating occurred.

Because the objective of the research effort was to demonstrate hollow cathode operation at high interelectrode pressures repeated attempts were made to operate at these pressures using a variety of different cathode designs. On one occasion for example operation of an HBC grade boron nitride cathode with a 1.2 mm dia orifice in the normal flow configuration was extended to an interelectrode pressure of 600 Torr. Between pressures of 1 and 300 Torr the discharge appeared to be stable, and at pressures above 300 Torr, the discharge was somewhat unstable and the anode voltage fluctuated with a 20 V amplitude and a fraction of a second period. The mean anode voltage required to sustain the discharge as shown in Fig. 54 for this test was relatively constant in the range of 100 to 130 V at pressures from 100 to 600 Torr. These voltages were lower than the 200 V values reached at pressures near 200 Torr is previous tests (see Fig. 53 for example) presumably because of the normal flow environment and this apparently facilitated operation to the higher interelectrode pressures. With the normal flow, however, the interior cathode pressure became very high and this caused severe melting and erosion of the boron nitride orifice plate and rapid destruction of the insert. In fact post-

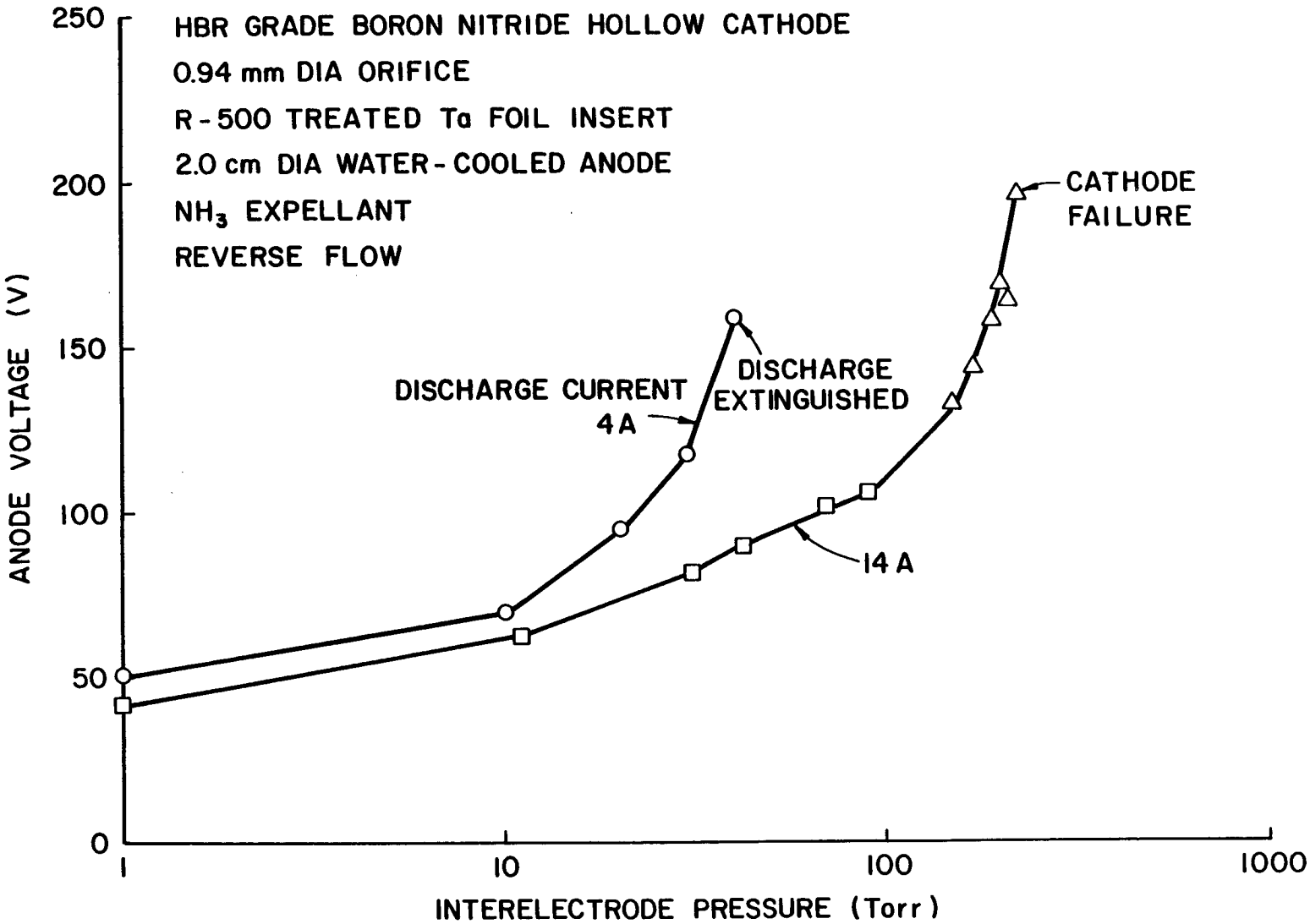

Fig. 53 Effect of Discharge Current on Anode Voltage vs. Interelectrode Pressure

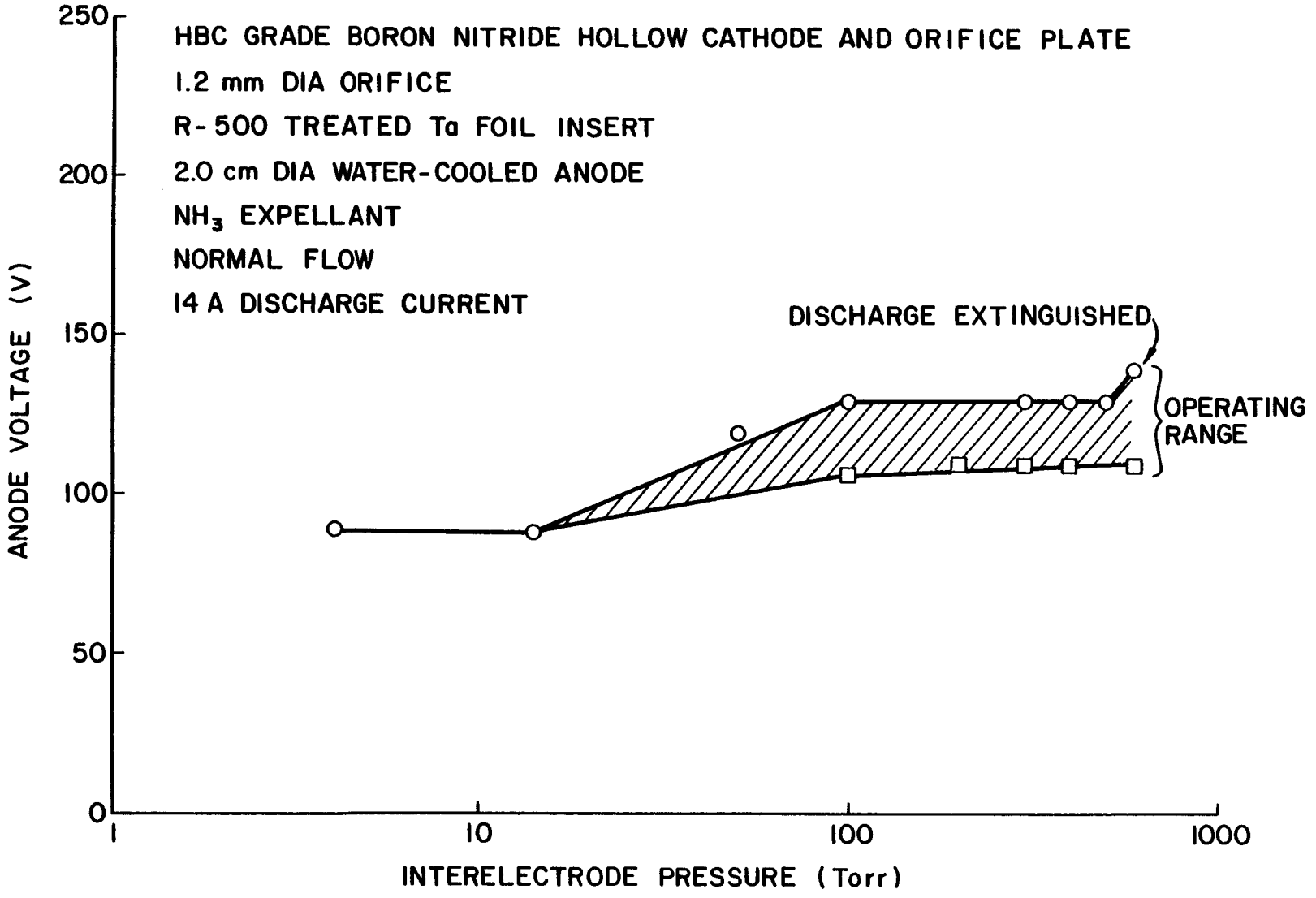

Fig. 54 Voltage/Pressure Characteristic for Normal Flow Case

operation inspection of the cathode interior showed the insert had completely disintegrated. A boron nitride-tantalum mass from which electron emission was apparently occurring appeared to remain in its place. The same test was attempted using reverse flow, but the boron nitride near the orifice melted repeatedly making it impossible to maintain low interior cathode pressures. When high interior cathode pressures do develop because of normal flow or orifice enlargement when reverse flow is being used, it appears the insert emission region is a small overheated spot and typically emission cannot be sustained from such a spot. If an insert material like the boron nitride/tantalum mass that was produced during the collection of the data of Fig. 54 could be made to operate for long periods of time, the data of Fig. 54 suggest it might be possible to operate at high interelectrode pressures in the normal flow mode.

Because it was considered more likely that successful hollow cathode operation at high interelectrode pressures could be achieved if the cathode interior pressure could be kept sufficiently low so the electron emission region on the insert could be kept large, no search for an improved insert material was started. Rather the focus of the research was directed at maintaining the integrity of the cathode orifice so low cathode interior pressures could be sustained in the reverse flow mode of operation.

Because boron nitride orifice plates melted under the high temperatures encountered during operation, it was decided that a tungsten orifice plate should be substituted for the boron nitride one. When this cathode was operated in the reverse flow configuration, it was possible to extend operation up to interelectrode pressures of 1,000 Torr. Cathode interior pressures measured as a function of interelectrode pressure for these tests are plotted in Fig. 55. This figure shows that the interior cathode pressure remained below 10 Torr over the entire interelectrode pressure range. The

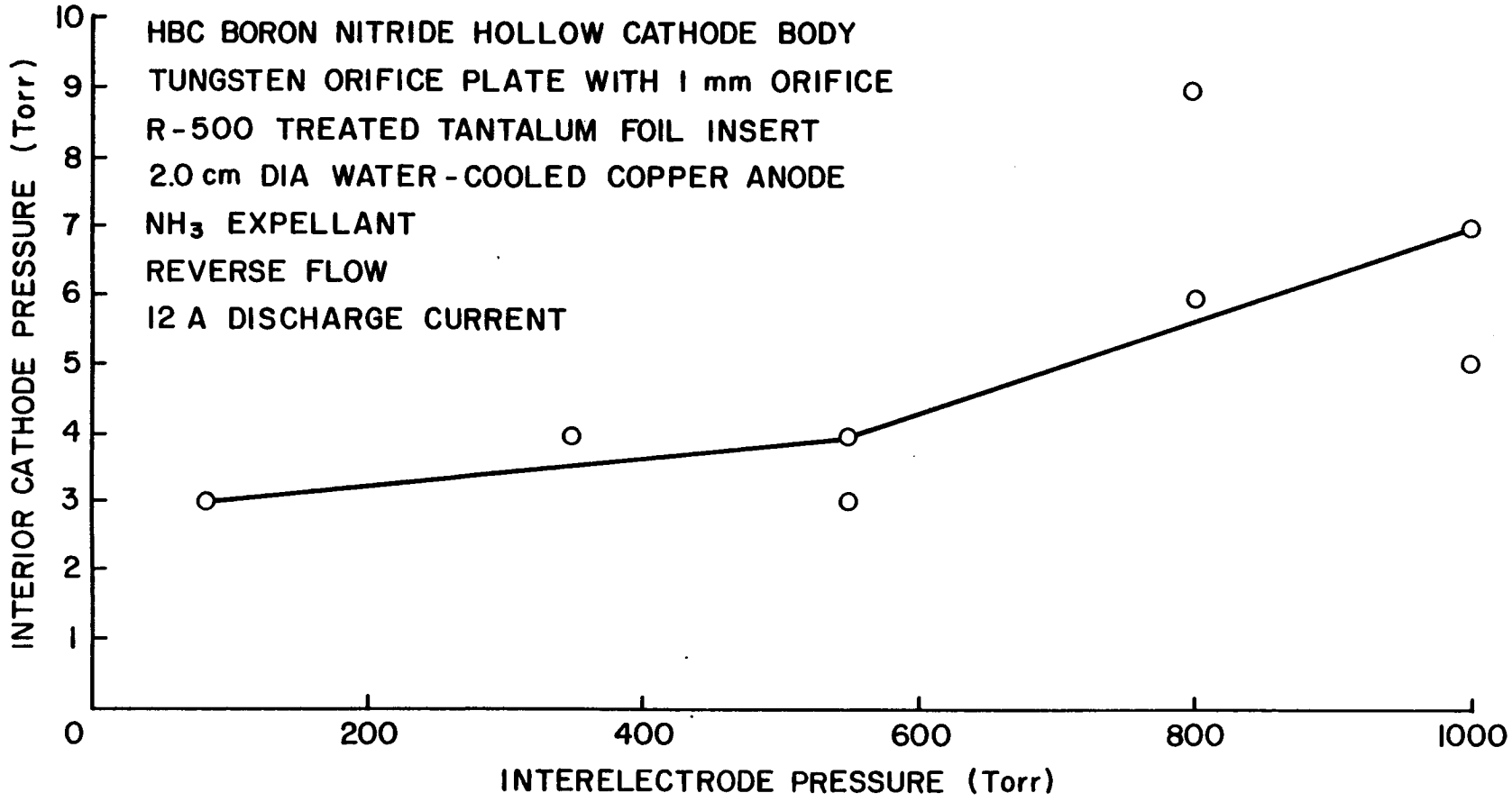

Fig. 55 Interior Cathode Pressure vs. Interelectrode Pressure

interior cathode pressures observed with the 1 mm dia orifice used in the test are much lower than expected. In addition the data show quite a bit of scatter. After the test had been completed and the cathode disassembled, it was observed that a small object, presumably boron nitride, was partially blocking the orifice in the tungsten plate and apparently causing of both the low interior cathode pressures and the data scatter. The anode voltage during this same test is shown plotted as a function of interelectrode pressure in Fig. 56. During the tests that the discharge operated stably at both the 12 A discharge current pertaining to Figs. 55 and 56 and at lower current levels. The discharge could not be observed visually during the tests, but it is believed based on subsequent tests where the discharge could be seen that the current was flowing in the form of a thin moving filament from the orifice radially outward toward the anode. After about 30 minutes of testing this current filament apparently caused the ceramic adhesive holding the tungsten orifice plate in place to loosen and erode. This eventually resulted in the opening of a flow passage between the interelectrode and cathode interior regions which allowed the cathode interior pressure to increase and the insert to degrade rapidly.

In an effort to overcome the tendency of the discharge to melt a hole between the tungsten orifice plate and the boron nitride body a configuration which used a tungsten orifice plate electron beam welded to a tantalum cathode body in the manner shown in Fig. 46 was tested. These attempts to operate the tantalum body cathode shown in Fig. 46 were completely unsuccessful. Immediately after startup it appeared that the quartz tube, which insulated the insert from the cathode tube melted. This allowed the insert to come in contact with the cathode tube and as a result the discharge apparently transferred from inside the cathode to a point on the edge of the tungsten orifice plate. An attempt to use a boron nitride insulator in place of the

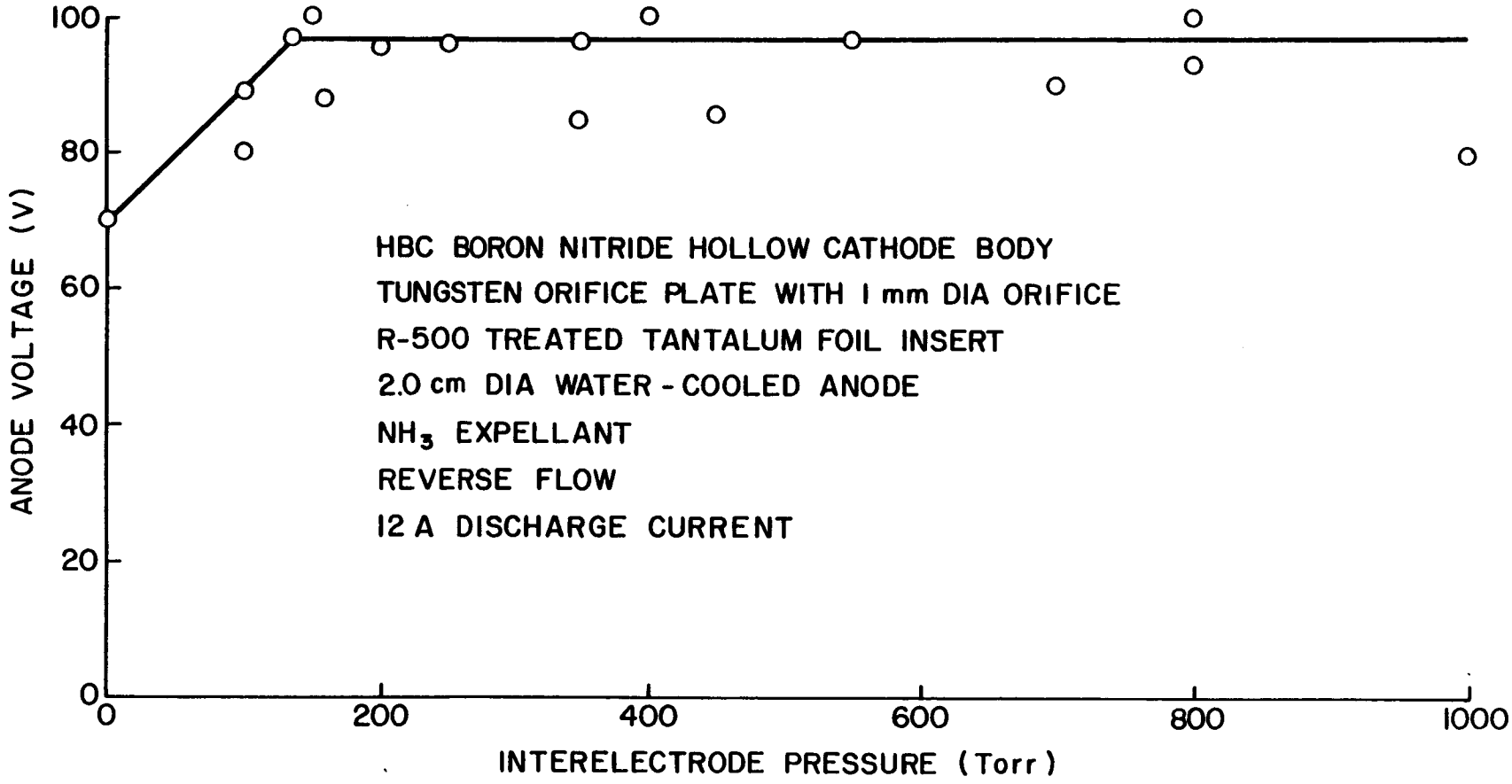

Fig. 56 Anode Voltage vs. Interelectrode Pressure

quartz tube insulator shown in Fig. 46 was also unsuccessful.

It was felt that the difficulties encountered with the tungsten orifice plate electrode beam welded to the tantalum cathode body could be overcome if the diameter of the assembly could be increased beyond the 0.7 cm value that was being used. Larger tantalum and tungsten assemblies, however, could not be located and so it was decided to attempt to make relatively large diameter (~1.5 cm) graphite caps. Three graphite orifice cap configurations were tested in conjunction with the boron nitride cathode body; anode voltage versus interelectrode pressure characteristics like those shown in Fig. 57 were observed. These characteristics are very similar to those observed with the tungsten orifice plate. When the cylindrical orifice cap having the centered orifice was removed and examined after the tests, hemispherical pits were observed at the outside edge of the cap near the anode. Their appearance suggested the discharge may have been coming from the cap surface rather than through the orifice. To prevent this, the semi-conical cap configuration was tested but again the discharge pitting suggestive of emission sites on the outside surface of the cap were apparent near the outer edge of the cap. Even when the orifice was offset and data represented by the squares in Fig. 57 were obtained, this pitting effect was still observed. It should be noted that in all cases described the insert was isolated from the orifice cap by the boron nitride so if emission was occurring from the outside surfaces of the orifice caps the discharge current had to be flowing from the insert to the inside of the orifice cap, through the orifice cap and then from the exterior of the orifice cap to the anode.

In all of the tests that utilized boron nitride or graphite at the orifice boundary, evidence of orifice enlargement was found after the associated tests had been completed. This enlargement as well as pitting observed on the outside of the

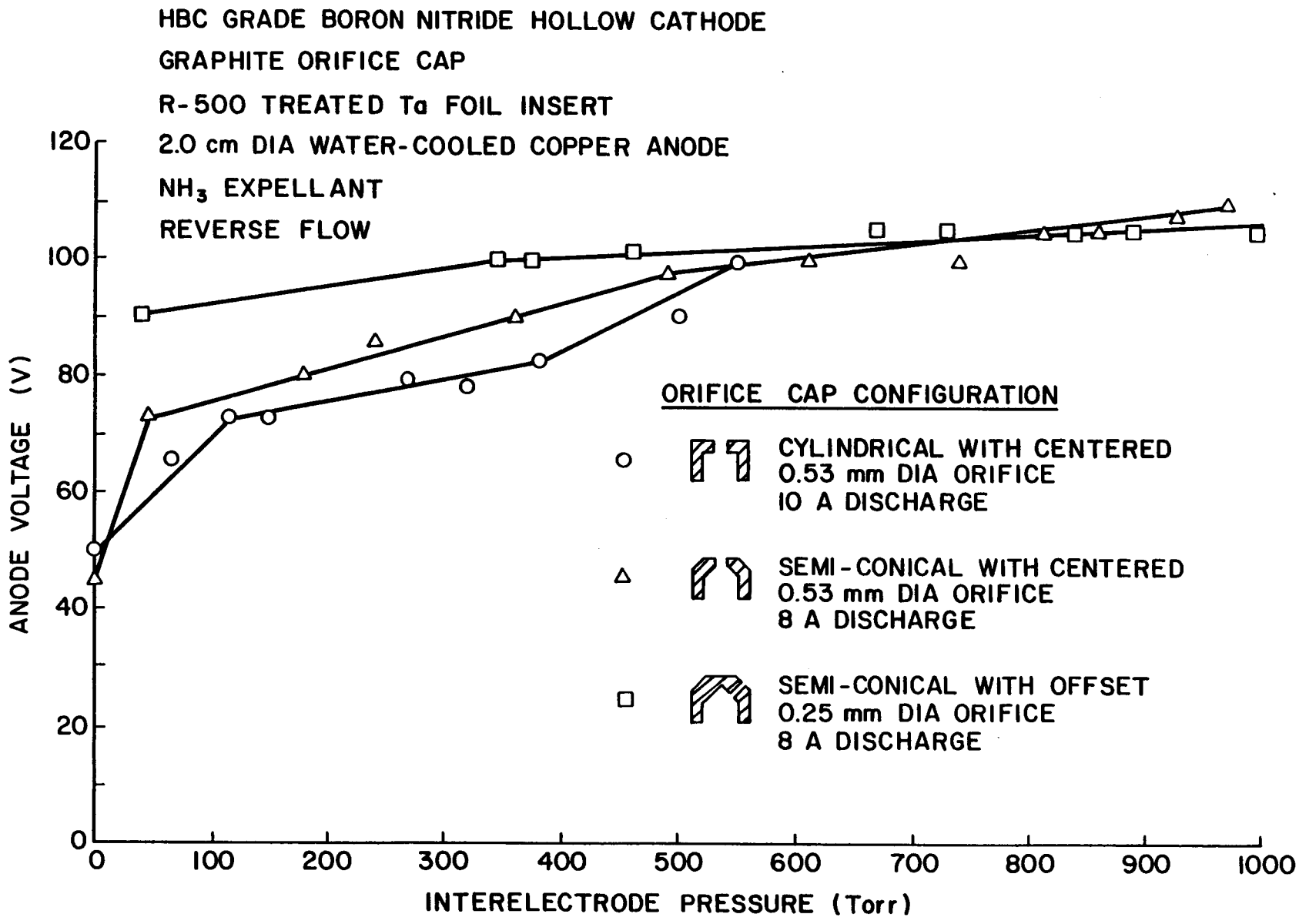

Fig. 57 Effect of Orifice Cap Configuration on Voltage/Pressure Curve

graphite cap must have been caused by a combination of discharge-induced heating, sputtering and chemical attack between the carbon or boron nitride and ammonia. After one 30 minute period of operation a new graphite cap was observed to have been eroded completely through the side of the orifice cap. In this case it appeared that the discharge had attached itself to the exterior of the cap at a location near the anode and discharge-induced erosion had eventually resulted in hole completely through the cap wall. Tungsten orifice plates on the other hand did not show any evidence of orifice enlargement during the conduct of tests that utilized them. It also appeared that insert degradation frequently accompanied cathode operation as evidenced by increases in anode voltage at a particular operating condition. During the tests conducted with the graphite and tungsten orifice regions the discharge could not be observed directly so it is not known when or if the discharges actually began to pass through the cap wall rather than through the orifice.

Conclusions

Hollow cathodes can operate on ammonia at interelectrode pressures up to the 1,000 Torr range where arcjets operate, but it is not known at this time if they operate in the conventional manner, i.e. so the discharge current passes through the cathode orifice under all conditions. If the cathode orifice plate is made from an electrical conductor the current may flow from the insert through the cathode interior plasma and then through the conducting orifice plate to couple to the interelectrode plasma under some conditions. In view of this, the following criteria have been identified as necessary but not sufficient conditions for high pressure hollow cathode operation.

1. The cathode interior pressure should be maintained at a low value ($\lesssim$10 Torr).

This can be realized by using reverse flow through an orifice with a sufficiently small diameter so the 10 Torr pressure is sustained within the cathode interior. The low cathode interior pressure is required to prevent emission from a tiny spot which eventually results in localized overheating and damage to typical insert materials.

2. The insert must be electrically isolated from the orifice plate. This condition ensures electron emission spot migration from the insert to the cathode exterior does not occur at high pressures. Under conditions where the orifice plate is made of an insulating material, it can be stated that the discharge is coming from the insert through the orifice. If the orifice plate is made of an electrically conducting material this statement cannot be made. In this case the discharge may pass from the insert through the interior plasma to the interior surface of the orifice, through the orifice plate, from a second emission site on the exterior of the orifice plate and finally through the interelectrode plasma to the anode.

3. The orifice plate must be made of a material that can tolerate a high temperature and is chemically non-reactive with the ammonia expellant if long-term operation is to be realized.

For these tests it was necessary to water-cool the anode at high interelectrode pressures to prevent the anode from overheating due to the large voltage drop across the anode sheath.

VERIFICATION OF RING CUSP DISCHARGE CHAMBER PERFORMANCE

Jason Vaughn

Introduction

The ring cusp discharge chamber having a cathode adjacent to the screen grid has been shown by Hiatt[12] to exhibit optimum performance when the anode is positioned downstream of the magnetic ring cusp at the optimum "virtual anode" location. This optimum performance was also determined by the location of the virtual cathode which was in turn determined by the position of the ring magnet and the size of the filament cathode used to supply electrons to the discharge. A study intended to provide further insight into the discharge chamber optimization process was initiated on the same 8 cm ring cusp discharge chamber used by Hiatt. The objective of the first phase of this work was to verify his best performance results. In order to do this it was necessary to first adjust the discharge chamber geometrical parameters to the values used by Hiatt and then to measure the discharge chamber performance. Experimental results obtained from this study will be analyzed in terms of the discharge chamber model developed by Brophy[8] and performance will be characterized in terms of the plasma ion energy cost (ε_p) and the extracted ion fraction (f_b) parameters which form the basis of this model

Apparatus and Procedure

The 8 cm dia ring cusp discharge chamber used in this verification study is shown schematically in Fig. 58. All of the symbols used to define the discharge chamber dimensions that can be varied are defined in this figure. The magnetic field associated with this discharge chamber is constructed by placing one magnet on the centerline at the rear of the chamber and

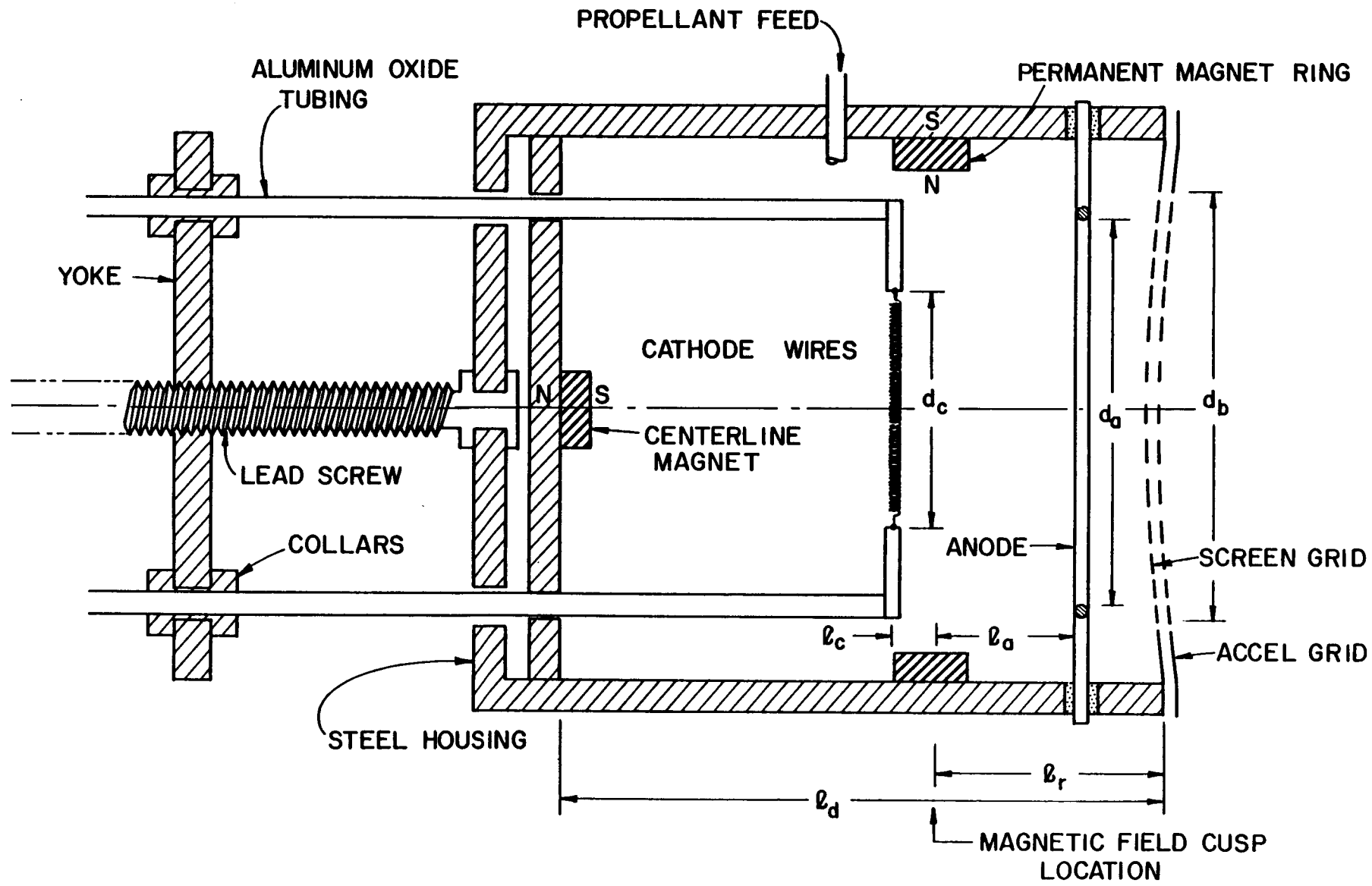

Fig. 58 Movable Loop Anode Discharge Chamber

arranging a ring of magnets end-to-end around the circumference of the wall. The 1.9 cm by 1.3 cm by 0.6 cm samarium cobalt magnets used to construct the field have a flux density of 0.27 Tesla at their surface. They are arranged so the polarity of the outward facing surface of the magnets comprising the ring is opposite to that of the single magnet at the rear of the chamber.

The cathode used in the discharge chamber is a 0.25 mm dia tungsten wire formed into a loop of diameter 3.1 cm. This loop is located 1.4 cm upstream of the screen grid. Under the action of the lead screw and yoke the 5.2 cm dia copper anode could be moved through the region between the axial location of the ring cusp and the axial location of the cathode loop. The grids had a cold spacing of 0.86 mm, the screen grid holes had diameters of 1.9 mm, the accelerator (accel) grid holes generally had diameters of 1.5 mm although a few near the centerline had enlarged to 1.7 mm as a result of sputter erosion, and the hole-to-hole spacing in both grids was 2.2 mm. The screen grid potential was 750 V positive and the accel grid was maintained at -250 V throughout the study. The argon propellent used to conduct the research was fed into the discharge chamber through the sidewalls in the manner shown in Fig. 58. The ball jar used was 46 cm in dia. and it was diffusion pumped to an ultimate pressure in the low 10^{-6} Torr range and operating pressures that were typically in the mid to low 10^{-5} Torr range. Neutral densities in the discharge chamber and propellant utilization data associated with its operation were corrected for neutral back flow into the discharge chamber from the bell jar. An electrical schematic diagram showing where power supplies are connected to the ion thruster and the points at which measurements are made is shown in Fig. 59.

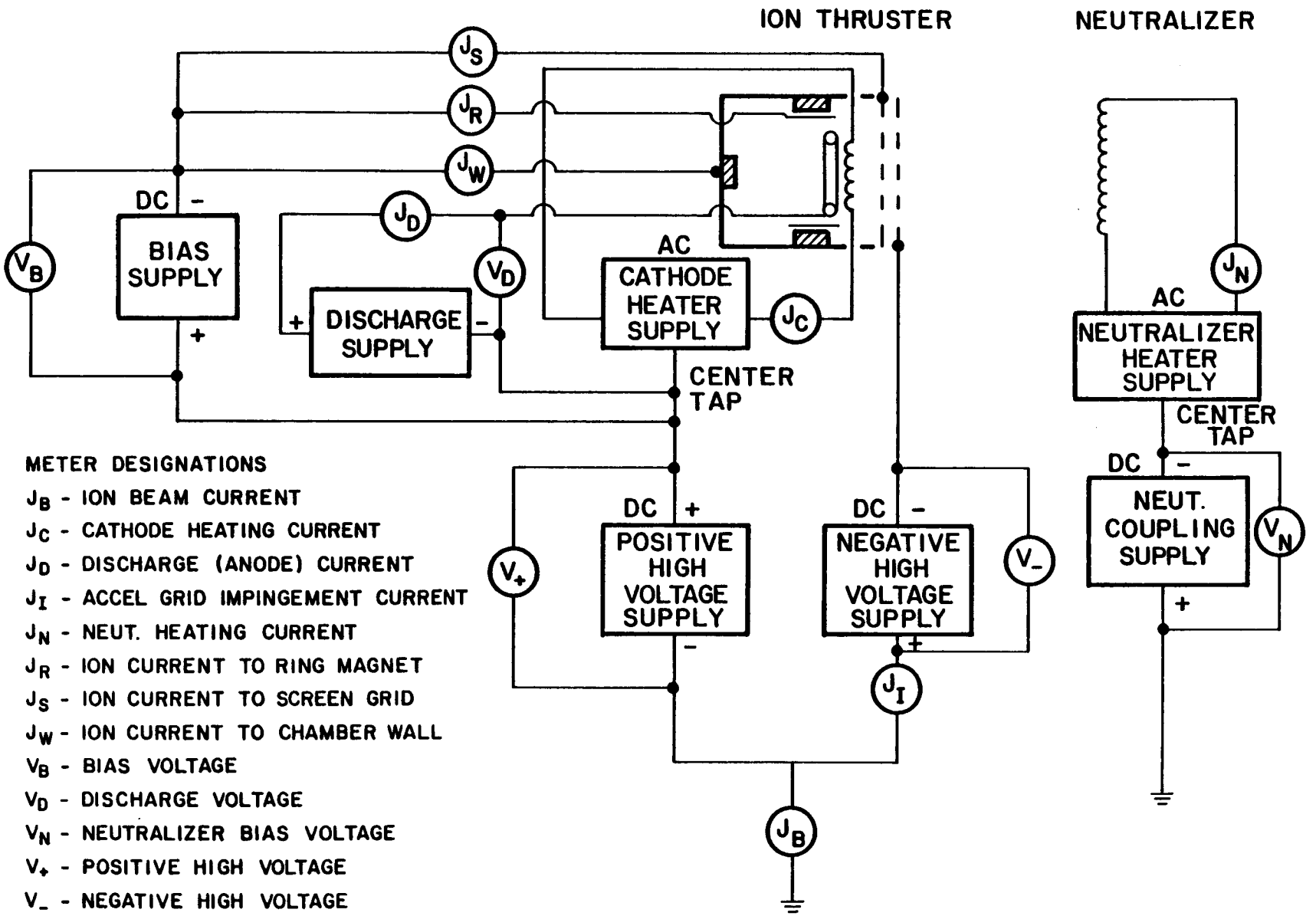

Fig. 59 Ring Cusp Ion Thruster Electrical Schematic

The basic test procedure used involved first establishing a flowrate ($\dot{m}$) in the range between 100 and 500 mA eq., then heating the cathode, starting the discharge and allowing it to stabilize. Typically this stabilization took place at a discharge voltage (V_D) of 50 V and a moderate discharge current ranging from 200 to 300 mA. After stabilization the discharge current was varied incrementally from 100 to 1,500 mA and the beam current (J_B) and ion production expressed as a current (J_p) were measured. The ion production current was measured by biasing the chamber walls and the screen grids 30 V negative of the cathode and measuring the ion currents arriving at these surfaces. The plasma ion energy cost (ε_p) and the extracted ion fraction (f_b) were calculated using these measured currents. The procedure was repeated over a range of flowrates from 100 to 500 mA eq and then the loop anode was moved downstream (ℓ_a in Fig. 58 was increased incrementally from its initial location at the ring cusp). At each incremental location the discharge current was again varied through the 100 to 1500 mA range and the currents and voltages of interest were measured. This process continued until the anode was sufficiently far downstream so the discharge was on the verge of extinction. This corresponded to the optimum performance configuration in agreement with Hiatt's results. The beam diameter d_b was kept constant at 8 cm throughout this test, however, some adjustments in the ring cusp location ℓ_r and the cathode diameter d_c were effected in an effort to reproduce Hiatt's test configuration exactly.

Results

A typical plot of plasma ion energy cost versus neutral density parameter generated using data collected in the manner just described is shown in Fig. 60. The trial-and-error procedure used to fit the curve to the data involves selecting values for the primary electron containment factor (C_o) and the

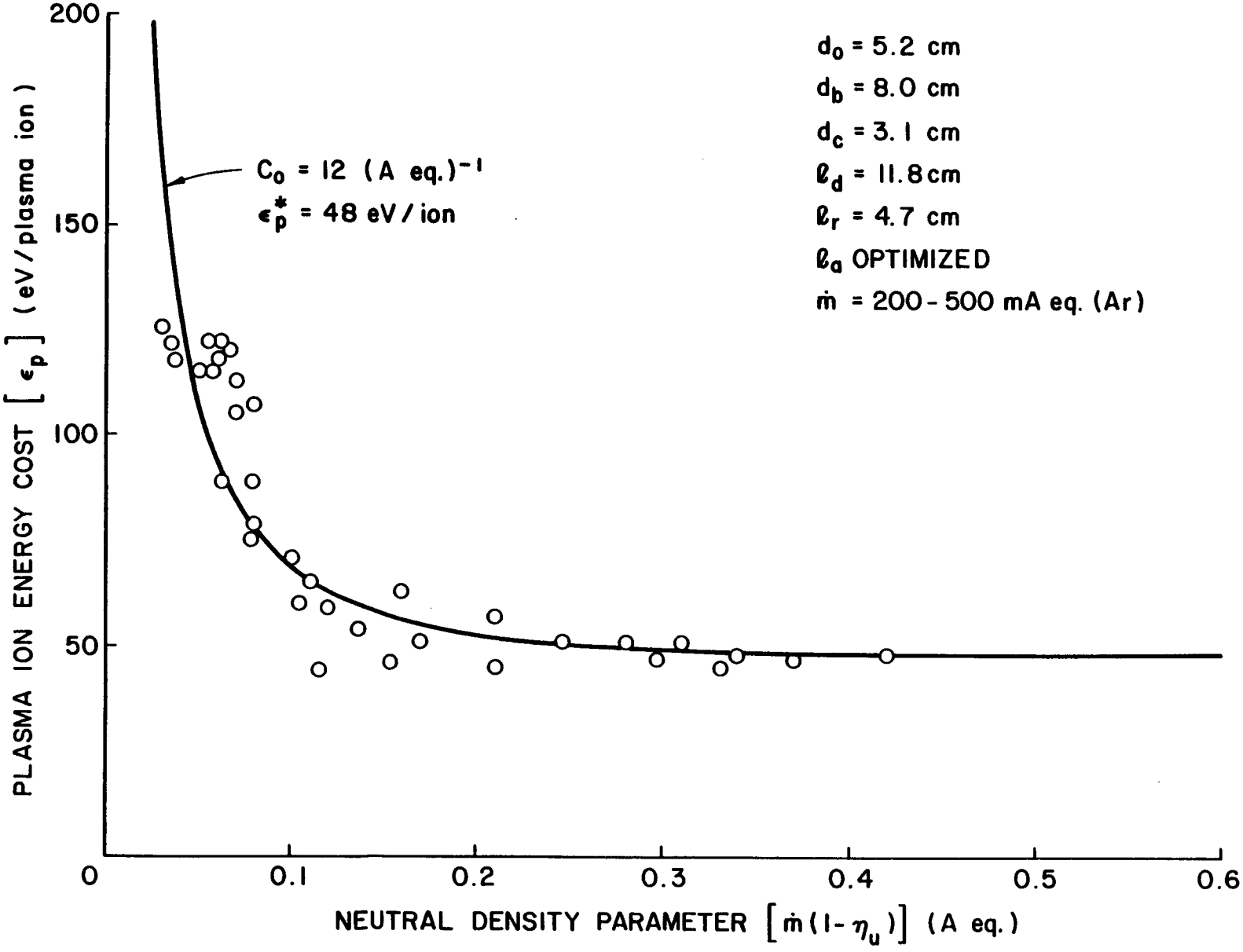

Fig. 60 Typical Plasma Ion Energy Cost Curve

baseline plasma ion energy cost (ε_p^*). This plot shows typical data scatter observed during a typical experiment. To avoid the clutter associated with many data points on curves that are located close together the actual data points will be left off of subsequent plots.

Figure 61 shows how varying ring cusp location (ℓ_r) affects the performance of the thruster operating with a 3.1 cm dia cathode and a 5.2 cm dia anode. This figure indicates that there is an optimum ring cusp location at ℓ_r of 4.7 cm at which the value of the primary electron containment factor is 12 $(A\ eq)^{-1}$ and the baseline plasma ion energy cost is 48 eV/ion. To describe the performance of the ion source completely using the model developed by Brophy[8] one must calculate the extracted ion fraction. The effect of ring cusp location on this fraction is shown in Fig. 62. The data points in this figure are actually mean values of the extracted ion fraction recorded during data collection of data over the range of neutral density conditions investigated at each ring cusp location. These data show the extracted ion fraction reaching a very mild peak of ~0.42 at a ring cusp location of 4.7 cm. Because a minimum plasma ion energy cost and a maximum extracted ion fraction were both observed at a 4.7 cm ring cusp location, the beam ion energy cost versus propellant utilization curve should also be optimal at this condition. Figure 63 shows how ring cusp location affects ion thruster performance when the anode is positioned downstream of the ring cusp at the point where the discharge is on the verge of extinction (optimized location). This figure indicates thruster performance is optimal when the ring cusp is at an ℓ_r of 4.7 cm for the ion source described by the parameters listed in the legend. It should be noted that the anode was positioned to yield optimum performance at each ring cusp location associated with the curves of Fig. 63. It is believed that the optimum performance shown in these data corresponds to a ring cusp location that causes

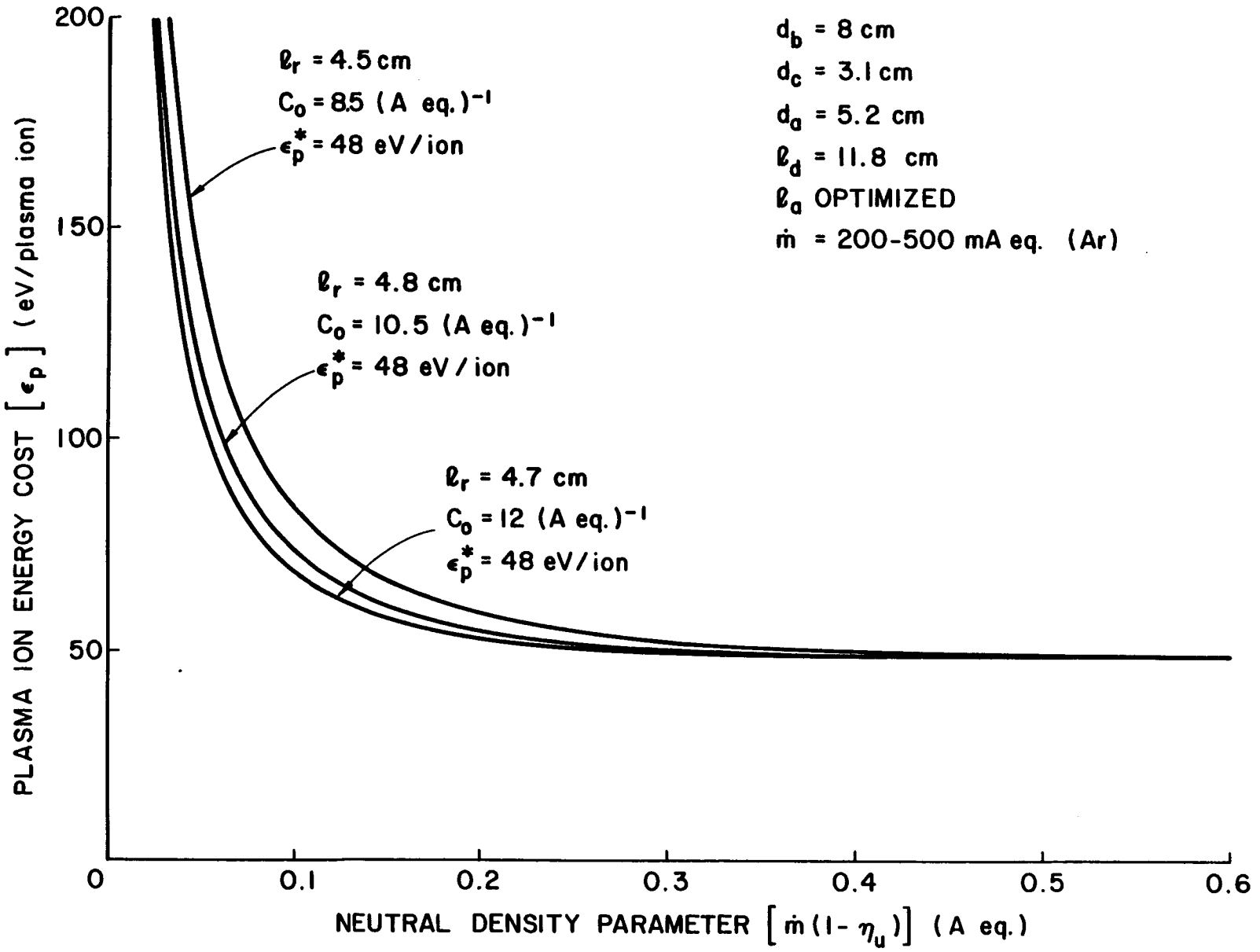

Fig. 61 Effect of Ring Cusp Location on Plasma Ion Energy Cost Curves

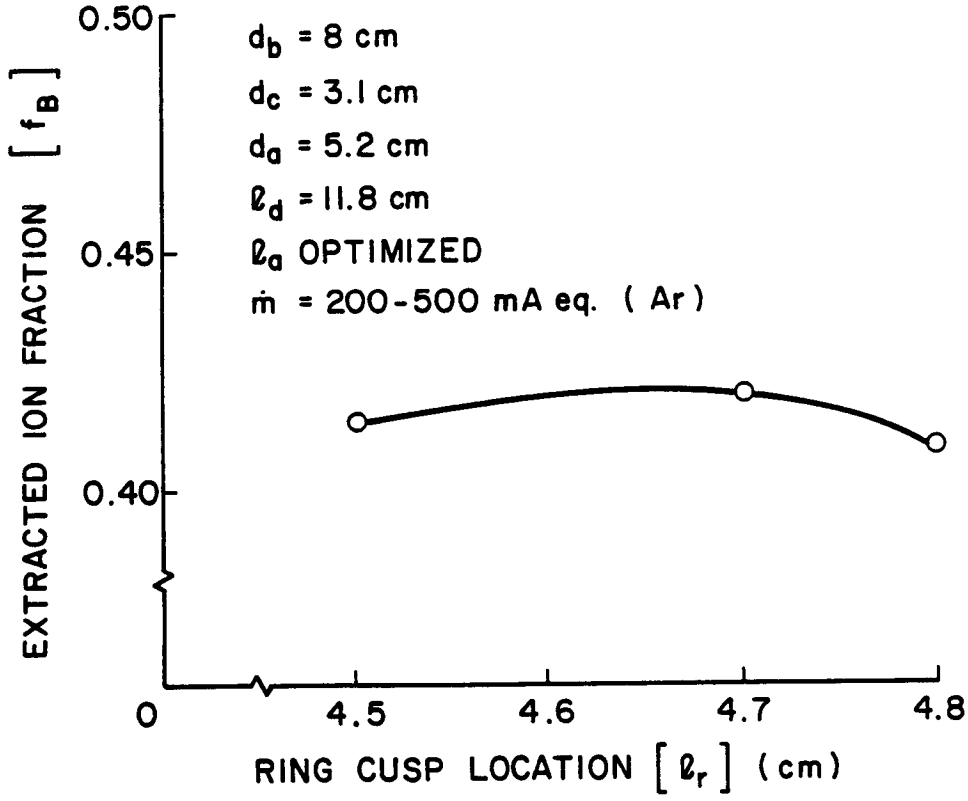

Fig. 62 Effect of Ring Cusp Location on Extracted Ion Fraction

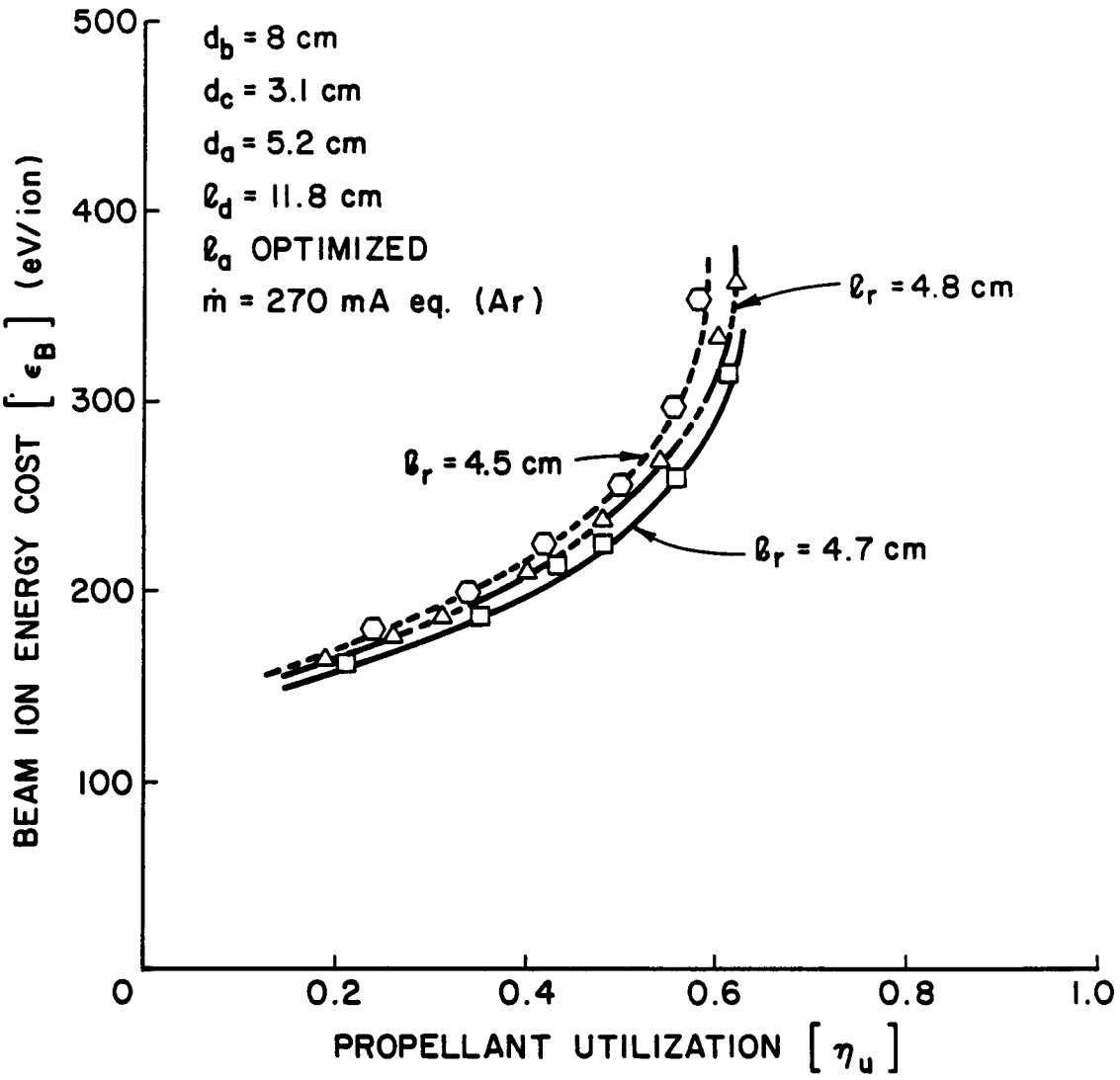

Fig. 63 Effect of Ring Cusp Location on Beam Ion Energy Cost

the virtual anode magnetic field line to intercept the outer most ring of holes in the screen grid. At this condition optimum use is being made of the screen grid. Movement of the virtual anode field line in either direction would degrade performance. Moving the virtual anode field line further out would cause significant numbers of the ions being produced to be directed beyond the outer-most holes in the screen grid onto the region of the grid where there are no extraction holes and onto the discharge chamber wall. Ions that strike these surfaces pick up an electron and they therefore come off of the surfaces as atoms and they must be reionized thereby using additional energy before they can be extracted as ions. On the other hand moving the virtual anode field line at the screen grid further in would reduce the ion current through the outer-most holes in the screen grid while neutral atoms would still be able to escape the discharge chamber through these holes. This also induces a degradation in discharge chamber performance. It is the balancing of these two competing effects that determines the optimum virtual anode field line location.

By operating the thruster at the optimum ring cusp location it was possible to make a comparison of the optimized data obtained in the present tests with those obtained previously by Hiatt.[12] Figure 64 shows such a comparison at a relatively high argon flowrate (380 mA eq) and these data show good agreement. At a reduced flowrate of 270 mA eq., however, the data of Fig. 65 were obtained and they do not show such good agreement. The reason why the data agree at high flowrates and not at low flowrates is because the primary electron containment factor (C_o) as determined in the present tests was ~12 (A eq)$^{-1}$ while it was 14 (A eq)$^{-1}$ in Hiatt's tests. The baseline plasma ion energy cost and the extracted ion fraction parameters determined in past and

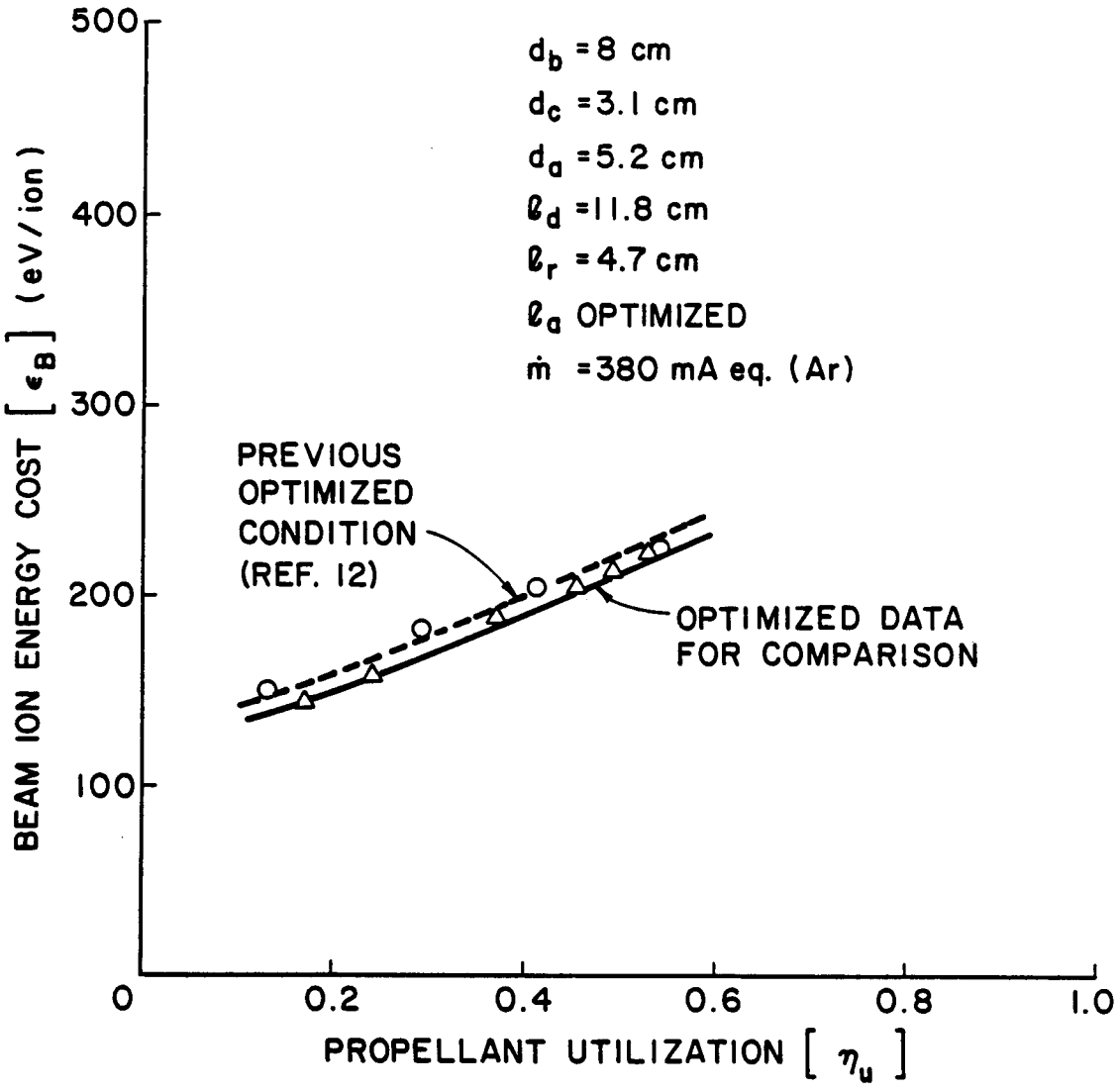

Fig. 64 Performance Comparison at High Flowrate

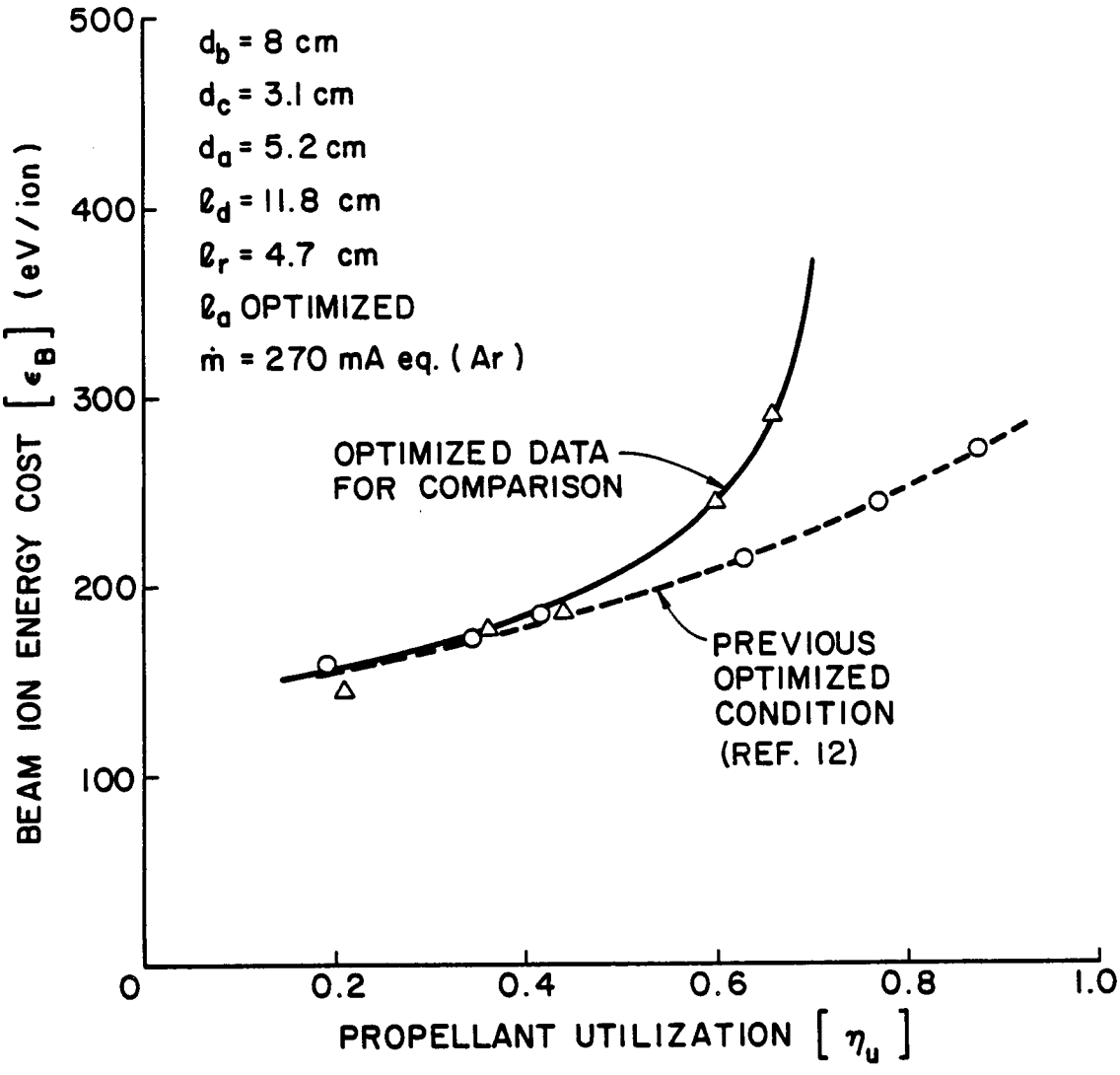

Fig. 65 Performance Comparison at Moderate Flowrate

present tests both agree well and the effects of these two parameters dominate and cause the good agreement observed in Figs. 64 and 65 at low propellant utilizations.

There are several reasons why the primary electron containment factor could be lower in the present set of experiments than in Hiatt's tests. The measurement of the neutral flow into the discharge chamber could be in error in either of the experiments. The two sets of data would agree if a neutral flow loss due to a leak or a neutral flow measurement error of 60 mA eq could be identified in the current experiments. The difference could also be explained if somehow the magnetic field were not containing primary electrons as effectively in the present experiments as it did in Hiatt's tests. To date, it has not been possible to identify errors of this type in the present experiments or to find an indication of errors in the opposite sense that occurred in the previous set of experiments.

Conclusion

Verification of experimental results obtained previously by Hiatt has been achieved at flowrates above about 380 mA eq. At lower flowrates an error has been identified that could be explained by a loss of 60 mA eq of neutral atoms in the present experiments. In general the trends and tendencies observed by Hiatt were confirmed in the present study. By varying the ring cusp location for a particular discharge chamber geometry a location was found that yielded optimum performance. With the ring cusp at this location, it is believed that the virtual anode magnetic field line intercepts the outer most ring of holes in the screen grid. This results in optimum utilization of the screen grid by facilitating ion extraction over the complete open region of the screen grid without allowing substantial numbers of ions to pass beyond the outer-most holes in the screen grid to a region of the discharge chamber where they recombine and are lost.

HIGH CURRENT HOLLOW CATHODE RESEARCH

There is an anticipated need for a high current (~50 A) xenon hollow cathode in electrodynamic tether plasma contactor and high-power ion thruster applications. Currently available hollow cathodes have been tested to 10 and 20 A levels and it might be possible to extend their operating envelope to this current. However, it is considered desirable to analyze present hollow catnode designs to determine if 2 to 5-fold increases in operating current levels might cause operational problems. In order to do this the hollow catnode model developed by Siegfried[11] was programmed and exercised to determine the operating conditions that might be expected at the 50 A emission current level. The key design parameters associated with this model which are used in the analysis are illustrated in Fig. 66.

The hollow cathode shown in Fig. 66 consists of a cathode tube and orifice plate enclosing a low work function insert from which electrons are extracted. The basis of the Siegfried model is that electrons, emitted from the downstream segment of the insert having a length ℓ_e are drawn into the region enclosed by the dotted line in Fig. 66. It is argued that within this region the plasma potential, plasma density and electron temperature are relatively constant and that primary electrons emitted from the insert undergo ionizing collisions with the neutral gas atoms which are also present within this region. This neutral gas is maintained at the pressure P in the region by expellant gas which is fed in at a flowrate $\dot{m}$. Electrons in the region, which are botn drawn from the insert and produced as a consequence of ionization, are extracted through an orifice of diameter d_o to an anode located downstream of the orifice plate. Ions produced in the discharge are on the other hand, extracted across the dotted line boundary to the insert, orifice

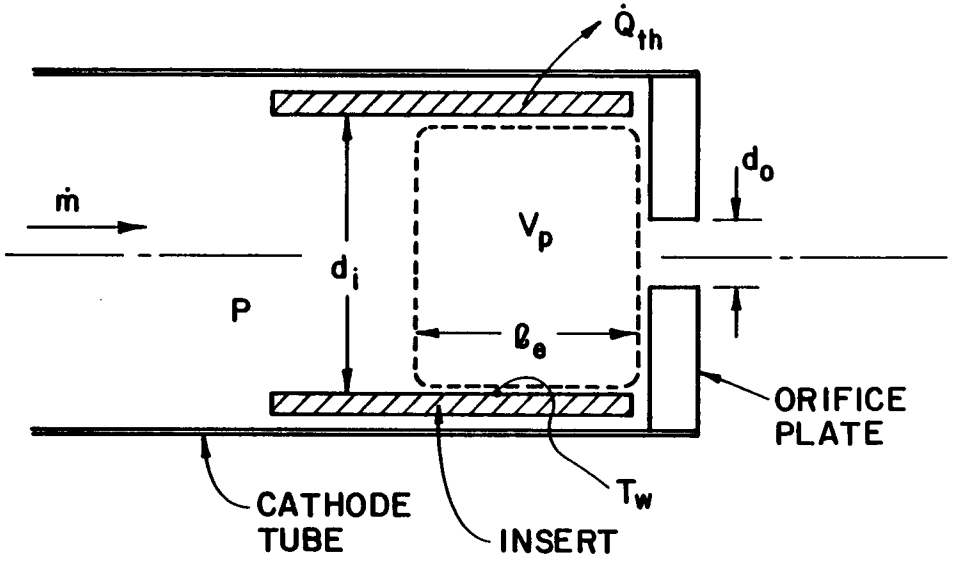

d_i = INSERT DIAMETER

d_o = ORIFICE DIAMETER

ℓ_e = EMISSION REGION LENGTH ON INSERT

$\dot{m}$ = EXPELLANT FLOW RATE

P = INTERIOR CATHODE PRESSURE

$\dot{Q}_{th}$ = HEAT LOSS RATE FROM INSERT

T_w = INSERT WALL (SURFACE) TEMPERATURE

V_p = PLASMA POTENTIAL WITHIN CATHODE

Fig. 66 Hollow Cathode Terminology

plate or cathode tube. Those ions crossing the boundary adjacent to the insert strike the insert thereby heating it to sustain its temperature and facilitate electron emission through the field-enhanced thermionic emission mechanism. The Siegfried model applies the equations of conservation of energy at the insert surface, conservation of energy within the ionizing volume, conservation of ion current lost from the ionizing volume at the Bohm velocity and electric field enhanced electron emission from the insert to determine the relationship between the variables indicated in the legend of Fig. 66. In order to apply the model it is necessary to assume only an electron temperature for the plasma within the dotted boundary and a value for the ratio of emission region length (ℓ_e) to primary electron scattering mean free path since other design variables are defined. The present analysis assumes 0.7 eV and unity respectively for the parameters on the basis of xenon hollow cathode experiments conducted by Siegfried on xenon at low currents[13].

Simultaneous solution of the equations just described yields results such as those shown in Fig. 67 for a 50 A xenon cathode with an insert diameter of 0.5 cm and an insert work function of 2.1 eV. The upper plot of Fig. 67 shows insert temperature variation as a function of emission region length ℓ_e with the heat removal rate from the insert $\dot{Q}_{th}$ as a parameter varying from 200 W to 1000 W. This heat removal rate from the insert is determined in a piece of hardware by such parameters as the thermal contact resistance between the insert and the cathode body, the radiative heat transfer environment of the cathode and the thermal conductance of the cathode tube between the insert and some structure tending to remain at a fixed temperature. It should be noted that the heat removal rates indicated of Fig. 67 are one or two orders of magnitude greater than those computed for previously tested low-current cathodes[11] but they are considered appropriate for operation at the high current involved.

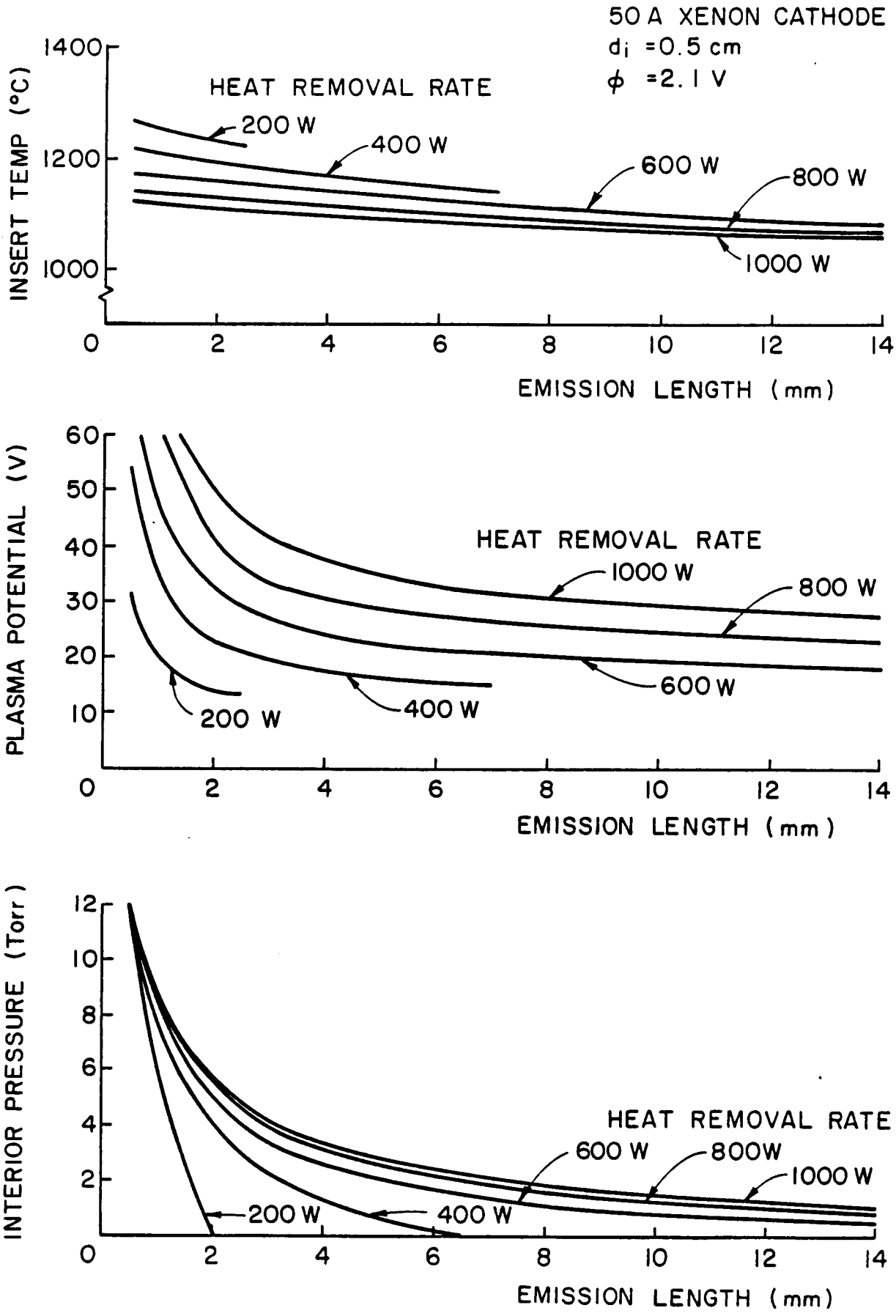

Fig. 67 Effect of Heat Removal Rate and Emission Region Length on Cathode Performance Parameters

The data in the upper plot of Fig. 67 show that insert temperatures in excess of 1200°C will be realized for the full range of emission lengths associated with a 200 W heat removal rate and that the insert emission length can be expected to extend only a little beyond 2 mm in this case. As the heat removal rate is increased, the curves of Fig. 67 show the insert temperature should drop and the emission length should increase to the point where excessively high emission current densities will not be demanded. It should be noted in considering the data that an insert temperature less than 1100°C is generally preferred to prevent migration and loss of the low work function material loaded into the insert.

The middle graph in Fig. 67 shows how plasma potential within the cathode varies as a function of heat removal rate and emission length. It indicates it is desirable to operate with a long emission length in order to keep the interior plasma potential and therefore the keeper voltage low. Hence increased emission length induces both of the desirable effects associated with the top two graphs (low insert temperature and low keeper voltage). However, the desirable effect for the upper graph (lower temperature) is realized by increasing heat removal rate while the desirable effect for the lower one (lower potentials) is realized by decreasing it. On the other hand minimizing the insert heat removal rate, an operating loss, maximizes the efficiency of any hollow cathode device so in this sense it is also desirable. In view of these considerations then it is probably desirable to operate with a large emission length and small heat removal rate. The bottom plot of Fig. 67 shows the desired large emission length is achieved by operating with a low cathode interior pressure. Unfortunately the plot also shows emission length limits are encountered at low heat removal rates (a little over 2 mm for 200 W heat rejection rate and about 7 mm for the 400 W rate) where interior cathode

pressure drop to near-zero values. What is occurring here can be understood by recognizing that increases in emission length result from increases in the primary electron mean free path. This path is increases by reducing the densities of either Maxwellian electron electrons or neutral atoms. In fact, however, reducing the neutral density to zero results in a near-zero pressure. Under this condition only the Maxwellian electrons and the ions needed to conduct the current being demanded are left in the cathode and there is no mechanism to reduce the mean free path below the limit imposed by this near-zero pressure condition. It is the imposition of this limit that causes the 200 W and 400 W curves in the upper and central plots of Fig. 67 to terminate suddenly.

An overview of the data of Fig. 67 suggests the preferred operating mode involves reducing the heat removal rate (to say 200 W). Figure 68 shows plots of interior cathode pressure as a function of emission length again for the 50 A xenon cathode and a 2.1 V work function insert but for inserts having diameters that vary from 0.5 cm to 1.5 cm. These curves show that one can indeed increase the emission length at which the interior cathode pressure drops to zero. This is accomplished by increasing the insert diameter. In fact, for the 200 W heat removal rate case, increasing the insert diameter from 0.5 to 1.0 cm increases the emission length corresponding to zero interior cathode pressure from 2 to over 6 mm.

Figure 69 shows a comparison of insert temperature, plasma potential, and xenon flux through the hollow cathode (proportional to flowrate per unit area) as a function of insert length for the 50 A xenon cathode at a heat rejection rate of 200 W and for two insert diameters (0.5 and 1 cm). These data suggest that the 1 cm dia insert (solid line) facilitates operation with greater emission lengths, lower insert temperatures and acceptably low plasma potentials if the xenon flux level is kept low. Since these operating conditions are preferred, the

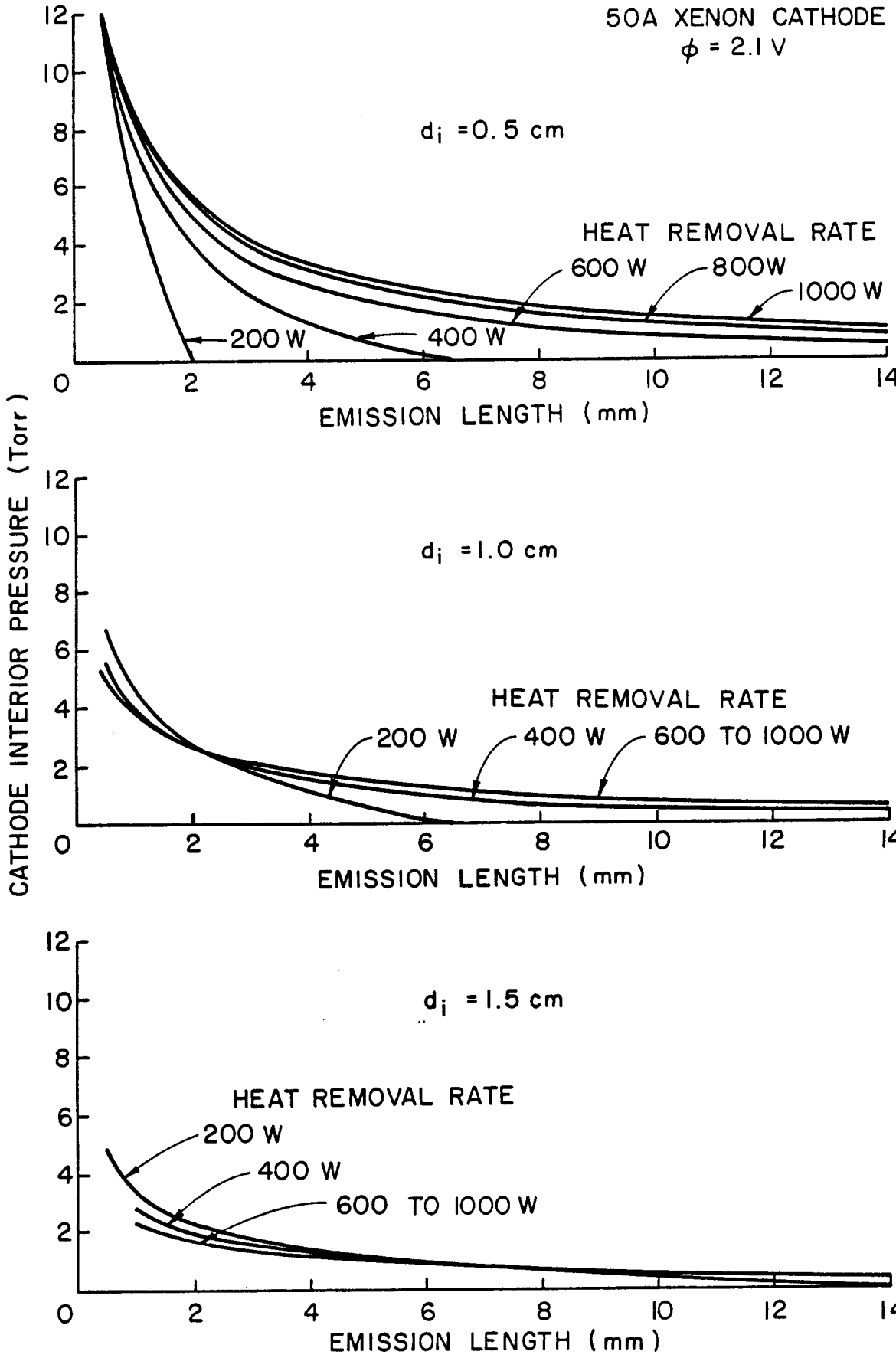

Fig. 68 Effect of Insert Diameter on Cathode Interior Pressure

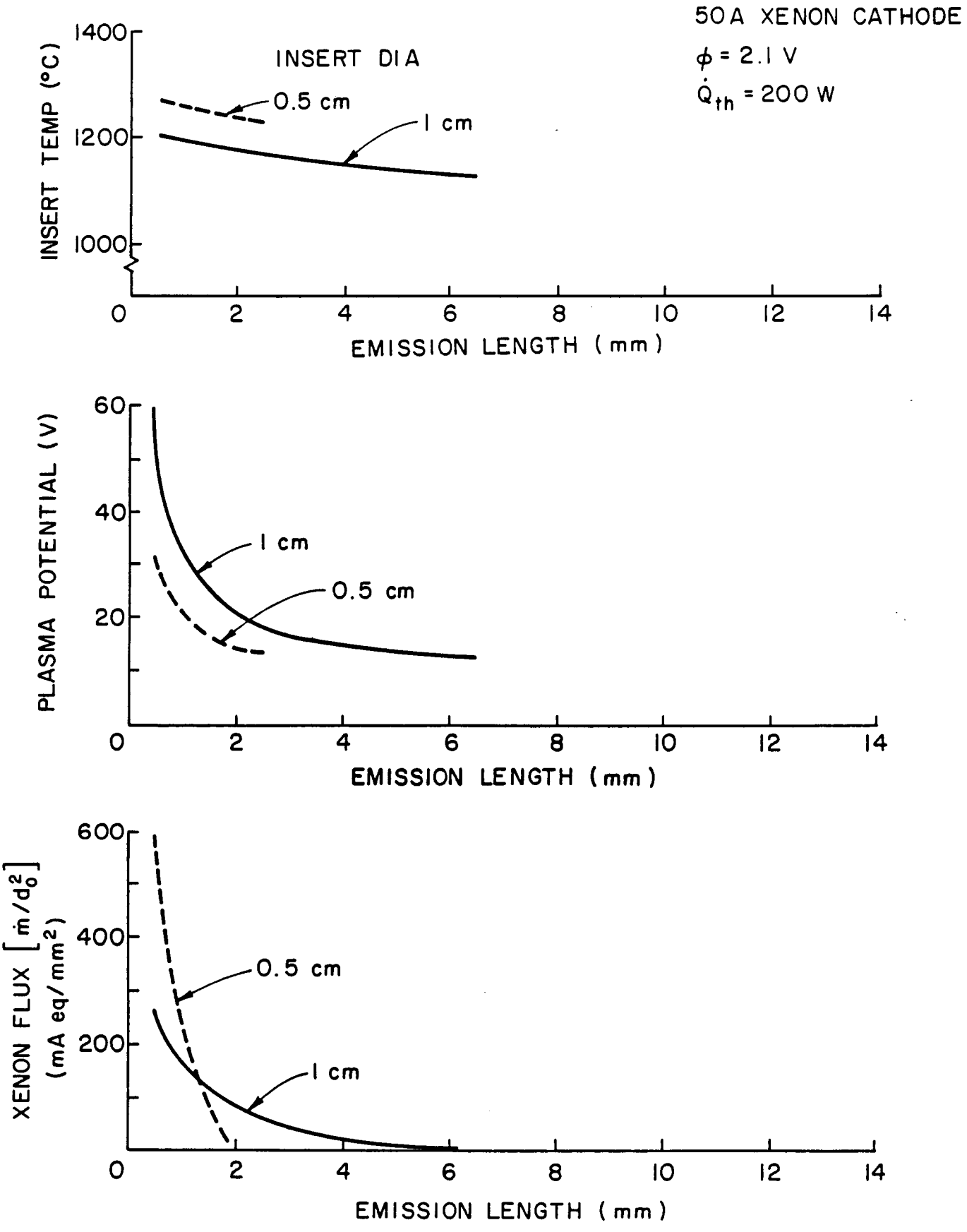

Fig. 69 Effect of Insert Diameter on Cathode Performance Parameters

data suggest the larger insert diameter is preferred at high current levels. It should be noted that xenon flux, which is the mass flowrate of xenon per unit orifice diameter squared, is directly related to cathode internal pressure.

If one were to assume the flow through the cathode orifice were isentropic, choked flow, one might expect a linear relationship between cathode interior pressure and cathode expellant flux. In the present case, however, the discharge current also affects the pressure that would be measured at a fixed flowrate as a results of the collisions that undoubtedly occur in the orifice region. Since this collision process has not been described analytically, Siegfried's approach [11] was followed and an empirical relationship between the discharge current and the pressure per unit xenon flux was obtained. This was done by measuring the cathode internal pressure and flowrate associated with a cathode having a 0.71 mm dia orifice as a function of discharge current. The results are shown in Fig. 70. Since the experimental apparatus allowed measurements to be made only to a discharge current of 15 A an extrapolation to 50 A was needed to project the xenon flux requirements associated with the lowest curve in Fig. 69. This extrapolation was not difficult because the curves of Fig. 70 seem to level out at currents beyond about 15 A. The xenon flux level specified in the lowest plot of Fig. 69 should probably be considered to be accurate to within about 100% because of the uncertainty associated with this assumption. It should be noted regarding to the overall analysis that there are uncertainties associated with the work function associated with a particular insert, the collision cross sections which have been incorporated into the model to compute primary electron mean free paths and the pressure /flux correlation of Fig. 70. This suggests that precise values of the insert diameter required to sustain operation will be uncertain. Still the trends suggested by Fig. 69 are considered correct and they indicate that the occurrence of overheating in an insert can be mitigated

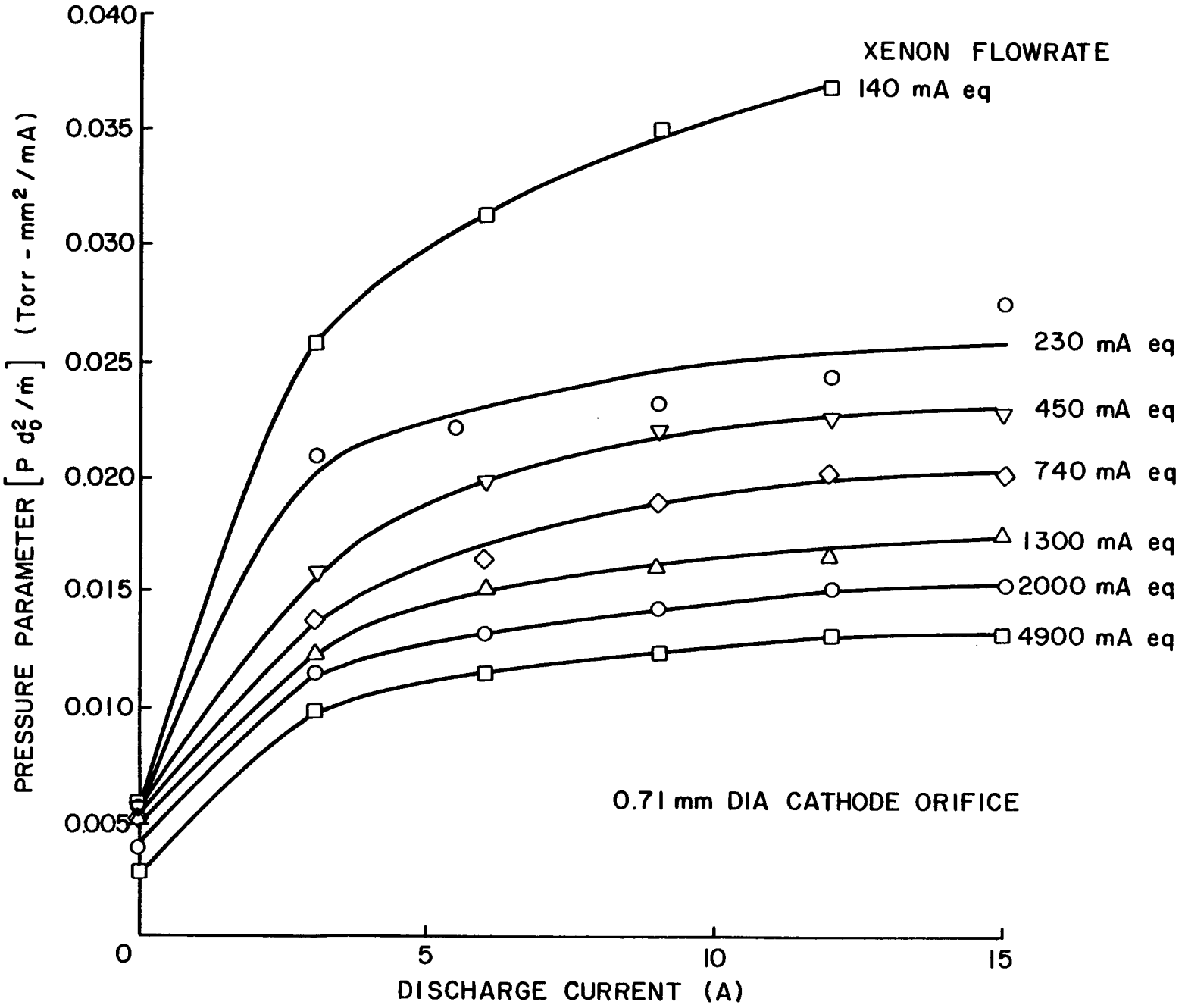

Fig. 70 Flowrate Correlation Data up to 15 A Discharge Current

by increasing the insert diameter and reducing the xenon flowrate to the point where the emission will be occurring over a substantial length of the insert. It can be stated that the model results suggest a 1 cm insert diameter is preferred over a 0.5 cm one.

CONSTRAINED SHEATH OPTICS RESEARCH

The high specific impulse capabilities of ion thrusters have long been recognized as well suited to high characteristic velocity missions such as planatary and deep space probes. Over the past decade, however, the program emphasis within NASA has been directed more toward near-earth missions where ion thrusters must perform at relatively low specific impulses in order to minimize trip times under the constrained of fixed power. Further, it is desirable to use a small number of high thrust-density ion thrusters operating at these low specific impulses to produce the required thrust. This could be accomplished by operating at a low net accelerating voltage to achieve low specific impulse operation and a high total accelerating voltage to achieve the desired high thrust density. Both experimental and theoretical data have shown, however, that conventional two-grid ion optics systems tend to exhibit high ion beamlet divergence losses and high direct ion impingement currents when they are operated at the low ratios of the net-to-total accelerating voltage ($R<0.5$) required.[14,15] Operation can be realized at low net-to-total accelerating voltage ratios by using mechanically more complex three-grid ion optics systems but the associated reduction in R to about 0.2 is still relatively modest.[15,16] The effort described here was undertaken to examine the possibility of constraining the shape of the sheath through which ions are extracted from the discharge plasma to facilitate operation at high current densities and low values of R without encountering the high beamlet divergence behavior that limits the performance of free-sheath optics systems.

In order to understand the mechanisms by which ions are accelerated and diverted from axial trajectories in ion-optics systems, it is instructive to consider the diagram shown in Fig. 71. This diagram shows equipotential contour lines associated with the case where ions are extracted from a flat plane

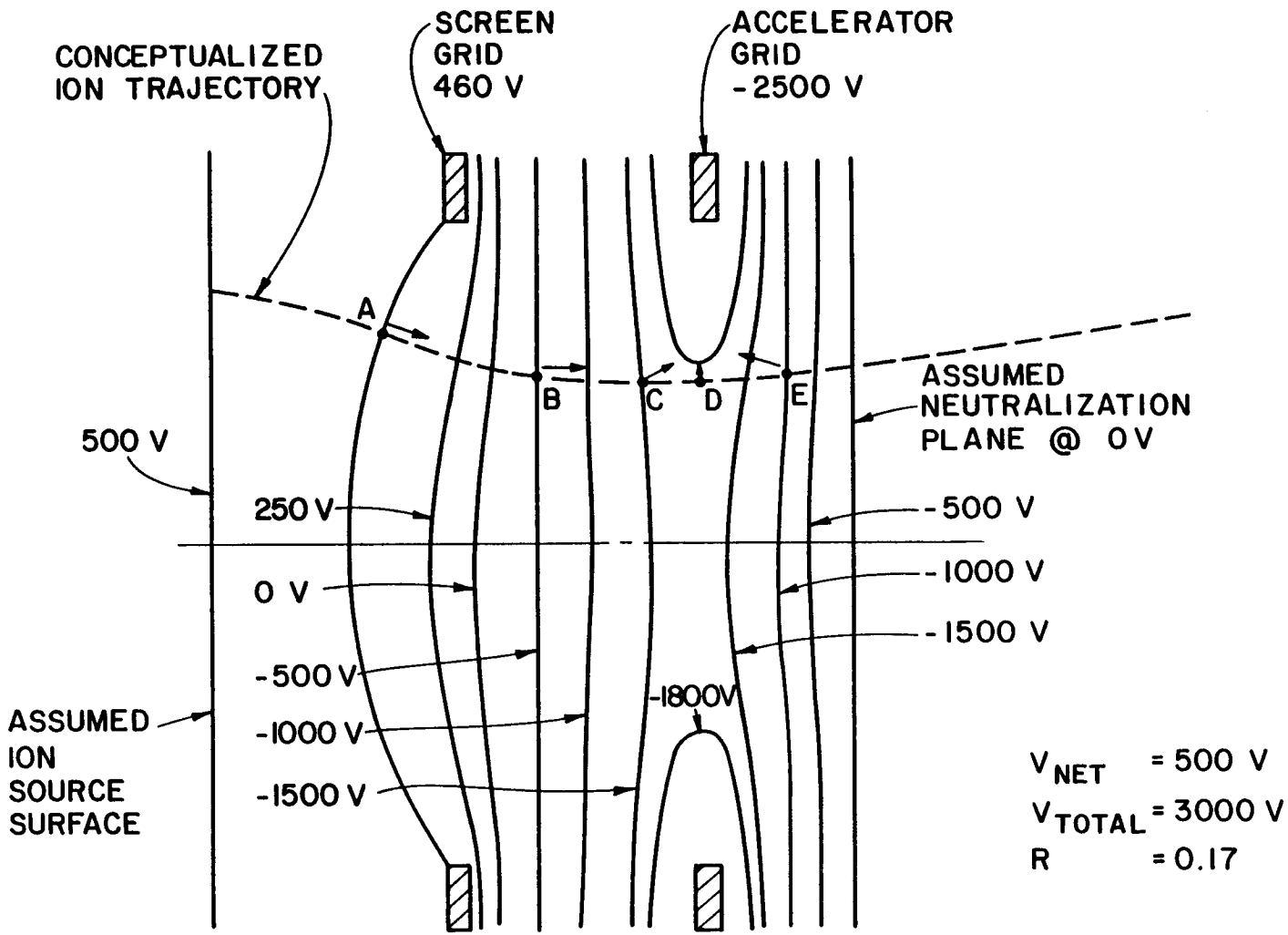

Fig. 71 Equipotential Contour and Ion Trajectory Diagram

at 500 V potential, accelerated through a 460 V screen grid aperture and a -2500 V accelerator grid aperture to a zero potential, flat plane at which neutralization of the ions is presumed to occur. The equipotential lines shown in the figure are the solid ones and the dotted line shows a conceptualized trajectory for an ion coming from the ion source plane and passing through the system at a substantial distance from the centerline of the apertures. The arrows emanating from the dots along the trajectory suggest the direction of electric field vectors along which forces act on the ions as they pass through the grid system along this trajectory. The arrow at position A suggests initial electric field forces acting on the ion have both a downstream axial component and an inward radial component. This inward radial force component causes the ion to be directed closer to the aperture centerline as it accelerates between the grids. This process continues until point B where the electric field contour is observed to be flat and essentially perpendiular to the centerline. At this point, only the axial component of electric field acts. Beyond point B the electric field vectors begin to have a component of electric field directed radially outward as shown at point C. At point D the ion begins to decelerate due to a component of electric field that is directed axially upstream. By the time the ion reaches point E the component of electric field as indicated by the arrow again has a significant outwardly directed radial component in addition to the upstream directed axial component. Figure 71 taken in total shows that the ion sees an outwardly directed radial force that causes it to diverge from point B to the neutralization plane. As the accelerator grid is biased more negative (i.e. the R value is reduced) the ion sees a component of outward directed electric field for a greater and greater fraction of the time associated with its passage through the optics system.

An ion moving along the centerline of the aperture, on the other hand, passes through equipotential surfaces that remain perpendicular to the axis of the screen and accelerator (accel) holes throughout its time of passage through the system. This ion therefore sees no radial component of electric field and as a result it would not diverge. One can see from this discussion that both the radial location at which an ion begins the acceleration process and the net-to-total accelerating voltage ratio influence its divergence angle at the conclusion of the process. One can also see that low divergence operation at a low net-to-total accelerating voltage ratio could be achieved if the bulk of the ions could be directed through the grids along trajectories near the aperture centerline.

If ions were to reach an ion source plane curved in such a way that the ions would all be directed toward the aperture centerline, one might be able to minimize the radial force components and thereby minimize the divergence of the beamlet exiting the grid aperture. In conventional two and three-grid ion optics systems the ion source surface shape, i.e. the sheath shape, is determined by the relative balance between the rate at which ions are supplied from the discharge and the rate at which they are extracted through the optics system. In this case it is not possible to control the ion source surface shape (free-sheath case). If on the other hand one could apply a properly shaped fine wire mesh over the screen aperture it would be possible to establish an immovable ion source surface having any desired shape ("constrained sheath").

Previous experimental investigations utilizing the constrained sheath concept include the work of Byers[17] who discovered that the wire mesh tended to melt, Reifenschweiler and Frohner[18] who achieved well-focused beams at high accelerating voltage levels and more recently Aston[19] whose decoupled extrac-

tion and acceleration concept is quite similar to the constrained sheath optics concept.

A schematic diagram showing the position of the sheath constraining mesh relative to the discharge plasma and the screen and accelerator grids is shown in Fig. 72. This figure also shows the various geometrical symbols used in describing the experiments. For example, the diameters of the screen and accelerator grid apertures (d_s and d_a) the spacing between the grids (ℓ_g) and the thicknesses of the screen and accelerator grids (t_s and t_a) are defined. For all cases considered in this study, the sheath constraining mesh was made of 0.25 mm dia tantalum wire mesh contoured to a spherically shaped surface of radius r_c where r_c is limited to values between d_s and infinity. The effective acceleration length ℓ_e shown in Fig. 72 was used here to compute perveance. This effective acceleration length can be expressed in terms of the other parameters defined in the figure by the equation shown there. Beamlet divergence results will be presented in the form of the divergence half-angle shown in Fig. 72. This angle is defined as the half-angle of the cone with its apex at the accelerator grid which encloses 95% of the beam being extracted through the grid system.

Apparatus and Procedure

Tests were conducted using an 8 cm diameter ring cusp ion source having a single 2.9 cm dia screen aperture at its downstream end. All tests were conducted using argon propellant and the ion beam current density profile was measured about 11 cm downstream of the accelerator grid using a Faraday probe that could be swept across the beam. Reference 20 details the ion source and Faraday probe system. In order to conduct the tests a stable argon discharge

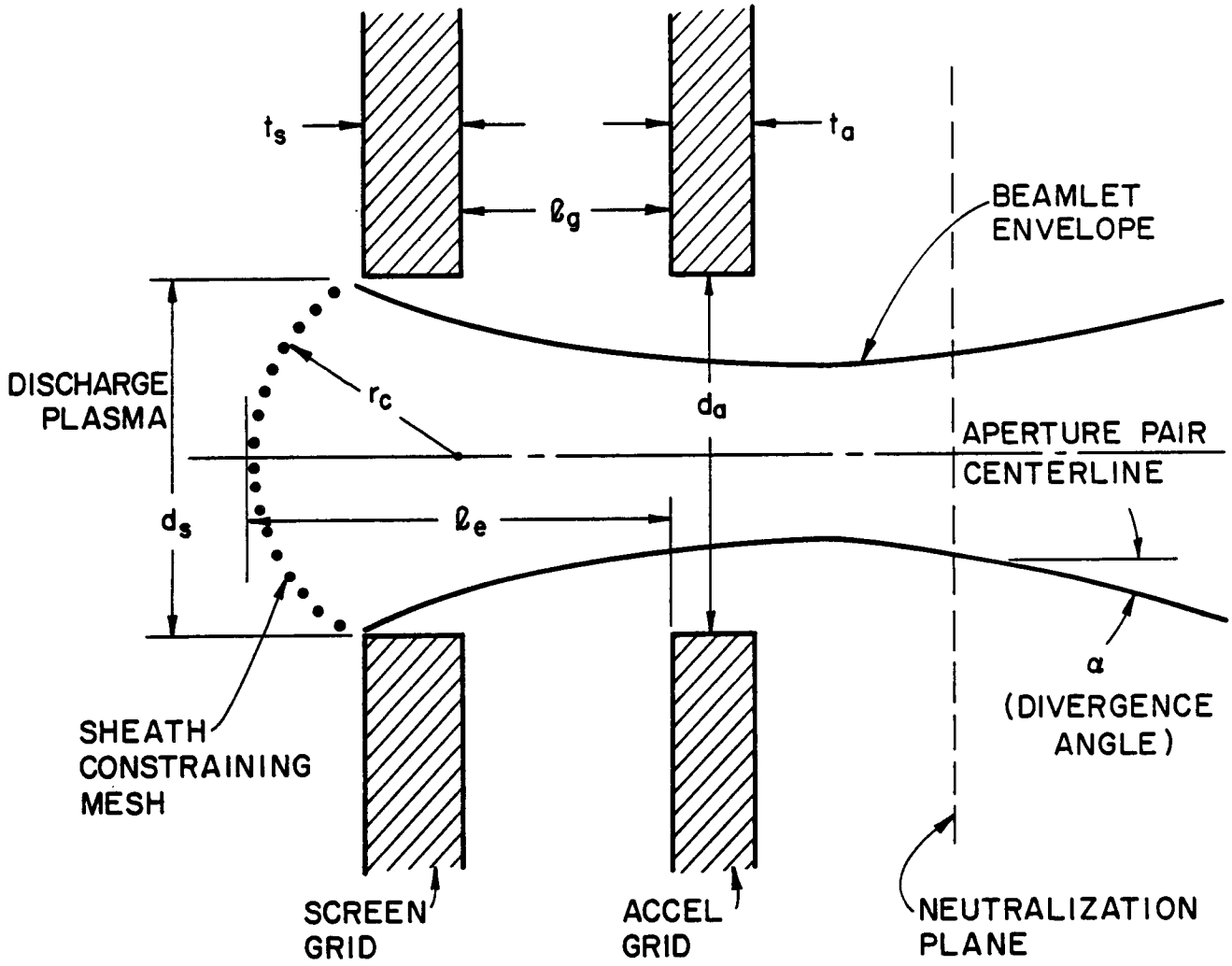

$$\left(\frac{\ell_e}{d_s}\right)^2 = \left\{\frac{\ell_g}{d_s} + \frac{t_s}{d_s} + \frac{r_c}{d_s}\left(1 - \cos\left[\sin^{-1}\left(\frac{d_s}{2r_c}\right)\right]\right)\right\}^2$$

Fig. 72 Constrained Sheath Optics Schematic Diagram

was established in the ion source and the source and accelerator grids were then biased to achieve the desired net and total accelerating voltage condition. The ion beam current extracted was measured directly using a beam current meter and indirectly by integrating the beam current density profile obtained using the Farady probe. The ion source discharge current was then increased in steps and ion beam profiles were measured at each operating condition.

Figure 73 shows example profiles measured at three difference discharge and beam current conditions characterized using a normalized perveance associated with the single aperture being operated by the equation

$$P = \frac{J_B}{V_T^{3/2}} \left(\frac{\ell_e}{d_s} \right)^2 . \qquad (4)$$

In this equation J_B is the beam current, V_T is the total accelerating voltage and ℓ_e and d_s are defined in Fig. 72. The limiting value of this parameter determined from the one-dimensional Child-Langmuir law is $6.8 \times 10^{-9} A/V^{3/2}$ for the argon propellant being used in the study. The three ion beam profiles shown in Fig. 73 reveal the beam profile structures typically observed in the tests. At low perveance values the profiles were gaussian in shape, however at high perveance values they tended to bifurcate producing two peaks away from the centerline of the beamlet. It is suggested that this bifurcation might be due to excessive repulsion forces that tend to develop when too many ions are forced along the centerline of the apertures.

In order to characterize the current density profiles, the measured data were put into a computer program that generated a polynomial curve fit of

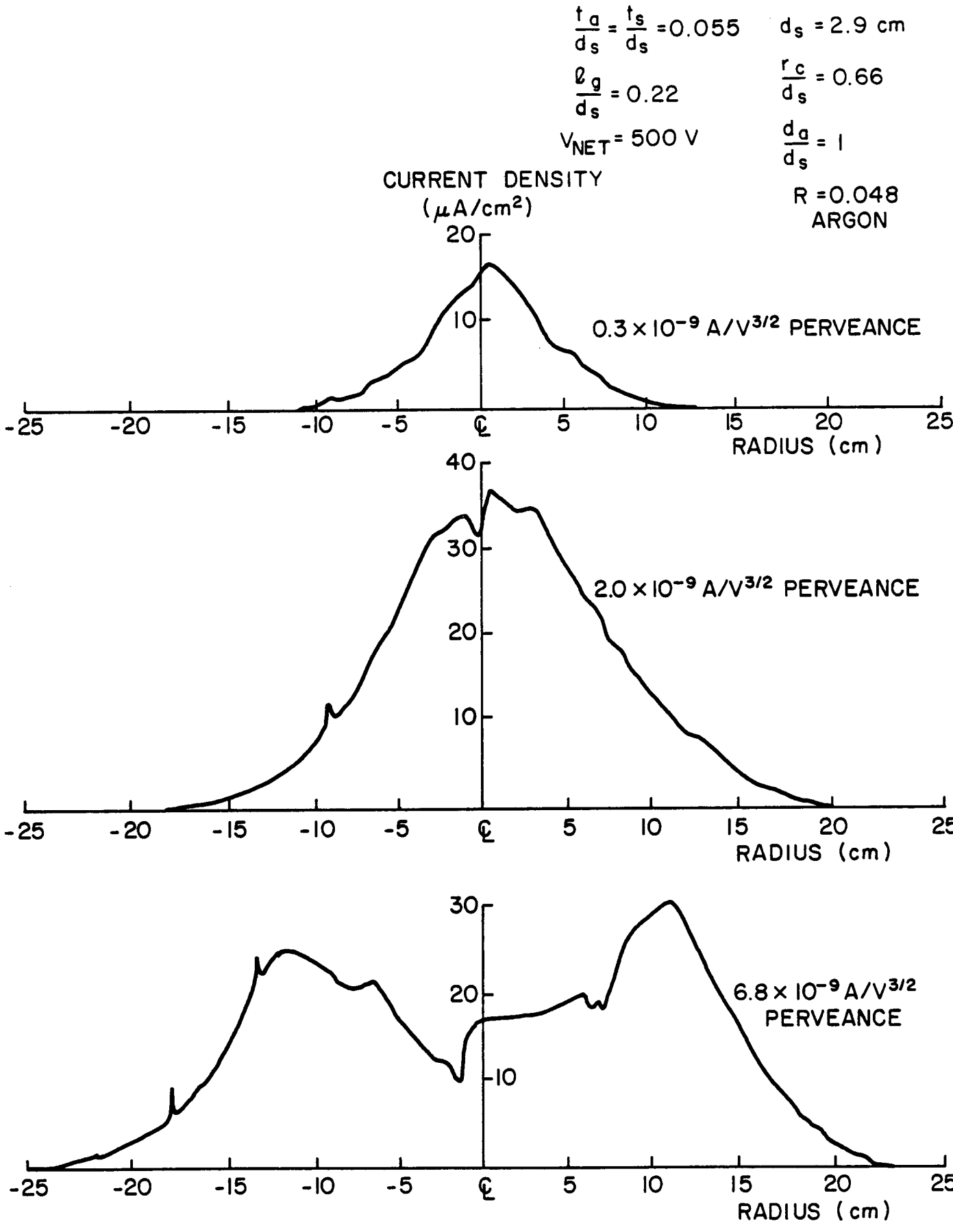

Fig. 73 Typical Current Density Profiles

the data. These curve fits were then integrated to determine a beam current and the divergence half angle. The half angle was found by first determining the radial distance to which the profile had to be integrated to obtain a beam current that was 95% of the total integrated beam current. The arc tangent of tnis radius divided by the distance from the accelerator grid to the probing plane is the desired half-angle. The computer program was also used to determine the ion beam divergence factor which is defined as the ratio of the thrust produced by the beam to the maximum thrust produced if all of the ion trajectories leaving the aperture system were parallel to the axis of the apertures. The computer program determined this factor by integrating the exit velocity for ions passing through a differential, circumferentially shaped band at radius r times the cosine of the divergence angle for that band of ion trajectories from the centerline to the edge of the beamlet.

Results

Typical results obtained experimentally and shown in Fig. 74 are plots of divergence angle and ion beam divergence factor as a function of normalized perveance per hole. Impingement current data associated with results like those of Fig. 74 will not be presented here because they they were small (a few percent of the beam current) until substantial direct ion impingement began to occur near the perveance limit of the system. In the particular case of the data shown in Fig. 74, the separation distance between the grids was varied while other parameters were held constant at values defined in the legend. The general trend suggested is that divergence angle increases substantially as normalized perveance per hole is increased. In each case tnis increase in divergence angle is reflected in a reduction in ion beam divergence factor with values extending as low as about 0.75 for the very closely spaced grids. As grid separation is increased the extent of diver-

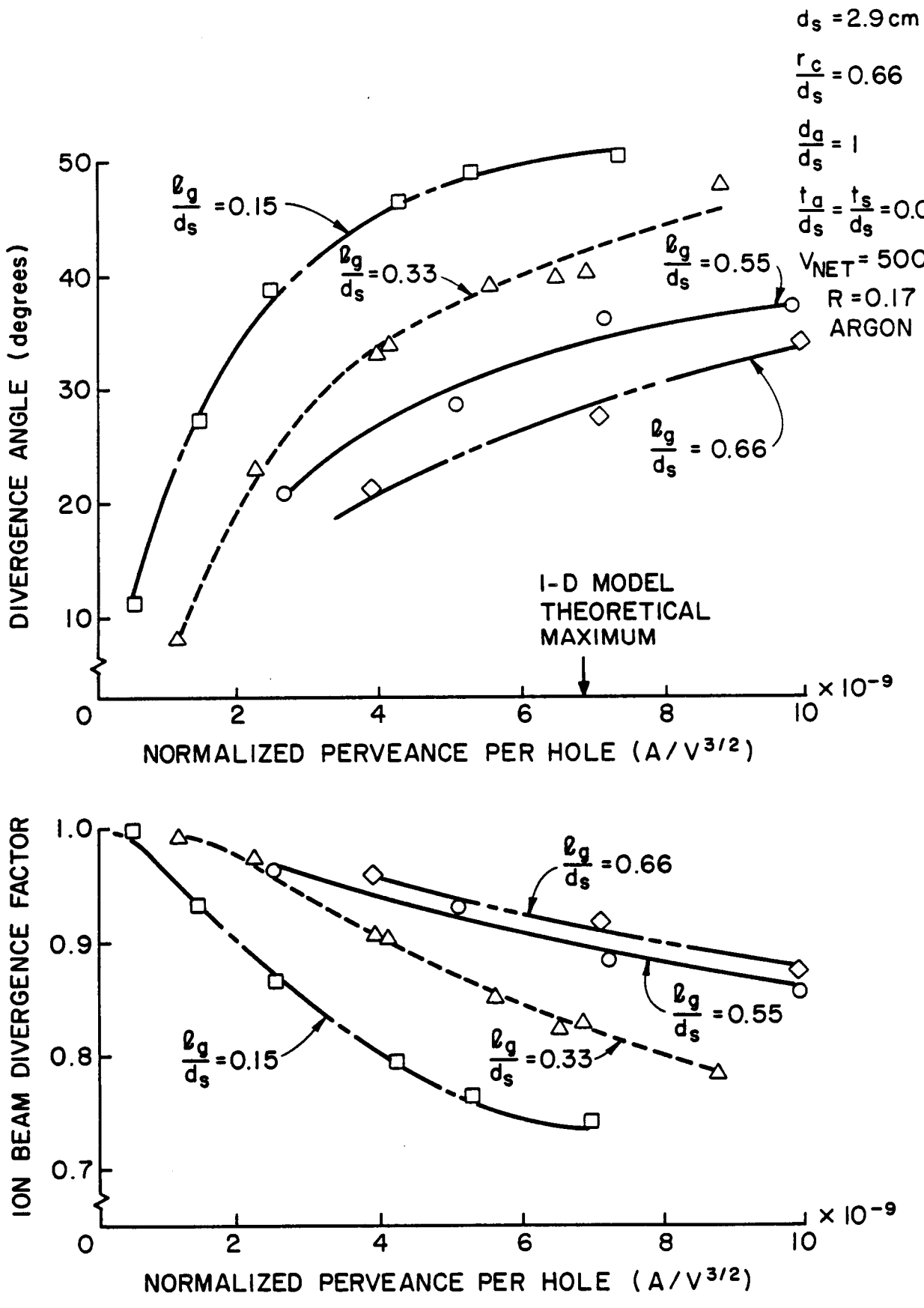

Fig. 74 Effect of Grid Separation on Divergence Characteristics

gence angle increase drops substantially. It should be noted that the net-to-total accelerating voltage ratio for these data are 0.17 and the lowest value of this ratio investigated by Aston for conventional, free-sheath three or two-grid optics systems was about twice this value.[14,16] When Aston attempted operation at lower R-values he observed poor divergence characteristics and high impingement currents. In Aston's case, however, the adverse effect of perveance on divergence angle was much more subdued and divergence angles less than 20° were generally observed as long as R-values were above about 0.3.

One startling feature of the data of Fig. 74 is the maximum normalized perveance at which data were obtained. It was expected that the mesh screen on the screen grid would collect a portion of the ion current and hence the maximum normalized perveance at which the grids could be operated would be substantially below the theoretical limit which for argon is 6.8×10^{-9} $A/V^{3/2}$. In the present case however that normalized perveance values approaching 10×10^{-9} $A/V^{3/2}$ are achieved before direct ion impingement on the accelerator grid became excessive and limited the extractable ion beam current. It could be that the theoretical perveance limit is being exceeded when the constrained sheath optics sets are used because the constraining sheath, which remains fixed in space, maintains a large sheath area exposed to the discharge plasma as the discharge plasma density is increased. In the free sheath case, on the other hand, the sheath collapses toward a plane at the screen grid thus reducing its effective area for the discharge chamber ion collection as perveance is increased. The high perveances realized in the present case could, however, also be related to the definition of the effective acceleration length ℓ_e identified in Fig. 72. This

length, which is defined to extend from the upstream plane of the accel grid to the upstream tangent to the sheath constraining mesh, is appropiate for ions passing on the centerline of the extraction system, but may be too long for ions extracted from the discharge near the screen grid edge. Finally regarding the ion beam divergence factors in Fig. 74, it is noted that beamlet divergence induces some thrust loss, but this loss may be more than compensated by the ability to operate at higher total accelerating voltages where the current densities are greater than those that could be extracted from free-sheath optics systems. More work needs to be done before quantitative responses to the question suggested by this comment can be made.

The effect of changing the net accelerating voltage while holding the net-to-total accelerating voltage ratio and the geometrical factors associated with the grid system constant, is shown in Fig. 75. These data indicate that changing the net accelerating voltage from 500 down to 250 V induces no substantial change in divergence characteristics. In regard to the Fig. 75 data it is suggested that the triangular data point at the high perveance associated with 500 V operation is probably erroneous. Figure 76 shows the effect of changing the net-to-total accelerating voltage ratio on divergence when the net accelerating voltage and geometrical factors are held constant. These data show grid performance improves when the higher net-to-total accelerating voltage ratio is used. At high perveances, however, the data suggest the divergence characteristics are similar.

It is noted at this point that beam currents determined by integrating the current density profiles obtained at each operating condition agreed with the associated measured ion beam current to within about 10% when the net-to-

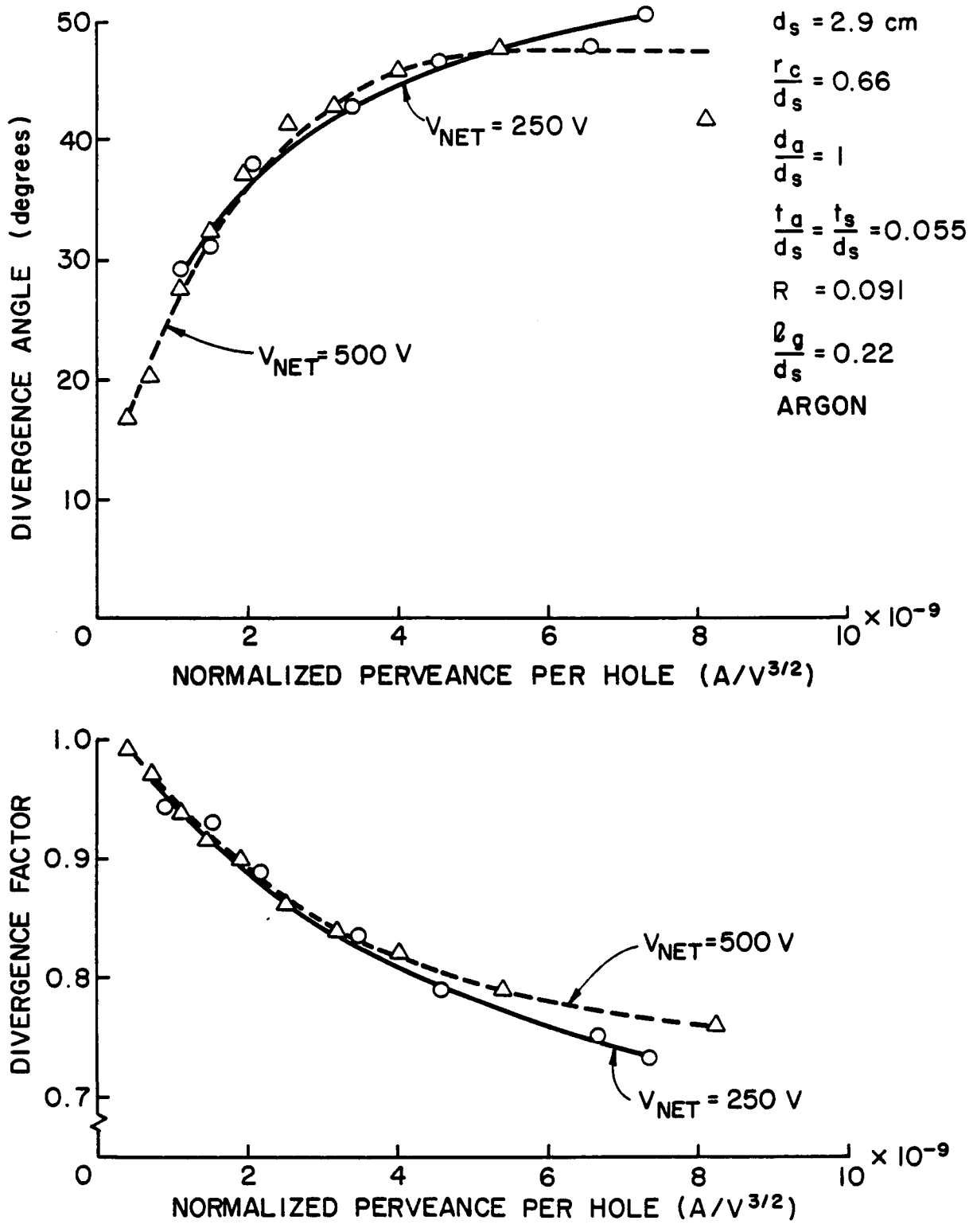

Fig. 75 Effect of Net Accelerating Voltage on Divergence Characteristics

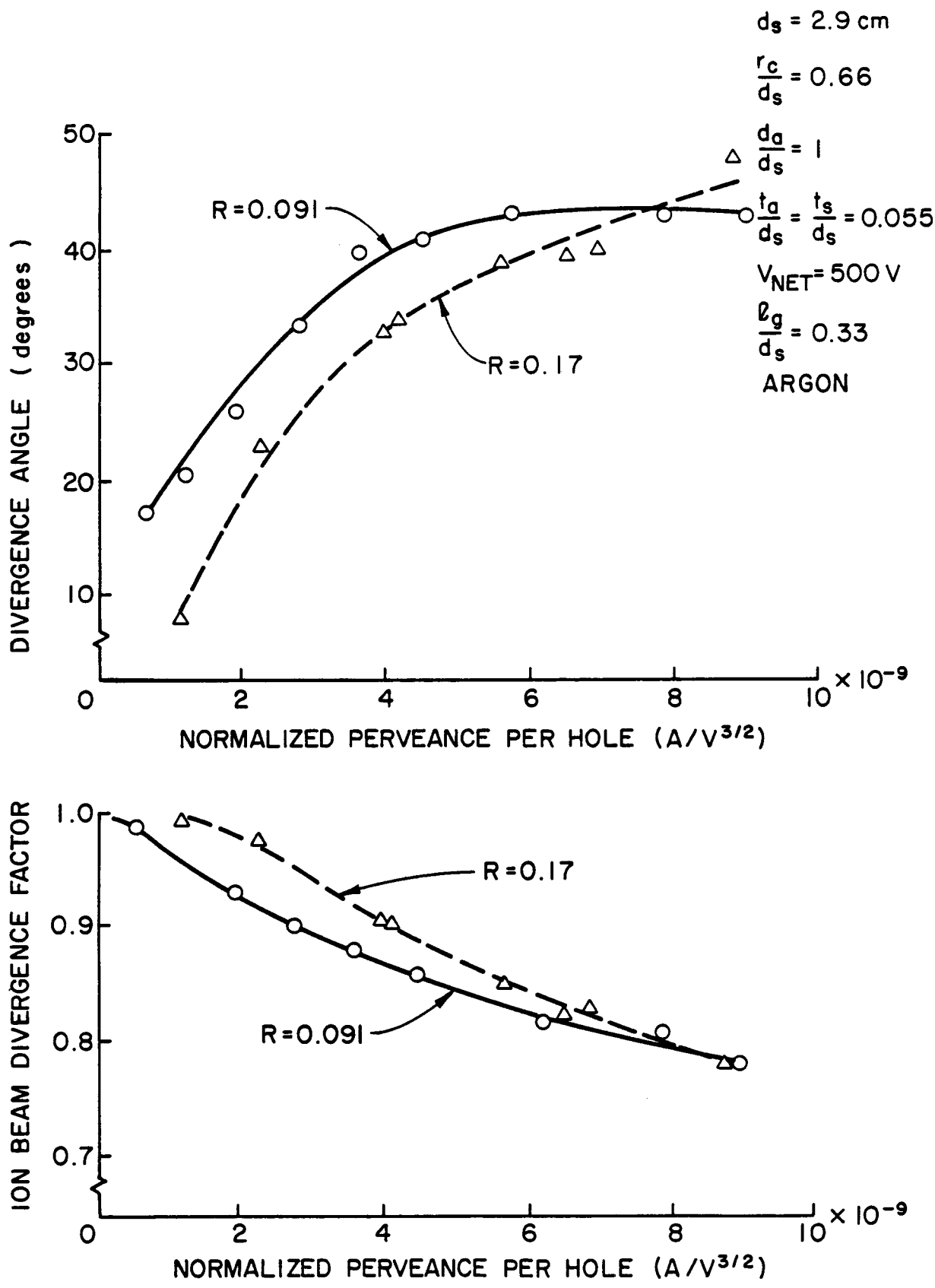

Fig. 76 Effect of Net-to-Total Accelerating Voltage Ratio on Divergence Characteristics

total accelerating voltage ratio was 0.17 and above. As the net-to-total accelerating voltage ratio was reduced below 0.17, however, the integrated beam currents determined from current density measurements dropped systematically below the measured beam currents. This suggests that some ions were escaping detection by the Faraday probe even though it sensed currents leaving at half-angles of divergence up to about 50°. The fact that integrated beam currents were less than measured ones indicates that significant numbers of ions may have been escaping on very divergent trajectories at low net-to-total accelerating voltage ratios. These ions might also be expected to reach the probe at such large radii that very small current densities could go undetected yet contribute substantially to total ion current. These ions would be expected to pass through the grid aperture away from the aperture centerline where they would see a large radial component of the electric field directing them outward.

The effect of changing the radius of curvature associated with the screen constraining mesh is shown in Fig. 77. These data suggest that it is preferable to operate with the smaller radius of curvature mesh which directs ions nearer to the aperture centerline where theory suggests the radial components of electric field that induce divergence are smaller.

Conclusions

A sheath constraining mesh fabricated from tantalum wire and spot welded to the screen grid can influence the focusing of ions extracted through two-grid accelerator apertures. Such a mesh need not limit the perveance of the extraction apertures to values below the theoretical limit for the propellant used. The divergence of the resulting beamlets can be reduced by increasing the separation distance between the grids, by increasing the net-to-total

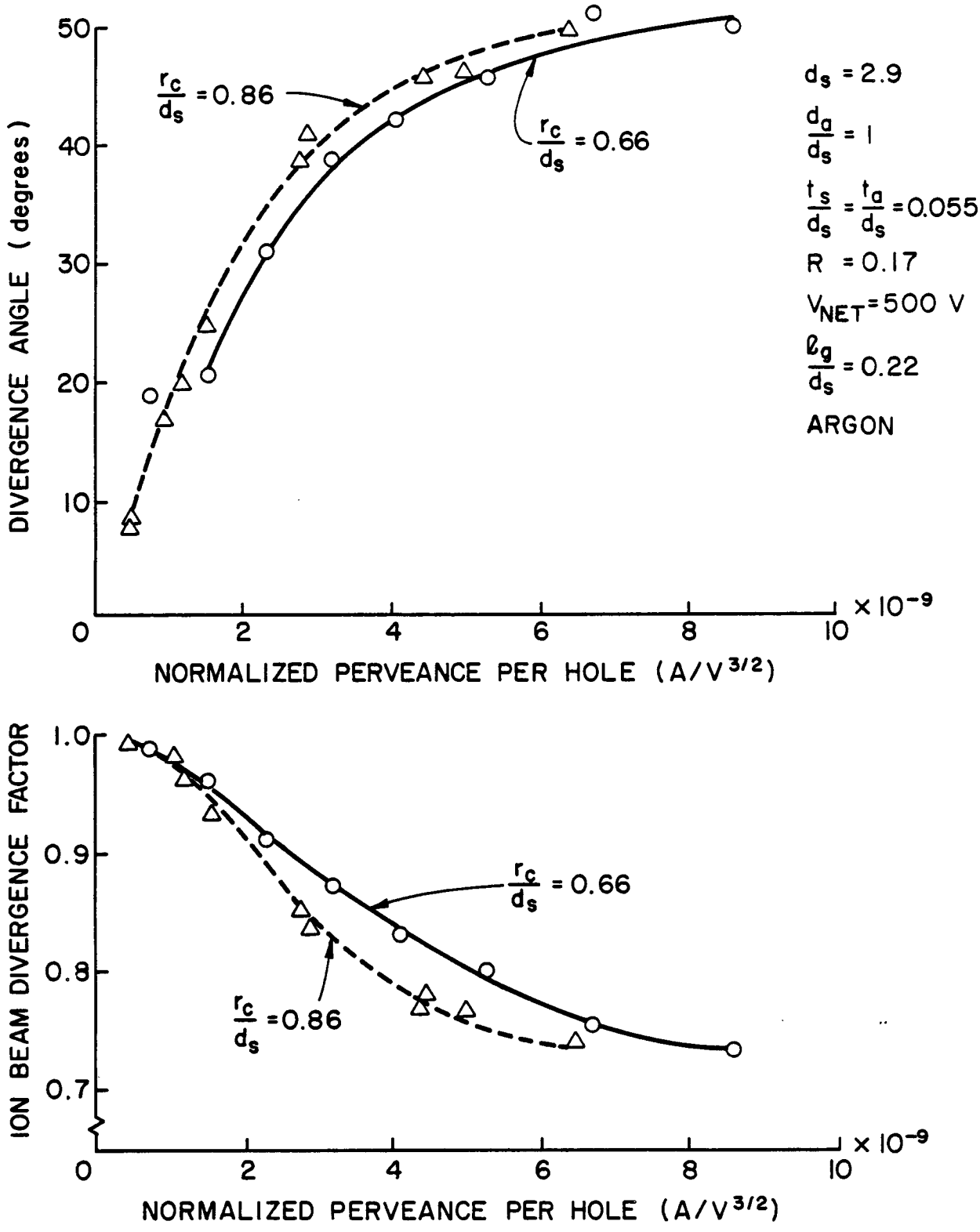

Fig. 77 Effect of Constraining Mesh Radius on Curvature on Divergence Characteristics

accelerating voltage ratio and by decreasing the radius of curvature of the sheath-constraining mesh. In this regard, it is noted that the present study has been limited to hemispherically shaped mesh surfaces and there is no theory indicating such a shape is optimum. In fact, the preferred shape would be expected to have a radius of curvature which varies as a function of radius from the aperture centerline. The experimental results also indicate that a variation in the net accelerating voltage range from 250 to 500 V induces no substantial change in the divergence characteristics of the beamlet.

REFERENCES

1. Sisson, J. M., "Development Status of First Tethered Satellite System," AIAA Paper 86-0049, Jan. 6-9, 1986, Reno, Nevada.

2. Parks, D. E., and I. Katz, "Theory of Plasma Contactors for Electrodynamic Tethered Satallite systems," Appl. of Tethers in Space Workshop, Venice, Italy, Oct. 1555-17, 1985.

3. Wei, R., and P. J. Wilbur, "Space-Charge - Limited Current Flow in a Spherical Double Sheath," J. Appl. Phys., V. 60, 1 Oct. 1986, pp. 2280-2284.

4. Aston, G., "Ion Extraction from a Plasma," NASA CR-159849, June 1980, pp. 12-19.

5. Laupa, T., "Electrodynamic Tether Plasma Contactor Research," appears in "Advanced Electric Propulsion and Space Plasma Contactor Research," P. J. Wilbur ed., NASA CR-175119, p. 34 f.

6. Wilbur, P. J., "Hollow Cathode Plasma Coupling Study" - 1986, NASA CR-171985, Dec. 1986.

7. Patterson, M. J. and P. J. Wilbur, "Plasma Contactors for Electrodynamic Tether," NASA TM-88850, Sept. 17-19. 1986.

8. Brophy, J.R., Ion Thruster Performance Model , NASA CR-174810, December 1984.

9. Luebben, C., "High Pressure Hollow Cathode Research," appears in NASA CR-175119, Jan. 1986, P. J. Wilbur, ed., p. 69 f.

10. Hardy, Terry L., private communication to Paul Wilbur, March 1986.

11. Siegfried, D. E., "A Phenomenological Model for Orificed Hollow Cathodes," NASA CR-168026, Dec. 1982.

12. Hiatt, J. M. and P. J. Wilbur, "Ring Cusp Discharge Chamber Performance," AIAA Paper 85-2007, AIAA 18th International Electric Prop. Conference, Alexandria, Virginia, Oct. 1985.

13. Siegfried, D. E., "Xenon and Argon Hollow Cathode Research," appears in "Advanced Ion Thruster Research," P. J. Wilbur, ed., NASA CR-168340, Jan. 1984, p. 76 f.

14. Aston, G., H. R. Kaufman and P. J. Wilbur, "Ion Beam Divergence Characteristics of Two-Grid Accelerator Systems," AIAA Journal, V. 16, No. 5, May 1978, pp. 516-524,

15. Kaufman, H. R., "Accelerator-System Solutions for Broad-Beam Ion Sources," AIAA Journal, V. 15, No. 7, July 1977, pp. 1025-1034.

16. Aston, G. and H. R. Kaufman, "Ion Beam Divergence Characteristics of Three-Grid Accelerator Systems," AIAA Journal, V. 17, No. 1, Jan. 1979, pp. 64-70.

17. Byers, D. C., "An Experimental Investigation of a High-Voltage Electron-Bombardment Ion Thruster," Electrochemical Science, V. 116, No. 1, Jan. 1969, pp. 9-17.

18. Reifenschweiler, O. and K. R. Frohner, "A New Principle of Ion Extraction from a Gas Discharge Plasma," Nuclear Inst. and Math., V. 30, 1964, pp. 298-302.

19. Aston, G. and W. D. Deininger, "The DE-AC Accelerator System for High Beam Current Density," 17th International Electric Propulsion Conference Paper 84-85, Tokyo, Japan, 1984.

20. Wilbur, P. J. and L. O. Daniels, "The development and application of an ion implanter based on ion thruster technology," VACUUM, V. 36, No. 1-3, 1986, pp. 5-9.